Dissertation

submitted to the

Combined Faculty of Mathematics, Engineering and Natural Sciences

of

Heidelberg University, Germany

for the degree of

Doctor of Natural Sciences

Put forward by

Casper Arie van Veen

born in: Oosterhout, Nederland

Oral examination: July 4, 2025

Simulation Studies for Measuring the Soft-Photon Spectrum with the ALICE 3 Forward Conversion Tracker

Referees: Prof. Dr. Klaus Reygers
Prof. Dr. Hans-Christian Schultz-Coulon

Abstract

The soft-photon puzzle has been an open problem in high energy particle physics for many years now. Experiments have been performed in the past to try to measure the soft-photon spectrum of inelastic $m \to n$ scattering processes. Some measured an excess of a factor 4–8 in terms of the internal bremsstrahlung spectrum predicted by Low's theorem, but others measured no excess at all. This work presents for the first time a full Monte Carlo simulation with generated internal bremsstrahlung photons predicted by Low's theorem propagated through the detector setup of ALICE 3. One of the goals of the proposed ALICE 3 experiment is to measure the soft-photon spectrum with the use of the Forward Conversion Tracker through the tracking of e^+e^- conversion pairs in a separate dipole magnetic field. Through dedicated studies of the (spatial) origin of the various sources of background, cuts and vetoes are implemented to minimize its impact on the measurement. These studies show a significance of 5–10 in the regime of $0.5 < k_T < 7.5\,\mathrm{MeV}/c$ for the case where the excess is 4 times the predicted internal bremsstrahlung spectrum. A conical modification of the beam pipe is suggested to reduce the material budget in front of the FCT and as such the kinematic regime where the significance exceeds 5 is extended to $0.5 < k_T < 10\,\mathrm{MeV}/c$ for the case where the excess is 4 times the predicted internal bremsstrahlung spectrum. In this thesis the theory, previous measurements and the performance of the proposed Forward Conversion Tracker will be discussed.

Kurzfassung

Das Rätsel der Produktionsrate weicher Photonen ist seit vielen Jahren ein ungelöstes Problem in der Hochenergie-Teilchenphysik. In der Vergangenheit wurden Experimente durchgeführt, um das Spektrums weicher Photonen von inelastischen $m \rightarrow n$ Streuprozessen zu messen. Einige dieser Experimente stellten einen Überschuss um den Faktor 4–8 im Vergleich zum durch Lows Theorem vorhergesagten Spektrum der internen Bremsstrahlung fest, während andere keinerlei Überschuss messen konnten. In dieser Arbeit wird erstmals eine vollständige Monte-Carlo-Simulation präsentiert, in der intern erzeugte Bremsstrahlungsphotonen, wie sie durch Lows Theorem vorhergesagt werden, durch den Detektoraufbau von ALICE 3 propagiert werden. Eines der Ziele des vorgeschlagenen ALICE 3-Experiments ist die Messung des Spektrums weicher Photonen mithilfe des Forward Conversion Trackers, der die e^+e^- Konversionspaare in einem separaten Dipolmagnetfeld verfolgt. Durch gezielte Studien zum (räumlichen) Ursprung der verschiedenen Hintergrundquellen werden Schnitte und Vetos implementiert, um den Einfluss auf die Messung zu minimieren. Diese Studien zeigen eine Signifikanz von 5–10 im Bereich von $0.5 < k_\mathrm{T} < 7.5\,\mathrm{MeV}/c$, für den Fall, dass der Überschuss das Vierfache des vorhergesagten Spektrums der internen Bremsstrahlung beträgt. Eine konische Modifikation des Strahlrohrs wird vorgeschlagen, um das Materialbudget vor dem FCT zu reduzieren, wodurch der kinematische Bereich, in dem die Signifikanz den Wert 5 übersteigt, auf $0.5 < k_\mathrm{T} < 10\,\mathrm{MeV}/c$ erweitert wird – ebenfalls für den Fall eines vierfachen Überschusses gegenüber der Vorhersage. In dieser Arbeit werden die Theorie, frühere Messungen und die Leistungsfähigkeit des vorgeschlagenen Forward Conversion Trackers diskutiert.

Words in advance

In this short paragraph I want to thank the people of the ALICE Heidelberg group and for the opportunities I was given for personal development. I thank all for the interesting scientific discussions, but especially so for the engaging talks and laughs we had. I especially want to thank Klaus Reygers who was an excellent supervisor and from whom I truly learned a lot. I then want to thank my parents who helped me through challenging times and were always there for me.

Complex acronyms and jargon can be confusing for those that want to learn and advance in a field. For this purpose I, with the help of Ilya Fokin, developed the High Energy Physics Dictionary. I do not claim it to be perfect, but it has helped me tremendously during talks and when I tried to read papers that did not share the meaning of the acronyms they used. I hope it can help you as well! I included a QR code which contains the link to the website[1].

HEPAD: the High Energy Physics Dictionary. QR code: `https://hepad.physi.uni-heidelberg.de/`. It contains more than 3000 entries for all of HEP, from theory to hardware. Feel free to share it or use this QR code in your presentations.

[1] It is not findable through search engines (yet!).

Contents

1 Introduction

Theory and experimental results have yet to reach a satisfying agreement between the prediction and measurement of the soft-photon spectrum in scattering processes. Since 1979, a multitude of experiments have been conducted in an attempt to measure this soft-photon spectrum, but results varied significantly. In these scattering processes, soft photons can have many origins, the most dominant of which are the decay of neutral hadrons and internal bremsstrahlung as a result of accelerating charges. The soft photon spectrum coming from the decay of neutral hadrons, dominated by $\pi^0 \to \gamma\gamma$, has been widely studied and measured. In 1958, Francis E. Low published a paper [1] which contained a theory to predict the internal bremsstrahlung spectrum in $2 \to 2$ processes. Extensions and generalizations of this theory were made [2–4] and the findings were established in theoretical physics, namely the infrared structure of gravity and gauge theory to name a few. It is safe to say that Low's theorem has firmly established itself in theoretical particle physics. Yet, when the experimental physics community attempted to measure the soft internal bremsstrahlung spectrum, some measured a significant excess in terms of a factor 4-8 with respect to the predicted internal bremsstrahlung spectrum, while others did not measure an excess at all. This came to be known as the "soft-photon puzzle". An overview of the experimental attempts to measure the soft internal bremsstrahlung spectrum is given in Tab. 1.

Most experiments that were conducted measured an excess of a factor 4–8 in terms of the predicted internal bremsstrahlung spectrum. It must be noted that some measurements did not show a(n) (significant) excess [5, 6]. The most recent result from the DELPHI collaboration [7] has led many to believe the origin of the excess is related to QCD interactions, since the measurement showed no excess in the well-understood, fully QED-predicted production channel of $e^+e^- \to \mu^+\mu^-$.

During the Long Shutdown 4 of the LHC the ALICE collaboration plans to install its proposed next-generation detector called ALICE 3 [8]. This detector will be able to operate at a much higher rate than its predecessors and some of the defining features will be its large coverage in pseudorapidity, $|\eta| < 4$, distance of the first layer to the interaction point, 5 mm, and low material budget, 0.3% for the first three inner tracking layers. As a part of the plan, the Forward Conversion Tracker (FCT) is proposed to shine light on the soft-photon puzzle and provide a measurement of the soft internal bremsstrahlung spectrum at a never seen before collision energy of $\sqrt{s} = 14\,\text{TeV}$. The FCT and techniques employed for this study have several competitive edges compared to previous experiments which will be highlighted in this thesis.

Section 2 will explain the theory behind Low's theorem and Haissinski's formula and present two generators to include the production of internal bremsstrahlung in full Monte Carlo simulations with the event generator PYTHIA [9]. Section 3 will cover the previous attempts to measure the soft-photon spectrum and attempt to find some common defining features of the excess they reported. Section 4 will introduce the proposed ALICE 3 experiment and outline its capabilities. In addition, the integrated luminosity requirements for the measurement of the soft-photon spectrum with the FCT will be covered. Section 5 will talk about the simulation strategy of the measurement of the soft-photon spectrum with the FCT and introduce and classify the sources of background. This section also covers the propagator which is used to perform the simulation of particle propagation through the detector setup of ALICE 3. The performance of the FCT is then covered in Section 6. In this section, great care is taken to uncover the differences between the produced background and the signal and the origin of the different background channels are carefully mapped out. Different ways to minimize the impact on the measurement are proposed which cover cuts on the geometric differences of the signal and background. In addition, a modification of the beam pipe is proposed to reduce the material budget in front of the FCT. Lastly, a Cherenkov detector is proposed to provide an event veto for events that contain electrons which are known to radiate big amounts of external bremsstrahlung. Section 7 will cover the uncertainty estimates on the background and discuss the uncertainty on the material budget from different modules in the detector setup of ALICE 3. Section 8 will show the low transverse momentum neutral pion reconstruction capabilities of the FCT. In the discussion, Section 9, improvements will be discussed.

Experiment	Year	p_{beam} or $\sqrt{s}$	Photon k_{T}	$\gamma_{\text{meas}}/\gamma_{\text{brems}}$	Reference
π^+p	1979	10.5 GeV/c	$k_{\text{T}} < 20$ MeV/c	1.25 ± 0.25	[10]
K^+p WA27, CERN	1984	70 GeV/c	$k_{\text{T}} < 60$ MeV/c	4.0 ± 0.8	[11]
π^+p CERN, EHS, NA22	1991	250 GeV/c	$k_{\text{T}} < 40$ MeV/c	6.4 ± 1.6	[12]
K^+p CERN, EHS, NA22	1991	250 GeV/c	$k_{\text{T}} < 40$ MeV/c	6.9 ± 1.3	[12]
π^-p CERN, WA91, OMEGA	1993	280 GeV/c	$k_{\text{T}} < 10$ MeV/c $(0.2 < E_\gamma < 1GeV)$	7.9 ± 1.4	[13]
p-Be	1993	450 GeV/c	$k_{\text{T}} < 20$ MeV/c	< 2	[5]
p-Be, p-W	1996	18 GeV/c	$k_{\text{T}} < 50$ MeV/c	< 2.65	[6]
π^-p CERN, WA91, OMEGA	1997	280 GeV/c	$k_{\text{T}} < 20$ MeV/c $(0.2 < E_\gamma < 1\text{GeV})$	7.8 ± 1.5	[14]
π^-p CERN, WA91, OMEGA	2002	280 GeV/c	$k_{\text{T}} < 20$ MeV/c $(0.2 < E_\gamma < 1\text{GeV})$	5.3 ± 1.0	[15]
pp CERN, WA102, OMEGA	2002	450 GeV/c	$k_{\text{T}} < 20$ MeV/c $(0.2 < E_\gamma < 1\text{GeV})$	4.1 ± 0.8	[16]
$e^+e^- \to n$ jets CERN, DELPHI	2006	91 GeV ($\sqrt{s}$)	$k_{\text{T}} < 80$ MeV/c $(0.2 < E_\gamma < 1\text{GeV})$	$4.0 \pm 0.3 \pm 1.0$	[17, 18]
$e^+e^- \to \mu^+\mu^-$ CERN, DELPHI	2008	91 GeV ($\sqrt{s}$)	$k_{\text{T}} < 80$ MeV/c $(0.2 < E_\gamma < 1\text{GeV})$	~ 1	[7]

Table 1: An overview of the experimental attempts to measure the soft internal bremsstrahlung spectrum. The excess measured by each experiment in as ratio of the predicted spectrum is given in the column "$\gamma_{\text{meas}}/\gamma_{\text{brems}}$".

2 Theory: Low's theorem

In scattering processes, bremsstrahlung is produced by accelerating initial-, intermediate- and final-state charged particles. The energy, or more intuitively the wavelength, of the bremsstrahlung is limited by the lifetime and spatial extent of the emitting source. The lifetime and the spatial extent of intermediate-state particles in inelastic hadronic interactions are short and are usually estimated to be $\Delta t \approx 1\,\mathrm{fm}/c$ and $\Delta x \approx 1\,\mathrm{fm}$, respectively [19]. Photons with a sufficiently long wavelength can therefore only be emitted by initial- and final-state charged particles. Photons in this energy regime are referred to as "soft photons". The exact wavelength, or energy, that defines the boundary at which these photons are emitted has sparked many discussions (e.g. [20], [21]) over the years. Considering that the wavelength of a 100 MeV photon is about 12 fm, it is thus expected that photons with energies of less than 10–100 MeV qualify as soft photons for inelastic hadronic interactions. In literature, the bremsstrahlung produced in inelastic hadronic interactions goes by the names internal bremsstrahlung and inner-bremsstrahlung. In this thesis, the term internal bremsstrahlung is used.

Low's theorem predicts the soft internal bremsstrahlung spectrum for particles involved in a $m \to n$ scattering process. In his original paper [1], the author considered 2-to-2 scattering processes plus an additional photon in the final state. Putting it in very simple terms, the paper relates the production of soft internal bremsstrahlung photons to the production of initial- and final-state charged particles, without the need to evaluate what happens at the intermediate state. He talked about the cross section σ, given by the power expansion

$$\sigma = \frac{\sigma_0}{\omega_k} + \sigma_1 + \omega_k \sigma_2 + \ldots, \tag{1}$$

for which he provided expressions for σ_0 (leading power) and σ_1 (next-to-leading power) where ω_k is the photon energy corresponding to the four-momentum k. This was later generalized for the leading-power term for $m \to n$ scattering processes. A more complete theoretical overview and modern interpretation of Low's theorem was recently published [19].

2.1 A short overview of the derivation of the soft-photon theory

In his paper [1], Francis Low obtained his result for spin-0 particles. Burnett and Kroll [2] then extended this to scattering processes of particles of spin 1/2, and Bell and Van Royen [3] gave the generalization for particles of arbitrary spin.

Steven Weinberg provided a treatment for the special case of the emission of a single soft photon in a $1 \to 1$ transition of a spin-1/2 particle [22] [4],

$$M(p_f, s_f; k, \lambda | p_i, s_i) = \frac{Qe}{\sqrt{2\omega_k}} \epsilon^*_\mu(\boldsymbol{k}, \lambda) \left\{ \frac{p_f^\mu}{k \cdot p_f} - \frac{p_i^\mu}{k \cdot p_i} \right\} M^0_{fi}(p_f, s_f; p_i, s_i) + \mathcal{O}(\omega_k^0). \tag{2}$$

Here M is the amplitude of emitting a soft photon with momentum k and polarization λ from an accelerating charged particle that goes from the initial state with momentum p_i and spin s_i to the final state with momentum p_f and spin s_f due to an interaction. Q is the charge[2] of the particle, ω_k the energy of the emitted photon, $\epsilon^*_\mu(\mathbf{k}, \lambda)$ the photon polarization four-vector, k the photon momentum four-vector, M_0 the amplitude of the process of initial-state charged particles going to final-state charged particles without the emission of a photon plus higher order corrections $\mathcal{O}(\omega_k^0)$. This is then in complete agreement with the result obtained from classical electrodynamics for soft-photon emission,

$$M(p_f; k, \lambda | p_i) = \frac{Qe}{\sqrt{2\omega_k}} \epsilon^*_\mu(\boldsymbol{k}, \lambda) \left\{ \frac{p_f^\mu}{k \cdot p_f} - \frac{p_i^\mu}{k \cdot p_i} \right\}. \tag{3}$$

[2] Here, $Q_i = Q_f = Q$.

A comprehensive summary of the derivation for both formulas and their comparison is given in Ref. [19]. The soft factor,

$$\frac{Qe}{\sqrt{2\omega_k}}\epsilon_\mu^*(\boldsymbol{k},\lambda)\left\{\frac{p_f^\mu}{k\cdot p_f}-\frac{p_i^\mu}{k\cdot p_i}\right\}, \tag{4}$$

of the Weinberg result does not depend on the particular features of the transition the charged particle undergoes, nor on its spin dimensions. This result can then be used as a building block in the case where this transition involves many charged particles, which results in

$$M_{fi}^1=\frac{e}{\sqrt{2\omega_k}}\sum_{n=1}^{N_i+N_f}\eta_n Q_n\frac{\epsilon^*(\boldsymbol{k},\lambda)\cdot p_n}{k\cdot p_n}M_{fi}^0+\mathcal{O}(\omega_k^0). \tag{5}$$

In this formula, the amplitude of the transition $i\to f$ with the emission of one real soft photon, M_{fi}^1, is related to the amplitude of the same transition but without the emission of these photons, M_{fi}^0, plus higher order corrections, $\mathcal{O}(\omega_k^0)$. The sum runs over all initial- and final-state charged particles where $\eta_n=+1$ for outgoing and $\eta_n=-1$ for incoming charged particles. Saying that the sum only runs over charged particles is stating the obvious since Q_n is the charge and subsequently 0 for neutral particles, but this is done to underline that it is the charged particles that are responsible for the emission of these photons. p_n is the four-momentum of the particle and carries the information about the acceleration, or transition, the charged particles undergo. $\epsilon^*(\mathbf{k},\lambda)$ is the photon polarization 4-vector and carries the information about the photon production. This formula is convenient because it shows that the non-radiative amplitude, M_{fi}^0, and the radiative amplitude, M_{fi}^1, are related through the so-called soft-photon production factor,

$$\frac{e}{\sqrt{2\omega_k}}\sum_{n=1}^{N_i+N_f}\eta_n Q_n\frac{\epsilon^*(\boldsymbol{k},\lambda)\cdot p_n}{k\cdot p_n}. \tag{6}$$

Here it can be seen that the factor arises from the interference of photon production from incoming and outgoing charged particles. Due to the negligible contribution of intermediate state virtual charged particles to the soft-photon production cross section, Low's leading term is tree-level correct. The amplitude M_{fi}^1 is used to calculate the cross section for the case with one photon in the final state. Extending this to the case for multiple photons in the final state gives

$$M_{fi}^{N_\gamma}=\prod_{r=1}^{N_\gamma}\left\{\frac{\epsilon_\mu^*(\boldsymbol{k}_r,\lambda_r)}{\sqrt{2\omega_k}}e\sum_{n=1}^{N_i+N_f}\eta_n Q_n\frac{p_n^\mu}{k_r\cdot p_n}\right\}M_{fi}^0+\mathcal{O}(\omega_k^0), \tag{7}$$

for low-energy photons with momentum k_r and polarization λ_r, with $r=1,\ldots,N_\gamma$.

2.2 Theoretical derivation and observables

This soft-photon spectrum shows some interesting properties, namely the angular distribution and the number of photons emitted per event, which will be discussed in this section. Eq. 7 can be used to calculate the soft-photon spectrum, however, it is easier to consider the case where one soft photon is emitted Eq. 5, and calculate its probability density dI,

$$dI=\frac{d^3\boldsymbol{k}}{(2\pi)^3}\sum_{\lambda=\pm1}|M_{fi}^1|^2=\frac{d^3\boldsymbol{k}}{(2\pi)^3}\frac{e^2}{2\omega_k}\sum_{\lambda=\pm1}\epsilon_\mu^*(\boldsymbol{k},\lambda)\epsilon_\nu(\boldsymbol{k},\lambda)\sum_{n,m=1}^{N_i+N_f}\eta_n Q_n\eta_m Q_m\frac{p_n^\mu p_m^\nu}{k\cdot p_n k\cdot p_m}|M_{fi}^0|^2. \tag{8}$$

This gives the probability of finding one soft photon of energy ω_k of the momentum four-vector k in a volume $d^3\boldsymbol{k}$ around $\boldsymbol{k}$. This is done by taking the absolute square of the leading term, so neglecting any terms of the order $\mathcal{O}(\omega_k^0)$, and summing over the two possible photon polarizations, $\lambda=\pm1$. Later integrating the result in section 2.2.2 will give the desired spectrum with which the expected number of emitted photons can be calculated.

2.2.1 Angular distribution

A handful of steps need to be taken to arrive at an expression for the angular distribution of the soft-photon spectrum. First, it is important to take note of the relations of the particle and photon four-vectors:

$$\begin{aligned} k &= (\omega_k, \boldsymbol{k}) = \omega_k(1, \hat{\boldsymbol{k}}), \\ p_n &= (E_n, \boldsymbol{p}_n) = E_n(1, \boldsymbol{\beta}_n). \end{aligned} \tag{9}$$

The four-vector product of a charged particle with the photon that is emitted then reads

$$k \cdot p_a = \omega_k E_a (1 - \boldsymbol{\beta}_a \cdot \hat{\boldsymbol{k}}). \tag{10}$$

The sum over physical photon polarizations can be expressed as

$$\sum_{\lambda=\pm 1} \epsilon_\mu(\boldsymbol{k}, \lambda)\epsilon^*_\nu(\boldsymbol{k}, \lambda) = -g_{\mu\nu} - \frac{k_\mu k_\nu}{(k \cdot n)^2} + \frac{k_\mu n_\nu + k_\nu n_\mu}{k \cdot n}, \tag{11}$$

which is a well-known result from QED, also called the photon completeness relation for free photons. It should be noted that $n_\mu = (1, \boldsymbol{0})$. When substituted in Eq. 8, this gives rise to the following terms:

$$\begin{aligned} -g_{\mu\nu} p_n^\mu p_m^\nu &= -(p_n^0 p_m^0 - \boldsymbol{p}_n \cdot \boldsymbol{p}_m), \\ k \cdot n &= k^0 \equiv \omega_k, \\ \tfrac{k_\mu k_\nu p_n^\mu p_m^\nu}{(k\cdot n)^2} &= (p_n^0 - \boldsymbol{p}_n \cdot \hat{\boldsymbol{k}})(p_m^0 - \boldsymbol{p}_m \cdot \hat{\boldsymbol{k}}), \\ \tfrac{k_\mu n_\nu p_n^\mu p_m^\nu}{k\cdot n} &= p_m^0(p_n^0 - \boldsymbol{p}_n \cdot \hat{\boldsymbol{k}}), \\ \tfrac{k_\nu n_\mu p_n^\mu p_m^\nu}{k\cdot n} &= p_n^0(p_m^0 - \boldsymbol{p}_m \cdot \hat{\boldsymbol{k}}), \\ (\hat{\boldsymbol{k}} \cdot \boldsymbol{p}_n)(\hat{\boldsymbol{k}} \cdot \boldsymbol{p}_m) &= \tfrac{(\boldsymbol{k}\cdot\boldsymbol{p}_n)(\boldsymbol{k}\cdot\boldsymbol{p}_m)}{\omega^2}. \end{aligned} \tag{12}$$

After some bookkeeping, the substitution of the photon polarization sum in Eq. 8 reads

$$\sum_{\lambda=\pm 1} \epsilon_\mu(\boldsymbol{k}, \lambda)\epsilon^*_\nu(\boldsymbol{k}, \lambda) p_n^\mu p_m^\nu = \boldsymbol{p}_n \cdot \boldsymbol{p}_m - \frac{(\boldsymbol{k} \cdot \boldsymbol{p}_n)(\boldsymbol{k} \cdot \boldsymbol{p}_m)}{\omega_k^2}. \tag{13}$$

Using the scalar quadruple product

$$(\boldsymbol{a} \times \boldsymbol{b}) \cdot (\boldsymbol{c} \times \boldsymbol{d}) = (\boldsymbol{a} \cdot \boldsymbol{c})(\boldsymbol{b} \cdot \boldsymbol{d}) - (\boldsymbol{a} \cdot \boldsymbol{d})(\boldsymbol{b} \cdot \boldsymbol{c}) \tag{14}$$

and noting $\hat{\boldsymbol{k}} \cdot \hat{\boldsymbol{k}} = 1$, the following relation can be written

$$\boldsymbol{\beta}_n \cdot \boldsymbol{\beta}_m - (\boldsymbol{\beta}_n \cdot \hat{\boldsymbol{k}})(\boldsymbol{\beta}_m \cdot \hat{\boldsymbol{k}}) = (\boldsymbol{\beta}_n \times \hat{\boldsymbol{k}}) \cdot (\boldsymbol{\beta}_m \times \hat{\boldsymbol{k}}). \tag{15}$$

This is then used to rewrite the polarization sum once again to

$$\sum_{\lambda=\pm 1} \epsilon_\mu(\boldsymbol{k}, \lambda)\epsilon^*_\nu(\boldsymbol{k}, \lambda) p_n^\mu p_m^\nu = \boldsymbol{p}_n \cdot \boldsymbol{p}_m - \frac{(\boldsymbol{k} \cdot \boldsymbol{p}_n)(\boldsymbol{k} \cdot \boldsymbol{p}_m)}{\omega_k^2} = E_n E_m (\boldsymbol{\beta}_n \times \hat{\boldsymbol{k}}) \cdot (\boldsymbol{\beta}_m \times \hat{\boldsymbol{k}}). \tag{16}$$

The angular dependence of the soft-photon spectrum now starts to become more obvious. With $d^3\boldsymbol{k} = \omega_k^2 d\omega_k d\Omega_{\boldsymbol{k}}$, where $\Omega_{\boldsymbol{k}}$ is the soft-photon solid angle, the probability density now reads

$$dI = \alpha \frac{d\omega_k}{\omega_k} \frac{d\Omega_{\boldsymbol{k}}}{(2\pi)^2} \sum_{n,m=1}^{N_i+N_f} \eta_n Q_n \eta_m Q_m \frac{(\boldsymbol{\beta}_n \times \hat{\boldsymbol{k}}) \cdot (\boldsymbol{\beta}_m \times \hat{\boldsymbol{k}})}{(1 - \boldsymbol{\beta}_n \cdot \hat{\boldsymbol{k}})(1 - \boldsymbol{\beta}_m \cdot \hat{\boldsymbol{k}})} |M_{fi}^0|^2, \tag{17}$$

where $\alpha = e^2/(4\pi)$. It is now also clear that the so-called dead-cone effect is present in this formula too through the denominator. To describe the angular distribution of soft photon radiation around a single charged particle with charge Q, mass m and energy E, the following relations are used

$$\begin{gathered}(\boldsymbol{\beta} \times \hat{\boldsymbol{k}}) = |\hat{\boldsymbol{k}}|^2 |\boldsymbol{\beta}|^2 \sin\theta^2 \\ 1 - \boldsymbol{\beta} \cdot \hat{\boldsymbol{k}} = 1 - |\boldsymbol{\beta}| \cos\theta\end{gathered} \tag{18}$$

to get

$$dI = \alpha Q^2 \frac{d\omega_k}{\omega_k} \frac{d\Omega_{\boldsymbol{k}}}{(2\pi)^2} \frac{|\boldsymbol{\beta}|^2 \sin\theta^2}{(1 - |\boldsymbol{\beta}| \cos\theta)^2} |M^0_{fi}|^2. \tag{19}$$

In the dead cone, the small-angle radiation is suppressed, $\theta \lesssim \theta_0$, where $\theta_0 = 1/\gamma$. To see the shape of the distribution, some expansions need to be done:

$$\begin{gathered}|\boldsymbol{\beta}| = \sqrt{1 - \tfrac{1}{\gamma^2}} = 1 - \tfrac{1}{2\gamma^2} = 1 - \tfrac{1}{2}\theta_0^2 + \ldots \\ \cos\theta = 1 - \tfrac{1}{2}\theta^2 + \ldots \\ \sin\theta = \theta + \ldots.\end{gathered} \tag{20}$$

In addition, note that

$$d\Omega_{\boldsymbol{k}} = \sin\theta d\theta d\phi, \tag{21}$$

and that the integral over ϕ gives rise to a factor 2π. Plugging this all in and showing the steps in between quickly becomes a lengthy expression, so here it is split up by numerator and denominator:

$$\begin{gathered}|\boldsymbol{\beta}|^2 \sin\theta^3 = (1 - \theta_0^2/2)^2 \theta^3, \\ (1 - |\boldsymbol{\beta}| \cos\theta)^2 = \tfrac{1}{4}(\theta^2 + \theta_0^2 - \theta^2\theta_0^2/2)^2.\end{gathered} \tag{22}$$

Then it is important to note for ultrarelativistic particles $\theta_0 \ll 1$ and $\theta \ll 1$, such that

$$\begin{gathered}\theta_0^2 \theta^3 \ll \theta^3, \\ \theta_0^2 \theta^2 \ll \theta_0^2 + \theta^2.\end{gathered} \tag{23}$$

Plugging this all in finally gives the sought-after angular distribution,

$$dI = \alpha Q^2 \frac{d\omega_k}{\omega_k} \frac{d\theta}{2\pi} \frac{4\theta^3}{(\theta^2 + \theta_0^2)^2} |M^0_{fi}|^2. \tag{24}$$

To calculate the angle at which the soft-photon spectrum reaches a maximum, the derivation with respect to θ is performed,

$$\frac{d}{d\theta} \frac{\theta^3}{(\theta^2 + \theta_0)^2}\Big|_{\theta=\theta_{\max}} = \frac{\theta^2_{\max}(3\theta_0^2 - \theta^2_{\max})}{(\theta^2_{\max} + \theta_0^2)^3} = 0. \tag{25}$$

The maximum is then reached at

$$\theta_{\max} = \sqrt{3}\theta_0 = \sqrt{3}/\gamma \tag{26}$$

with respect to the ultrarelativistic charged particle.

2.2.2 Photons emitted per event

To calculate the number of photons emitted per event Eq. 8 is again considered. Here the sum over the photon polarizations, Eq. 11, is inserted. Because of the Ward identity of QED, the terms $k_\mu k_\nu$, $k_\mu n_\nu$ and $k_\nu n_\mu$ vanish, leaving $-g_{\mu\nu}$, which gives

$$dI = \frac{\alpha}{(2\pi)^2} \frac{d^3\boldsymbol{k}}{\omega_k} \sum_{n,m=1}^{N_i+N_f} \eta_n Q_n \eta_m Q_m \frac{-p_n \cdot p_m}{(k \cdot p_n)(k \cdot p_m)} |M^0_{fi}|^2. \tag{27}$$

Here several steps are needed to get to the stage where the invariant yield of internal bremsstrahlung photons from colliding particles going to n final states for a single event can be easily calculated. First it is noted that

$$d^3\boldsymbol{k} = \omega_k^2 d\omega_k \sin\theta d\theta d\phi, \tag{28}$$

to get

$$\frac{dI}{d\omega_k d\theta d\phi} = \frac{\alpha}{(2\pi)^2}\sin(\theta)\omega_k \sum_{n,m=1}^{N_i+N_f} \eta_n Q_n \eta_m Q_m \frac{-p_n \cdot p_m}{(k\cdot p_n)(k\cdot p_m)} |M^0_{fi}|^2. \tag{29}$$

To have this as a function of pseudorapidity[3], the relation

$$\left|\frac{d\eta}{d\theta}\right| = \cosh\eta \tag{30}$$

is used to get

$$\frac{dI}{d\omega_k d\eta d\phi} = \frac{\alpha}{(2\pi)^2}\frac{\omega_k}{\cosh^2\eta} \sum_{n,m=1}^{N_i+N_f} \eta_n Q_n \eta_m Q_m \frac{-p_n \cdot p_m}{(k\cdot p_n)(k\cdot p_m)} |M^0_{fi}|^2. \tag{31}$$

To then write this more compactly,

$$\sum_{n,m=1}^{N_i+N_f} -\frac{p_n p_m}{(k\cdot p_n)(k\cdot p_m)} = -\left(\sum_{n=1}^{N_i+N_f} \frac{p_n}{k\cdot p_n}\right)^2, \tag{32}$$

is used to get to

$$\frac{dI}{d\omega_k d\eta d\phi} = -\frac{\alpha}{(2\pi)^2}\frac{\omega_k}{\cosh^2\eta}\left(\sum_{n=1}^{N} \eta_n Q_n \frac{p_n}{p_n\cdot k}\right)^2 |M^0_{fi}|^2. \tag{33}$$

Following the steps in Ref. [19], where the relation between Feynman amplitudes and cross sections are used, the expression for the number of emitted photons is retrieved,

$$\frac{dN_\gamma}{d\omega_k d\eta d\phi} = -\frac{\alpha}{(2\pi)^2}\frac{\omega_k}{\cosh^2\eta}\int d^3\boldsymbol{p}_1 \ldots d^3\boldsymbol{p}_{N_f}\left(\sum_{n=1}^{N} \eta_n Q_n \frac{p_n}{p_n\cdot k}\right)^2 \frac{dN_{\text{hadrons}}}{d^3\boldsymbol{p}_1 \ldots d^3\boldsymbol{p}_{N_f}} \tag{34}$$

And then, for a single event the number of photons produced per interval of the energy of the emitted photon, azimuthal angle and pseudorapidity is given by

$$\frac{d^3N_\gamma}{d\omega_k d\eta d\phi} = -\frac{\alpha}{(2\pi)^2}\frac{\omega_k}{\cosh^2\eta}\left(\sum_{n=1}^{N_i+N_f} \eta_n Q_n \frac{p_n}{k\cdot p_n}\right)^2 \sim \frac{1}{\omega_k}. \tag{35}$$

This formula shows some interesting properties, like the $1/\omega_k$ dependence, where ω_k is the energy of the emitted photon. This dependence follows from

$$k\cdot p = \omega(E - |\mathbf{p}|\cos\theta). \tag{36}$$

The $1/\omega_k$ dependence implies a divergence that caused a great crisis in the infrared regime of physics were it not for Ref. [23] where it was shown that the total energy radiated is not violated. Another interesting property is that the production of photons can be entirely attributed to the acceleration of charged particles. This property can be seen when studying the four-vectors. Through the numerator and denominator, the energy of the particle drops out, like

$$\frac{p}{E} = \begin{pmatrix} 1 \\ \vec{p}/E \end{pmatrix} = \begin{pmatrix} 1 \\ \vec{\beta} \end{pmatrix}. \tag{37}$$

The fraction is then only dependent on the velocity of the charged particle since $\vec{p} = \vec{\beta}\gamma m$ and $E = \gamma m$. This reflects the notion that the initial- and final-state particles are considered to gain this velocity as a result of the interaction, i.e. the transition the particles undergo. Charge between initial- and final-state particles is conserved in these interactions, but the number of initial-state particles, N_i, and final-state particles, N_f, can be different from each other.

[3]Which is more convenient later on

2.3 Simulating the Low photon spectrum

Eq. 35 makes it easy to calculate the number of photons produced on an event-by-event basis, but it is also easy to use when integrated with event generators like PYTHIA [9]. PYTHIA does not calculate the internal bremsstrahlung spectrum when used for event generation. PHOTOS [24], [25] generates the decay bremsstrahlung spectrum and can be integrated with Monte Carlo (MC) generators like PYTHIA, but it is not tailored to $m \to n$ processes which are considered in this work. To that end an add-on for PYTHIA was developed, called the "Low Photon Generator" (LPG) [26]. Since the internal bremsstrahlung spectrum can be calculated as a function of the initial- and final-state charged particles, this is what the LPG does too. It gets passed the stack of event particles from PYTHIA and based on that calculates the number of soft photons produced. It then generates and adds these photons to the PYTHIA event stack and they can then be used for further simulation purposes, like propagation through a detector setup. The LPG can be used standalone with PYTHIA, or in an O^2 simulation as an external generator. O^2 is the reconstruction, calibration and simulation and software of ALICE [27] which will be covered in Sec. 5.

To calculate the expected number of photons emitted in a certain pseudorapidity, azimuthal and photon energy range, Eq. 35 needs to be integrated over η, ϕ and ω_k. For the energy of the emitted photon this can be done analytically, but for η and ϕ it is tricky to do even a numerical integration due to the nature of the function which is strongly peaked in the $[\eta, \phi]$ range close to the charged particle. To do a proper numerical integration, the grid density of $[\eta, \phi]$ needs to be fine enough such

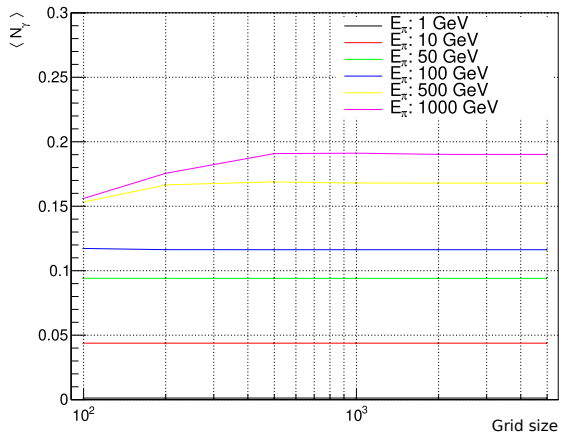

(a) Result of the numerical integration for the expected number of photons for pions of different energies as function of the grid size used for the LPG. The graph for pions with an energy of $E = 1\,\text{GeV}$ is present, but its value is very close to 0.

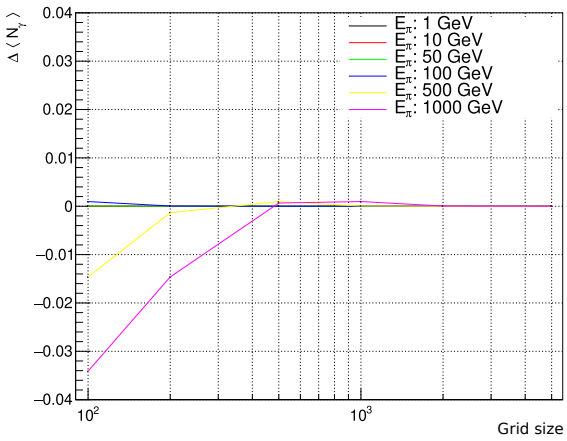

(b) The difference in the result of the numerical integration for the expected number of photons for pions of different energies for the selected grid size and the largest grid size (5000) used for the LPG. For lower energies, this difference is very close to 0.

Figure 1

that the value of the peaks are properly accounted for, but not so fine that it significantly slows down the execution time. To choose a proper grid size, the function is numerically evaluated for pions at different momenta and grid sizes, as shown in Fig. 1a. The difference in the result of the numerical integration for the expected number of photons between the selected grid size and largest (5000) grid size, $\Delta\langle N_\gamma \rangle$, is then plotted in Fig. 1b. As can be seen, the result of the numerical integration for pions with an energy up to $E = 100\,\text{GeV}$ remains constant when a grid size of $[\eta, \phi] = [100, 100]$ or more is selected. For pions with an energy $E > 100\,\text{GeV}$, the result of the numerical integration starts to be depended on the grid size, up to a certain grid size where it then remains constant again. As can be seen in Fig. 2a and 2b, the occurrences of pions exceeding $p > 100\,\text{GeV}/c$ are rare. These figures show the momentum spectra of the most common final-state charged particles retrieved from doing PYTHIA simulations of proton-proton collisions at $\sqrt{s} = 14\,\text{TeV}$. Even though a grid size of $[100, 100]$ is probably sufficient, a grid size of $[250, 250]$ was chosen for the simulations performed in this thesis.

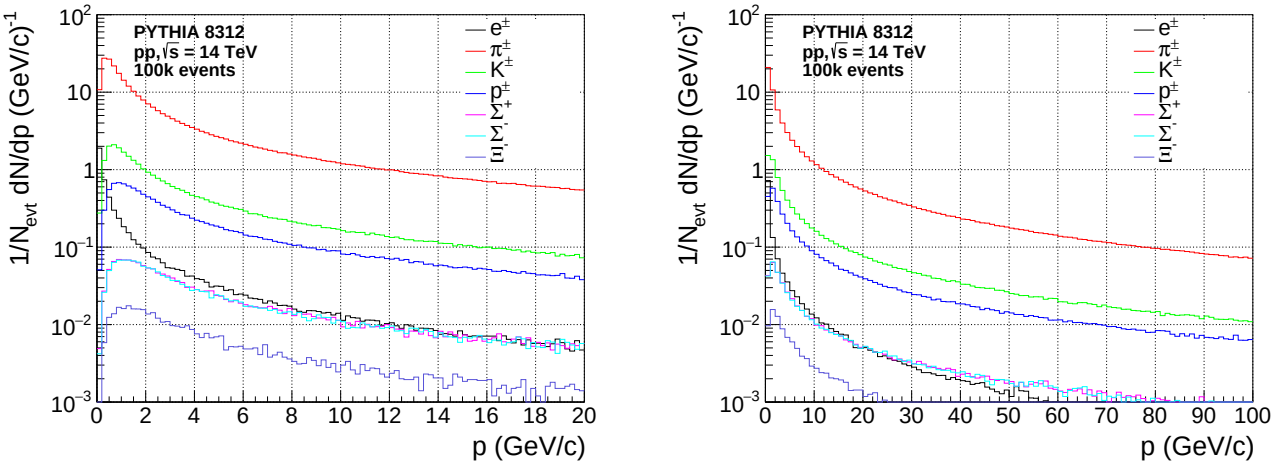

(a) (b)

Figure 2: Momentum spectra of the most common charged particles for $\sqrt{s} = 14\,\text{TeV}$ collisions. The simulations were carried out with PYTHIA.

Once the number of expected photons for a single event over a certain $[\eta, \phi, E]$ range is calculated, $\langle N_\gamma \rangle$, the number of photons emitted is drawn from a Poisson distribution with $\mu = \langle N_\gamma \rangle$. For each emitted photon, the energy, pseudorapidity and azimuthal angle need to be drawn from the probability distribution of Eq. 35. For the energy this is straightforward due to the $1/\omega_k$ dependence. For η and ϕ this is done through rejection sampling. In order for rejection sampling to work properly a proposal distribution Y needs to be selected. This is not trivial due to the sharply peaked nature of the function, but comparing peak values of a coarse grid for multiple simulated events (e.g. $[100, 100]$) with a fine grid (e.g. $[1000, 1000]$) showed that these values did not differ more than a factor 3 from each other. A proposal function Y with a uniform probability density of 3 times the peak value of the grid is then chosen for the event in question and rejection sampling is performed. There were very few cases in which this difference exceeded a factor 3, but it was found that this did not impact the accuracy. The transverse momentum spectrum of the internal bremsstrahlung for different regions in pseudorapidity was simulated and fitted with a a/k_T function[4] where a is the free parameter and shown in Figs. 3a, 3b, 3c, 3d, 3e, 3f. A cross-check with Ref. [28] was performed and it was found that the LPG agrees well with the results presented there[5]. Tab. 2 shows the comparison of the value for a between reported results and results retrieved from the simulations performed in this thesis.

[4]Since Eq. 35 $\sim 1/\omega$, it follows the same relation for k_T

[5]In the presentation, Eq. 35 is mentioned, but a factor 2 was missing because of a typo. In private conversation it was confirmed that the analytical calculation in the code that performed this did have the correct factorization.

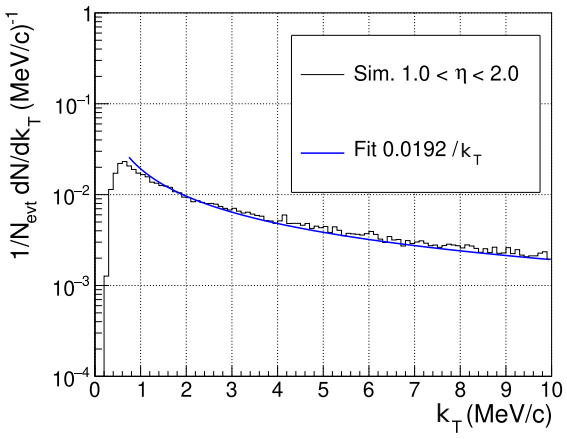

(a)

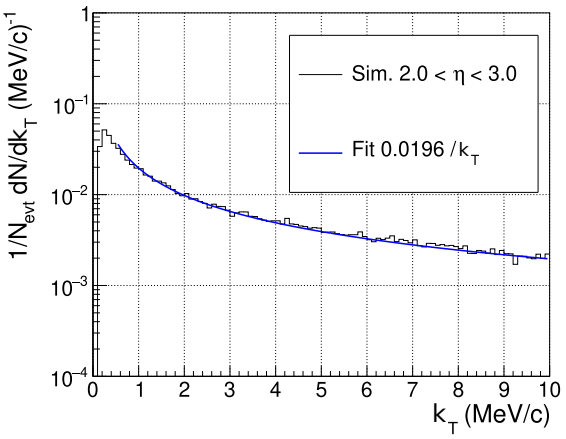

(b)

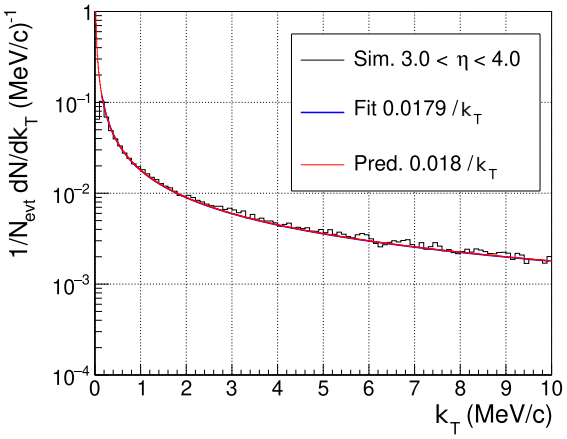

(c)

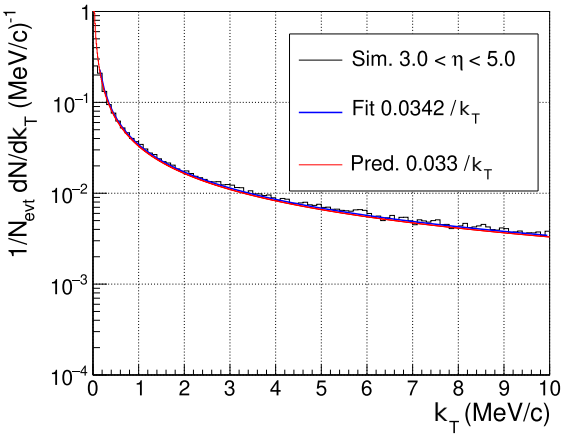

(d)

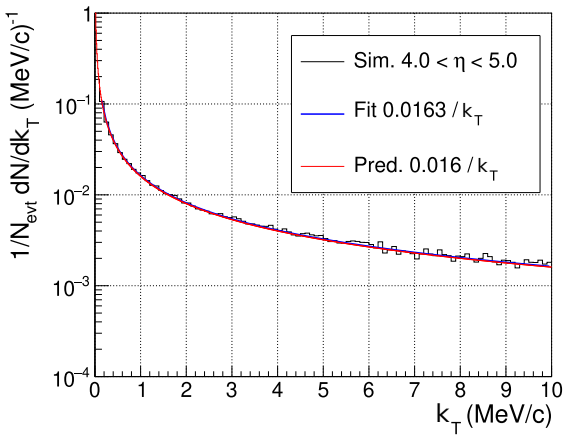

(e)

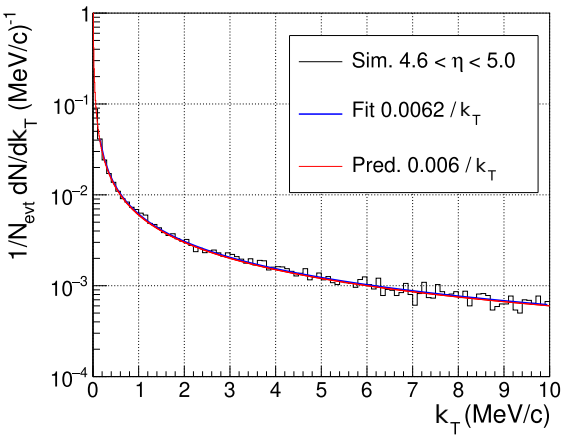

(f)

Figure 3: The internal bremsstrahlung spectrum generated with the LPG for different regions of pseudorapidity and compared to Ref. [28]. The minimum energy of an emitted photon was set to 1 MeV in the LPG which causes the drop of the intensity in the pseudorapdity regions $1 < \eta < 2$ and $1 < \eta < 2$ due to the relation $E = k_{\mathrm{T}} \cosh \eta$. The fits regions were defined through this relation.

Pseudorapidity	Reported fit value	Simulated fit value
$1 < \eta < 2$	-	0.0192
$2 < \eta < 3$	-	0.0196
$3 < \eta < 4$	0.018	0.0179
$3 < \eta < 5$	0.033	0.0342
$4 < \eta < 5$	0.016	0.0163
$4.6 < \eta < 5$	0.006	0.0062
$5 < \eta < 6$	-	0.0116

Table 2: Comparison between the reported fit values of the internal bremsstrahlung spectrum for various pseudorapidity regions of a previous study versus the values presented in this thesis.

2.3.1 Some simulated events

Figs. 4a and 4b show the photon density calculated with the LPG as function of the pseudorapidity and azimuthal angle of two events generated with PYTHIA. These density plots show the dead cone effect

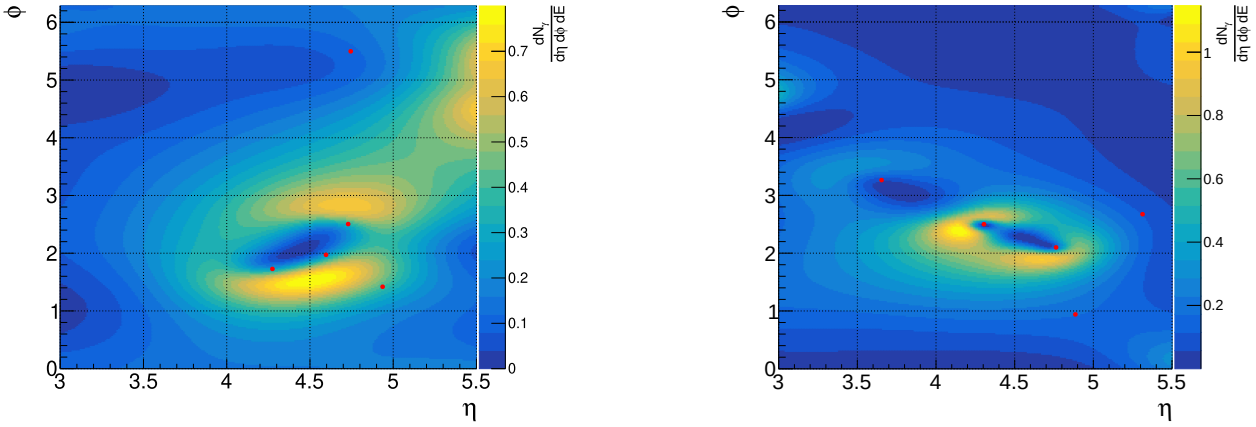

(a) (b)

Figure 4: Photon density plots simulated with the LPG for two events generated with PYTHIA. The dead-cone effect and interference patters are visible in these displays. The red dots indicate the charged particles with an energy $E > 2\,\text{GeV}$.

of the emission angle around charged particles and the interference patterns nicely. Both figures show a bright circular-like structure that (partially) surrounds a darker spot where the expected photon density is almost 0. In the case of Fig. 4b, the interference pattern between two charged particles can be seen as a sort of "bridge" between the two bright spots. Both these figures have a relatively low charged particle multiplicity to show case these specific structures. If the charged particle multiplicity becomes higher, it is more difficult to spot the relation between the position of the charged particles in $[\eta, \phi]$ and the structures.

2.3.2 Dead cone effect

In the paper by DELPHI [7], the angular distribution of internal bremsstrahlung coming from a muon with $\Gamma = 4.3 \times 10^2$ was calculated and plotted. The data from that figure were extracted and are plotted in this thesis alongside the distribution that is obtained when the LPG is used for a similar muon in Fig. 5.

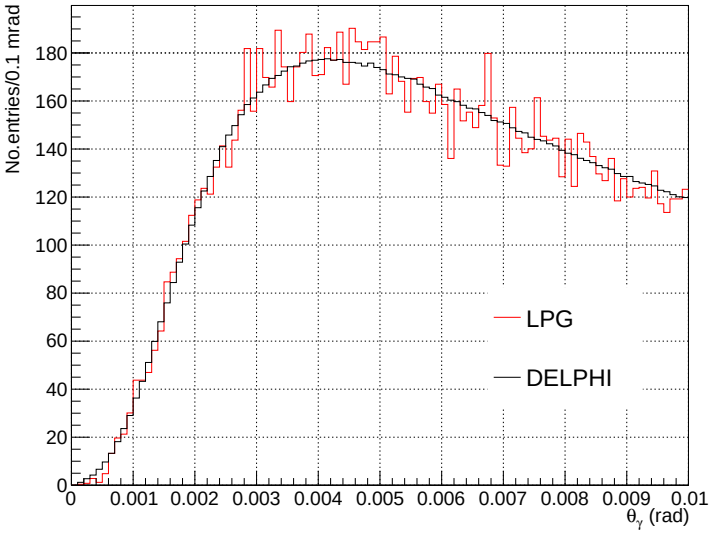

Figure 5: Comparison of the angular distribution around a muon with $\Gamma = 4.3 \times 10^2$ generated with the LPG (red) and reported by DELPHI (black) [7].

The simulation was done by creating a back-to-back PYTHIA event of two muons with $\Gamma = 4.3 \times 10^2$ and forcing the LPG to emit 10^5 photons in a chosen $[\eta, \phi]$ range around one of the charged particles. The angle of every photon with respect to the muon in question is then plotted. The distribution is then scaled with a factor a to match that of DELPHI[6]. From Eq. 26, the maximum of this distribution is at $\theta_{\max} = \sqrt{3}/\gamma \approx 0.004\,\text{rad}$, which is in agreement with the distribution retrieved from the LPG. The shape of both distributions also match nicely, including statistical fluctuations.

2.4 Transverse momentum as qualification of a soft photon

Low's theorem predicts the soft-photon spectrum as long as the photon that is emitted is low in energy compared to the particle that emits it. This in and of itself is a rather vague statement, because the question then arises what "low energetic" means, and in particular where this cutoff is supposed to be. Gribov argued in a paper [29] that the k_{T} of the photon also qualifies the emitted photon to be a soft photon. It is, however, not always clear from previous papers whether this was properly defined in their analysis. It is suspected that during the analysis this was considered to be "obvious", but reading the papers does not always convey the "obvious". In the jet studies of DELPHI [17], this was made explicitly clear by the fact that they took the jet axis as the direction to which they related the transverse momentum of the soft photon. To this end, it is important to be clear what is understood and meant with transverse momentum of the soft photon in this work. The FCT of ALICE 3 will be placed in the forward direction, namely to cover the pseudorapidity region of $4 < \eta < 5$. Through the geometric relation of

$$E = k_{\text{T}} \cosh \eta \tag{38}$$

the energy of the photon can be calculated. As η increases, k_{T} can stay small as the energy increases, satisfying Gribov's argument for the qualification of soft photons and causing the photons to be able to convert to trackable e^+e^- pairs. Again, this would be the transverse momentum of said photon with respect to the charged particle that emitted it. However, the measurement of the charged particle that emitted the photon is often a challenge. And for the FCT this is no different. The geometry of ALICE 3, which will be discussed in detail in coming sections, makes the tracking of charged particles that are produced in non-diffractive pp collisions extremely difficult in the pseudorapidty region of $4 < \eta < 5$. Simply put, there are no, or almost no, sensitive volumes available between the the primary

[6]From the paper it was unclear over which energy range they integrated to obtain this distribution, so an arbitrary scaling was chosen

vertex and the FCT to provide tracking for the charged particles produced in this pseudorapidity region. In addition, the solenoidal magnetic field bends the tracks of these charged particles, which in turn destroys the spatial correlation of the photons that travel unaffected by the magnetic field from the primary vertex to the FCT and the charged particles that emitted them. DELPHI [17] wanted to solve this by measuring the charged particles in a jet and the photons that were then consequently emitted as a result of the acceleration of said charged particles. They, like other previous experiments, also measured an excess of the soft-photon spectrum. For this work, the transverse momentum of the measured photons is quoted with relation to the beam axis. In this forward regime, the angle between the soft-photons and the beam axis is very small. Through the relation of the pseudorapidity and the angle in radians,

$$\theta(\eta) = 2 \arctan e^{-\eta}, \tag{39}$$

the angle between the beam axis for $\theta(4) = 37\,\text{mrad}$ and for $\theta(5) = 13\,\text{mrad}$. DELPHI [17] considered a resolution of the angle of the jet axis with respect to the photon to be around 50–60 mrad. This is partially due to the smearing of the jet axis because its definition of the weighted sum of the monument of all participating particles. In other fixed target experiments, the soft photon spectrum was measured at an angle of 20 mrad with respect to the beam axis. They also measured an excess. For the FCT, these values are very similar.

The spectrum of $\pi^0 \to \gamma\gamma$ dominates the hadronic decay photon spectrum and also the soft-photon spectrum coming from inelastic scattering processes at larger k_T. Since the $\pi^0 \to \gamma\gamma$ decay spectrum scales as

$$\frac{dN_\gamma}{dk_\text{T}} \sim \frac{2k_\text{T}}{m_{\pi^0}} \frac{1}{\sqrt{\left(\frac{m_{\pi^0}}{2}\right)^2 - k_\text{T}^2}}, \tag{40}$$

also known as the Jacobian Peak, and the internal bremsstrahlung spectrum with $\sim 1/k_\text{T}$, there is a region in low transverse momentum where the internal bremsstrahlung spectrum dominates. The external bremsstrahlung caused by charged particles[7] traversing detector material, which has the same $1/E$ shape as the internal bremsstrahlung, dominates the internal bremsstrahlung for the setup with the FCT in ALICE 3. In the next chapters, a strategy will be laid out how to deal with the external bremsstrahlung spectrum.

2.5 The Haissinski formula

The Haissinski formula is also often used [13], [14], [15], [16] to predict the soft-photon spectrum. It reads

$$\frac{dN_\gamma}{d^3k} = \frac{\alpha}{(2\pi)^2} \frac{1}{\omega_\gamma} \int d^3\mathbf{p}_1 ... d^3\mathbf{p}_{N_f} \left(\sum_{n=1}^{N_i+N_f} \eta_n Q_n \frac{\mathbf{p_n}_\perp}{p_n \cdot k} \right)^2 \frac{dN_\text{hadrons}}{d^3\mathbf{p}_1 ... d^3\mathbf{p}_{N_f}}, \tag{41}$$

where $\mathbf{p_n}_\perp = \mathbf{p_n} - (\mathbf{n} \cdot \mathbf{p_n}) \cdot \mathbf{n}$, $\mathbf{p_n}$ the charged particle three-momentum vector and $\mathbf{n}$ is the photon unit vector, $\mathbf{n} = \mathbf{k}/|\mathbf{k}|$. This form was proposed by Haissinski *et al.* [30] by modifying Low's leading power formula and it said to be more stable in use when not all intial- and final-state charged particles involved in a $m \to n$ scattering process can be measured due to detector effects. When used with Monte Carlo generators where all charged particles involved are known, the outcomes are said to be in complete agreement. Low's theorem requires all charged particles involved to be known, but for Haissinski's this requirement does not exist. Low's theorem occasionally and not infrequently predicts a negative number of predicted photons when the charged particles considered are limited to a certain range in pseudorapidity. Haissinski's formula does not suffer from this, but predicts less photons when the charged particles considered are limited to a certain range in pseudorapidity. This will be shown in more depth in the next paragraph. Ideally, to test Low's formula, one would set up an experiment where all charged particles can be measured, but as stated in the previous subsection, this is very challenging, if not impossible at ALICE 3. However, predictions about the spectrum in certain pseudorapidty ranges can still be made by simulating non-diffractive pp collisions, as is done

[7] mostly electrons

in this thesis. Haissinski's formula, unfortunately, also seems a bit impractical to use when even a part of the charged particles are measured. Perhaps when all charged particles in the pseudorapidty range of the FCT can be tracked by the IRIS tracker can the Haissinski formula be used, but very high momentum particles would need to be tracked with the outer tracker, which unfortunately does not cover the same pseudorapidity region as the FCT. In addition, to extract the momentum of the particles from their tracks, a way to identify the particles would need to be present.

Using the Haissinski formula instead of Low's formula in the event generator, the aptly named Haissinski Photon Generator (HPG) is made. In essence, it functions the same as the LPG, but a defining difference is that it allows the user to select the range of charged particles in η to predict the internal bremsstrahlung spectrum. Comparing the predicted photon density with both generators has satisfying results, as shown in Fig. 6. For Low's theorem, all charged particles need to be known which is

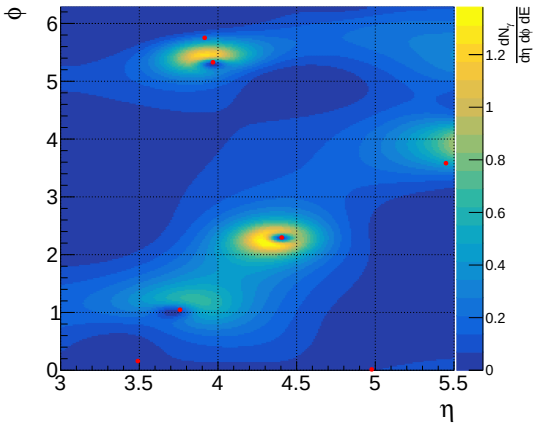

(a) The photon density plot as simulated with the LPG according to Low's theorem.

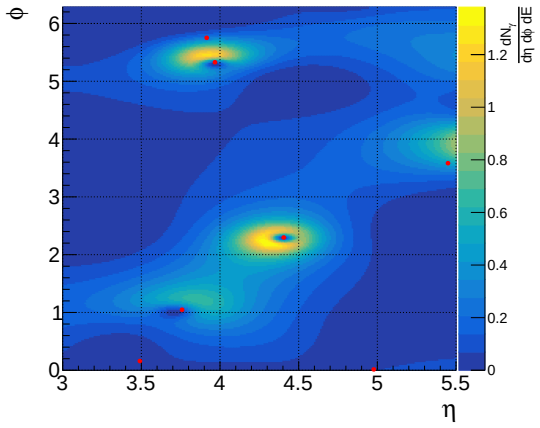

(b) The photon density plot as simulated with the HPG with Haissinski's formula.

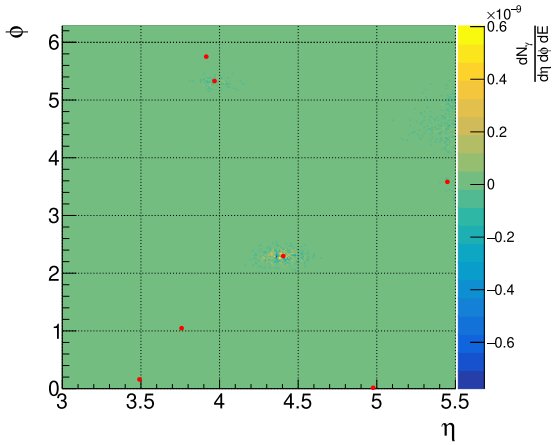

(c) The photon density as predicted by the HPG subtracted from the photon density predicted by the LPG.

Figure 6: Comparison plots of the predicted photon density by the LPG and HPG when both are given full access to all initial- and final-state charged particles involved in the scattering processes.

easily achieved with a MC generator. For Haissinski's formula, this is not necessary. However, when all charged particles are used in both formulas, the predicted photon spectra are in complete agreement, as shown in Fig.6c which shows the the photon density as predicted by the HPG subtracted from the photon density predicted by the LPG, up to a very high precision. The comparison of the predicted internal bremsstrahlung spectrum by the LPG and HPG is given in Fig. 7 for the pseudorapidity range $4 < \eta < 5$. The LPG takes all charged particles produced by the MC generator into account, i.e. PYTHIA, but the HPG only considers the charged particles produced in the pseudorapidity range

$4 < \eta < 5$. For this figure 100k events were simulated. Fig. 7b shows that the ratio between the the

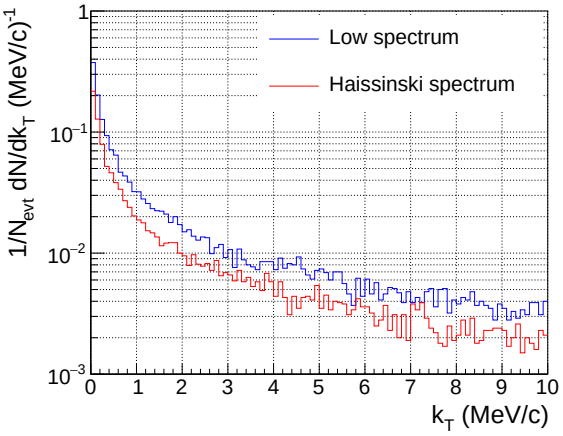

(a) Comparison of the predicted internal bremsstrahlung spectrum by the LPG (blue) and HPG (red) in the pseudorapidity range $4 < \eta < 5$. For the prediction with the HPG, the charged particles considered were limited to the same pseudorapidity range.

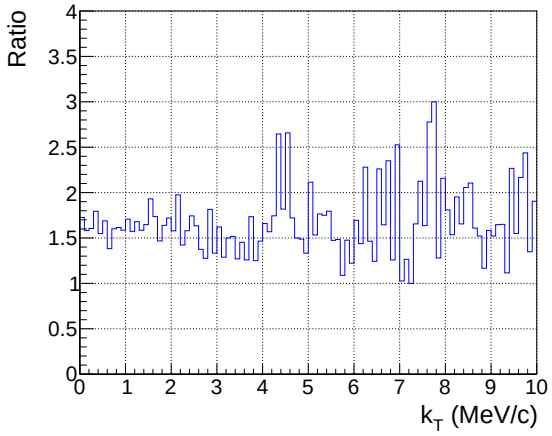

(b) Ratio of the predicted internal bremsstrahlung spectrum by the LPG and HPG (LPG/HPG).

Figure 7

predicted internal bremsstrahlung spectrum of the LPG and HPG is constant. This is an inherent attribute of these formulas: both predict the number of photons in a certain pseudorapidity range, but due to incomplete information of all involved charged particles, the Haissinki's formula predicted less photons in this pseudorapidity range because it only had access to the charged particles in that pseudorapidity range.

3 Previous measurements

Experiments in the past have measured the soft-photon spectrum in the low-k_{T} region as indicated by Tab. 1. From this table it can be read that the experiments that measured an excess in the soft-photon spectrum, measured this as a factor 4–8 in terms of the predicted internal bremsstrahlung spectrum. This table is great for a quick overview, but it does not show the full kinematic regime in which the experiments were conducted. Some experiments reported findings for multiple kinematic regimes and some have tighter constraints through the inclusion of the Feynman x. Tabs. 3 and 4 show a slightly more complete overview of the kinematic regime in which the experiments were conducted. In addition, the reported findings along with their expected signal-to-background ratio, so excluding any potential measured enhancement of the signal, are also given. Here, the expected signal is the expected internal bremsstrahlung spectrum and the expected background everything else. The measured signal is the measured data after the expected background has been subtracted.

Chliapnikov *et al.* [11] performed a fixed target experiment. They reported that the shape of the excess matches that of their predicted external bremsstrahlung spectrum in both Feynman x and k_T, the latter of which did not have a distribution present in the paper, but it was mentioned in the text. In addition, the excess shows a forward-backward asymmetry in the reported Feynman x regime, extending further into the forward direction than backward. Botterweck *et al.* [12] then showed the same forward-backward asymmetry, but for a higher beam energy, for both π^+p and K^+p collisions. They also reported the shape of the excess to match that of their predicted internal bremsstrahlung spectrum. Banerjee *et al.* [13] and Belogianni *et al.* [15] continued the trend and they reported that their excess also matches their predicted internal bremsstrahlung spectrum in shape. Belogianni *et al.*, however, limited the amount of charged tracks per event to be less than 8 to allow for their pattern recognition algorithm to work optimally. In a follow-up experiment at higher beam energy, Belogianni *et al.* [16] compared their findings of pp collisions to their previous experiment with π^-p collisions, Ref. [15]. They made predictions about the differences in the spectra and found that the excess shows similar features to those predictions. DELPHI [17] reported the slope of their found excess in k_{T}^2 to be a good estimation for the slope of their predicted internal hadronic bremsstrahlung. This was, however, difficult to see for their k_{T} spectrum, and it was also not reported by them. The similarity in shape of the excess and predicted internal bremsstrahlung spectrum of most of these reports suggests that the excess has something to do with the internal bremsstrahlung spectrum, however a reason to explain the forward-backward asymmetry of early fixed target experiments remains elusive as of yet.

Antos *et al.* [5], Tincknell *et al.* [6] and DELPHI [7] reported no noticeable, or an upper limit to the excess. A few things, however, stick out. Starting with Tincknell *et al.* where they used barium fluoride arrays (BAF1 and BAF2) to detect the photons. In front of these BAF1 and BAF2 detectors were veto counters to select neutral events in the offline analysis by requiring no charged particle fired the veto counter in front of the corresponding detector. Yet in their analysis they do mention an expected internal bremsstrahlung spectrum. Photons of such a spectrum, as shown in Sec. 2, are emitted under a small angle of a charged particle. It is unclear through the rest of the paper what impact the offline veto has on the internal bremsstrahlung spectrum. DELPHI performed their measurement of the internal bremsstrahlung spectrum with collisions of $\mathrm{e^+e^-} \to \mu^+\mu^-$, which is considered to be a very clean QED channel without any influence from QCD. This suggests a dependence of the excess on QCD, especially since the other experiment done by DELPHI [17], which measured $\mathrm{e^+e^-} \to n$ jets, did measure an excess. Antos *et al.* did not report a significant excess at all and this result adds to the puzzle.

Aubert *et al.* [31], not present in the overview tables, also reported an excess in the photon spectrum they measured. However, as they reported themselves, the photon energies measured in their report are higher than those reported in the other experiments that measured an excess in the soft-photon spectrum. They therefore stated themselves that it is unlikely that the excess has the same origin.

Experiment + year	p_{beam} or $\sqrt{s}$	Region Photon k_{T} and/or Feynmann x	$\gamma_{\text{meas}}/\gamma_{\text{brems}}$	Reported findings	$S_{\text{exp}}/B_{\text{exp}}$	Reference
π^+p 1979	10.5 GeV/c	$k_{\text{T}} < 20$ MeV/c $0 < x < 0.01$	1.25 ± 0.25	B_{exp} : 1006 photons S_{meas} : 840 ± 166 photons S_{exp} : 671 photons	0.67	Goshaw *et al.* [10]
K^+p WA27, CERN 1984	70 GeV/c	$k_{\text{T}} < 60$ MeV/c $-0.001 < x_\gamma < 0.008$	4.0 ± 0.8	B_{exp} : $13.3 \pm .5$ mb S_{meas} : 4.5 ± 0.9 mb S_{exp} : 1.1 mb	0.083	Chliapnikov *et al.* [11]
π^+p CERN, EHS, NA22 1991	250 GeV/c	$k_{\text{T}} < 40$ MeV/c	6.9 ± 1.5	B_{exp} : not reported S_{meas} : 8.2 ± 1.5 mb S_{exp} : 1.18 mb	0.04–0.05	Botterweck *et al.* [12]
π^+p CERN, EHS, NA22 1991	250 GeV/c	$-0.001 < x_\gamma < 0.008$	3.7 ± 1.7	B_{exp} : 29.24 mb S_{meas} : 5.9 ± 1.7 mb S_{exp} : 1.6 mb	0.05	Botterweck *et al.* [12]
K^+p CERN, EHS, NA22 1991	250 GeV/c	$k_{\text{T}} < 40$ MeV/c	6.4 ± 1.6	B_{exp} : not reported S_{meas} : 6.3 ± 1.6 mb S_{exp} : 0.98 mb	0.04–0.05	Botterweck *et al.* [12]
K^+p CERN, EHS, NA22 1991	250 GeV/c	$-0.001 < x_\gamma < 0.008$	4.1 ± 1.7	B_{exp} : 24.24 mb S_{meas} : 5.3 ± 1.7 mb S_{exp} : 1.3 mb	0.05	Botterweck *et al.* [12]
π^-p CERN, WA91, OMEGA 1993	280 GeV/c	$k_{\text{T}} < 10$ MeV/c $(0.2 < E_\gamma < 1$ GeV)	7.9 ± 1.4	B_{exp} : - S_{meas} : 1/6 of events S_{exp} : 2.1% of events	1.03–1.33	Banerjee *et al.* [13]
p-Be 1993	450 GeV/c	$k_{\text{T}} < 20$ MeV/c	< 2	B_{exp} : - S_{meas} : - S_{exp} : -	Insufficient information	Antos *et al.* [5]

Table 3: Overview one of two of experiments that measured the soft-photon spectrum.

Experiment + year	p_{beam} or $\sqrt{s}$	Region Photon k_{T} and/or Feynmann x	$\gamma_{\text{meas}}/\gamma_{\text{brems}}$	Reported findings	$S_{\text{exp}}/B_{\text{exp}}$	Reference
p-Be, p-W 1996	18 GeV/c	$k_{\text{T}} < 50$ MeV/c	< 2.65	B_{exp} : - S_{meas} : - S_{exp} : -	Insufficient information	Tincknell *et al.* [6]
π^-p CERN, WA91, OMEGA 1997	280 GeV/c	$k_{\text{T}} < 20$ MeV/c ($0.2 < E_\gamma < 1$ GeV)	7.8 ± 1.5	B_{exp} : 3.25 ± 0.09 % per event S_{meas} : $9.8 \pm 0.4 \pm 1.5$ % per event S_{exp} : 1.25 ± 0.05 % per event	0.38	Belogianni *et al.* [14]
π^-p CERN, WA91, OMEGA 2002	280 GeV/c	$k_{\text{T}} < 20$ MeV/c ($0.2 < E_\gamma < 1$ GeV)	5.3 ± 1.0	B_{exp} : 3.72 ± 0.05 % per event S_{meas} : $9.2 \pm 0.4 \pm 1.5$ % per event S_{exp} : 1.74 ± 0.03 % per event	0.47	Belogianni *et al.* [15]
pp CERN, WA102, OMEGA 2002	450 GeV/c	$k_{\text{T}} < 20$ MeV/c ($0.2 < E_\gamma < 1$ GeV)	4.1 ± 0.8	B_{exp} : 3.09 ± 0.09 % per event S_{meas} : $4.73 \pm 0.18 \pm 0.91$ % per event S_{exp} : 1.16 ± 0.02 % per event	0.31–0.38	Belogianni *et al.* [16]
$e^+e^- \to n$ jets CERN, DELPHI 2006	91 GeV ($\sqrt{s}$)	$k_{\text{T}} < 80$ MeV/c ($0.2 < E_\gamma < 1$ GeV)	$4.0 \pm 0.3 \pm 1.0$	B_{exp} : 0.987 γ/jet S_{meas} :$(69.1 \pm 4.5 \pm 15.7) \cdot 10^{-3}\,\gamma$/jet S_{exp} : $(17.10 \pm 0.01 \pm 1.21) \cdot 10^{-3}\,\gamma$/jet	0.017–0.018	DELPHI [17]
$e^+e^- \to \mu^+\mu^-$ CERN, DELPHI 2008	91 GeV ($\sqrt{s}$)	$k_{\text{T}} < 40$ MeV/c ($0.2 < E_\gamma < 1$ GeV)	$1.11 \pm 0.17 \pm 0.07$	B_{exp} : $(0.11) \cdot 10^{-3}\gamma/\mu$ S_{meas} : $(0.412 \pm 0.048 \pm 0.007) \cdot 10^{-3}\gamma/\mu$ S_{exp} : $(0.388 \pm 0.001 \pm 0.025) \cdot 10^{-3}\gamma/\mu$	3.5	DELPHI [7]
$e^+e^- \to \mu^+\mu^-$ CERN, DELPHI 2008	91 GeV ($\sqrt{s}$)	$k_{\text{T}} < 80$ MeV/c ($1 < E_\gamma < 10$ GeV)	$1.06 \pm 0.11 \pm 0.12$	B_{exp} : $(0.25) \cdot 10^{-3}\gamma/\mu$ S_{meas} : $(0.829 \pm 0.069 \pm 0.025) \cdot 10^{-3}\gamma/\mu$ S_{exp} : $(0.794 \pm 0.001 \pm 0.089) \cdot 10^{-3}\gamma/\mu$	3.2	DELPHI [7]

Table 4: Overview two of two of experiments that measured the soft-photon spectrum.

3.1 Some notes on the extraction of the values

Botterweck *et al.*

In Ref. [12], results were published for two kinematic regimes for both $\pi^+ p$ and $K^+ p$ collisions. For the kinematic regime of $k_\mathrm{T} < 40\,\mathrm{MeV}/c$, no exact value was quoted for the expected background in the text, nor was a transverse momentum range quoted for the kinematic regime of $-0.0001 < x_\gamma < 0.008$. It is thus unclear whether the overlap of both is fully compatible. Assuming the expected background to be of similar value in both kinematic regimes, an estimated range for the signal-to-background ratio has been given for the kinematic regimes of $k_\mathrm{T} < 40\,\mathrm{MeV}/c$ in Tab. 3. For the uncertainty on the $\gamma_\mathrm{meas}/\gamma_\mathrm{brems}$ the values for the uncertainty on the measurement of the signal, or excess as it is called in the paper, were adopted. Unfortunately, no uncertainty was quoted for the prediction of the internal bremsstrahlung for either kinematic ranges.

Banerjee *et al.*

In Ref. [13], no exact values for the measured excess were quoted except for the 2.1 % events that were expected to contain photons, but they measured that 1/6 did. This results in $\gamma_\mathrm{meas}/\gamma_\mathrm{brems} = 7.9$, the excess ratio that is quoted in the paper. For the expected signal to expected background ratio, the figures containing the data were imported in an online tool and the data points extracted, providing the range as quoted in Tab. 3. Performing this exercise showed that a 7.9 ratio was only to be retrieved when the kinematic range of $k_\mathrm{T} < 8\,\mathrm{MeV}/c$ was considered, whereas the paper quoted this for $k_\mathrm{T} < 10\,\mathrm{MeV}/c$. Due to this, the ratio $S_\mathrm{exp}/B_\mathrm{exp}$ is given in a range.

Antos *et al.*

In Ref. [5], the quoted $\gamma_\mathrm{meas}/\gamma_\mathrm{brems}$ ratio is given for many values of k_T, the uncertainty of which are not quoted. Like Ref. [19], the value is therefore quoted as < 2 in Tab. 3. No exact values were quoted in the text of the paper for the expected signal (excess) and background. An attempt was done to extract the data from the figures present in the paper, but due to the size of the markers and error bars on the data, the uncertainty introduced in the extraction process was too big to give a meaningful value for the ratio $S_\mathrm{exp}/B_\mathrm{exp}$.

Tincknell *et al.*

In Ref. [6], integrated values for their (expected) signal and background were not given. Instead, their results were predominantly presented in graphs for which the uncertainty introduced in an extraction process was too big to give a meaningful value for the ratio $S_\mathrm{exp}/B_\mathrm{exp}$.

Belogianni *et al.*, WA102

In Ref. [16], an upper bound was given for the production of photons from secondary interactions, the in- and exclusion of which determines the range for the ratio $S_\mathrm{exp}/B_\mathrm{exp}$ given in Tab. 4.

DELPHI $\mathrm{e}^+\mathrm{e}^- \to$ n jets

In Ref. [17], the data uncorrected and corrected for photon detection efficiency were given. These then determine the range of the ratio $S_\mathrm{exp}/B_\mathrm{exp}$ given in Tab. 4. The exact value for the expected background was not quoted, but this was calculated from the values quoted in the text. As such, an uncertainty on the expected background is not given in Tab. 4.

DELPHI $\mathrm{e}^+\mathrm{e}^- \to \mu^+\mu^-$

In Ref. [7], the exact values for the expected background were not quoted, but these were calculated from the values quoted in the text. As such, uncertainties on the expected background are not given in Tab. 4.

4 An introduction to ALICE 3 and the FCT

ALICE 3 is the proposed next-generation detector of the ALICE Collaboration for Run 5 & 6 when the LHC is in its high-luminosity phase, dubbed the HL-LHC. The installation of said detector is scheduled to take place during the fourth long shutdown (LS4, 2034-2035). The proposal for ALICE 3 was published in the Letter of Intent (LoI) [8] and the design considerations will be published in its upcoming Scoping Document (SD) [32]. Its layout, shown in Fig. 8, has been specifically curated to tackle some extraordinary open problems in physics, as well as improve and/or advance existing measurements. Advanced silicon detectors will give ALICE 3 its high readout rate, superb pointing

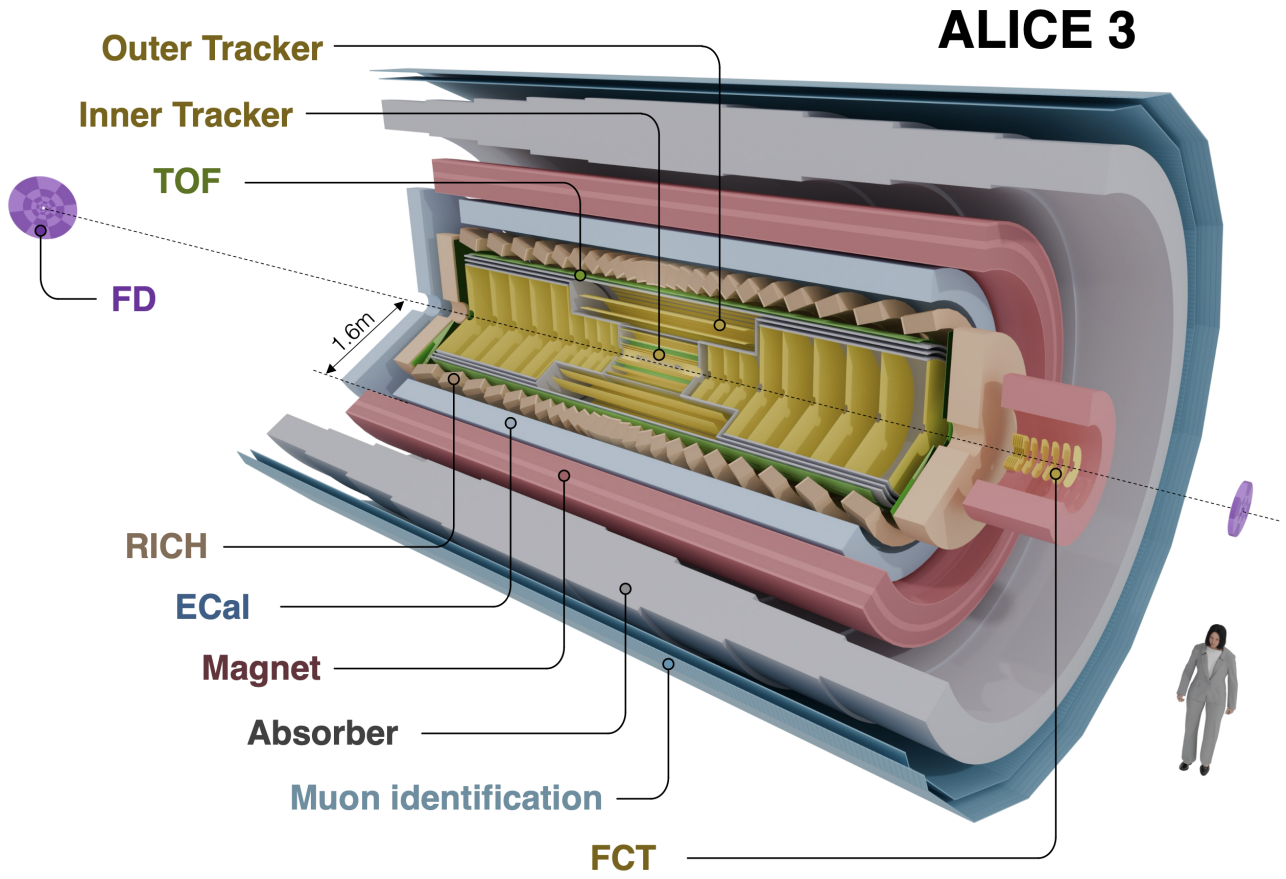

Figure 8: Prospected layout of the ALICE 3 detector as per the SD [32]. A few labels have been included to convey the general layout, but specific naming of all individual parts has been omitted to avoid cluttering of the figure. For a more complete overview, refer to Fig. 9.

resolution and excellent tracking over a large acceptance. To complement this, it will sport outstanding particle identification over the same acceptance.

To achieve its desired pointing resolution, the first tracking layer must be as close as possible to the interaction point. ALICE 3 does this by placing its vertex tracker (also nicknamed IRIS because of its resemblance of an optical diaphragm) inside the beam pipe. The IRIS tracker is composed of three cylindrical layers bent around the interaction vertex and 3 circular disks on either side. The silicon pixel sensors with which the tracking is performed are Complementary Metal-Oxide Semiconductor (CMOS) Monolithic Active Pixel Sensors (or MAPS for short). During beam injection of the LHC, the aperture required ($\sim$ 16 mm) is a lot larger than at stable beams ($\sim$ 5 mm). The IRIS tracker takes advantage of that fact by being retractable and when stable beams have been achieved it will settle in its contracted state. With an aperture of 5 mm in the contracted stated it will be ready for data taking.

The increase in luminosity plays a key role in achieving the prospected physics program of ALICE 3.

Based on the projections laid out in the Letter of Intent [8], the prospected nucleon-nucleon luminosity ALICE 3 will provide is more than five times larger than that is available with Pb-Pb collisions of Run 3 & 4 ($\sim 0.5\,\mathrm{fb}^{-1}$). Studies, e.g. the operation with lighter ions, are currently being undertaken to further increase this luminosity. For proton-proton interactions, ALICE 3 is prospected to operate at an instantaneous luminosity of $L = 3 \times 10^{32}\,\mathrm{cm}^{-2}\mathrm{s}^{-1}$, or an interaction rate of 24 MHz, corresponding to the accumulation of $3\,\mathrm{fb}^{-1}$ per operational year. The cutting edge MAPS will have a data acquisition rate to match this interaction rate. The pixel sensors of the IRIS tracker will be as thin as 0.1% of a radiation length X_0 to minimize multiple scattering of charged particles passing through them. They also sport a position resolution of $\sigma_{\mathrm{pos}} \approx 2.5\,\mu\mathrm{m}$.

While the IRIS tracker takes care of the vertex location and will provide information for track seeding, the outer tracker will be used to perform the tracking for the vast majority of the charged particles produced. The outer tracker consists of cylindrical "barrel" layers and forward disks, all made up of MAPS, but with a thickness of $1\%\,X_0$ and a position resolution of $\sigma_{\mathrm{pos}} \approx 10\,\mu\mathrm{m}$. Together, they will provide the outer tracker with an acceptance of $|\eta| < 4$. A radial projection of the layout of ALICE 3 is depicted in Fig. 9, where the barrel layers are colored cyan and the disks olive green. All the other components, as well as some of the passive material, have been given their own label.

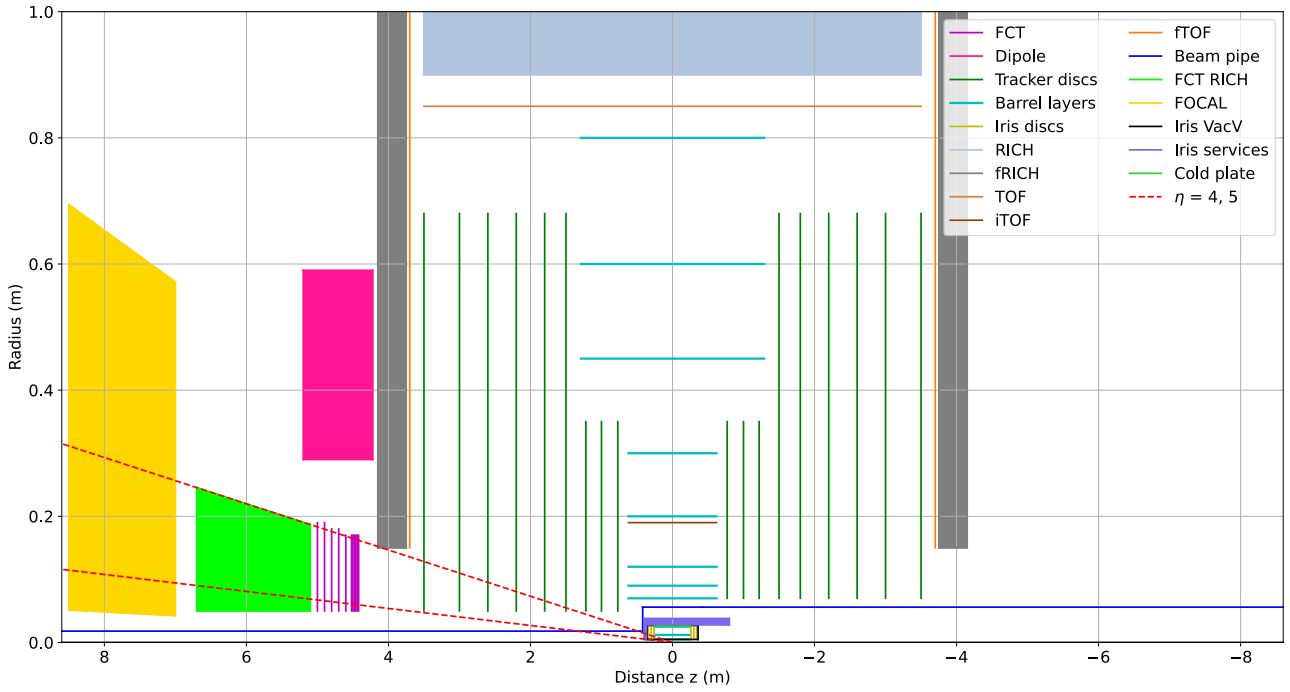

Figure 9: A schematic overview of the layout of ALICE 3 as seen from the radial-z point of view. The FCT (purple) is placed at the A side [33]. The ECAL, magnet, absorbers and muon chambers are outside of this radial projection. The acceptance in pseudorapidity of the FCT is given by the red, dotted lines.

Particle identification is performed by the combination of the inner, outer and forward Time-of-Flight (iTOF, TOF and fTOF respectively) detectors with a time resolution of 20 ps. The TOF will provide electron/hadron separation of up to $500\,\mathrm{MeV}/c$ and π/K separation up to $2\,\mathrm{GeV}/c$. To identify particles below $300\,\mathrm{MeV}/c$, the iTOF will be used. This is complemented by the Ring-Imaging Cherenkov (RICH), which consists of the barrel RICH (RICH) and forward RICH (fRICH), to extend the range for e/π separation up to $2\,\mathrm{GeV}/c$, and of protons from e, π, K up to $14\,\mathrm{GeV}/c$. For muons, a dedicated muon detector after a steel absorber will be installed. A solenoid magnet will provide ALICE 3 with a magnetic field of 2 T. The FCT will have its own separate dipole magnet. The electromagnetic calorimeter (ECAL) was proposed in the LoI to extend the particle identification range and a more in-detail discussion on that topic can be found in the SD [32].

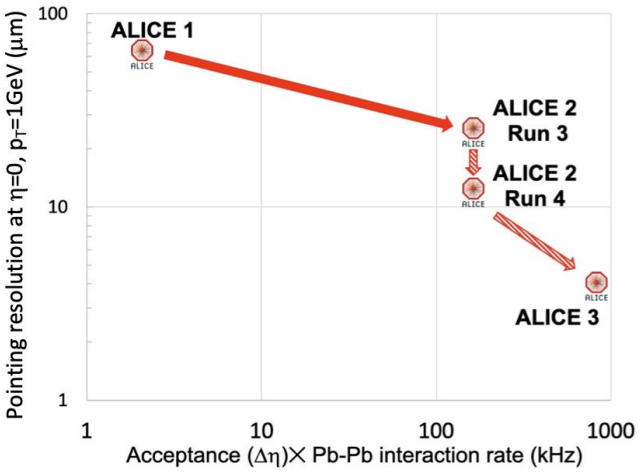

Figure 10: ALICE 3 Pb-Pb performance. The values for this graph were extracted from the LoI [8].

Fig. 10 summarizes the performance gain of ALICE 3 in Pb-Pb collisions compared to its previous installments. It shows a significant jump in both the pointing resolution and acceptance multiplied by the Pb-Pb interaction rate.

4.1 Physics program and detailed layout of ALICE 3

It is of course wonderful to read about its novelties, but the design considerations of ALICE 3 have been motivated by the exhilarating physics program it will pursue. A list of the major topics is given below.

- Ultra-soft photons and tests of quantum field theories
- High-precision beauty measurements
- $D - \bar{D}$ azimuthal correlations
- Multi-charm hadrons, p-wave quarkonia and exotic hadrons
- Azimuthal asymmetry of electromagnetic radiation
- Fluctuation of conserved charges
- Nuclear bound states and hadronic interactions
- Chiral symmetry restoration
- Collectivity in small systems
- High-statistics hadronic physics
- Searches beyond the Standard Model

These physics goals rely on observables which, in their turn, define the requirements of the detector design. The highlight of this program in this thesis is of course the ultra-soft-photon spectrum, the measurement of which will be facilitated by the Forward Conversion Tracker (FCT). The FCT and how it functions within ALICE 3 has its own dedicated section, Section 5. The following paragraphs will give an overview of a small selection of the major components of the physics program of ALICE 3, and at the same time motivate the ALICE 3 detector design and its requirements. A more detailed view on this is available in the LoI [8] and SD [32].

4.1.1 Multi-charm baryons, p-wave quarkonia and exotic hadrons

ALICE 3 has the goal to establish the connection between the thermalization of charm quarks in the quark-gluon plasma (QGP) and the formation of hadrons from deconfined quarks. In central Pb-Pb collisions, many hard scatterings occur which leads to the creation of many $c\bar{c}$ pairs. Some of these c quarks are subsequently separated from their original partner during thermalization of the QGP. When hadronization of the QGP occurs, these deconfined quarks can then form a hadron with another c quark from another hard scattering process. This would lead to the creation of multi-charm baryons like Ω_{cc}, Ξ_{cc}, or even Ω_{ccc}, and p-wave quarkonia ($\chi_{c1,2}$). In addition, ALICE 3 wants investigate the dependence of the production of these multi-heavy-flavor hadrons on the heavy-quark density that varies with rapidity. To perform these measurements, a method called "strangeness tracking" is implemented. In this method, the decay products of these baryons, such as Ξ^- and Ω^- hyperons, are tracked before they decay further. The subsequent decay products of these baryons are then identified with the particle identification capabilities of ALICE 3 and together with the tracking information the multi-charm hadrons are reconstructed. The pixel sensors of the outer tracker, consisting of the barrel layers and forward discs, will have a pixel pitch of $\sim 50\,\mu$m with a corresponding spatial resolution of $\sigma_{\mathrm{POS}} \approx 10\,\mu$m, which allow for accurate tracking of the decay products of the multi-charm baryons. The pixel sensors of the inner tracker achieve a spatial resolution of $2.5\,\mu$m and a distance of the first layer to the primary vertex of 5 mm, which allows for precise primary vertex reconstruction.

4.1.2 Chiral symmetry restoration

Chiral symmetry is one of the properties of the QCD Lagrangian in the massless limit, but it is broken indicated by the mass spectrum of hadrons. Predictions about the impact of chiral symmetry restoration can be made. At high enough temperatures and pressure, like in the QGP, chiral symmetry is expected to be restored. In the QCD vacuum, the mass spectrum of chiral partners is modified, like for the $\rho(770)$ and the $a1(1260)$. The $\rho(770)$ and $a1(1260)$ mass spectral functions change with the temperature of the QGP up to the point when chiral symmetry is restored, at which point the mixing of $\rho(770)$ and $a1(1260)$ degenerates occurs. Through the measurement of the $\rho(770)$ decaying in $\mathrm{e^+e^-}$ pairs, indirect access is provided to the properties of the $a1(1260)$ due to the chiral mixing mechanism. In practical terms this means that an increase in the thermal spectrum of $\mathrm{e^+e^-}$ pairs is expected in the range between the $\rho(770)$ and $\phi(1019)$. This increase would be in the order of 15%[34], [8]. This measurement requires a strong electron identification which can be provided by the TOF and RICH, and in addition electrons need to be tracked with high efficiency, which is done with the IRIS and outer tracker.

4.1.3 $D - \overline{D}$ azimuthal correlations

To discriminate between the different regimes of energy loss in the QGP and reveal possible charm isotropization, ALICE 3 will measure low p_{T} angular $D^0 - \overline{D^0}$ correlations over a wide rapidity range. In the transverse plane, $c\bar{c}$ pairs produced from hard scatterings in nucleon-nucleon collisions are back-to-back. If the medium is fully thermalized, meaning the back-to-back correlation between the produced pairs is gone, then the expected azimuthal distribution between $D^0 - \bar{D}^0$ pairs shows no preference and remains constant. These pairs lose their back-to-back correlation via interactions with the medium. This is then a measurement of the energy loss in the QGP. To measure forwardly produced pairs, the pseudorapidity coverage that is needed is large. In comparison, when this measurement is carried out with the current ALICE setup, the combinatorial background completely overshadows the potential signal. For ALICE 3, with its increased reconstruction performance and particle identification, the measurement of $D^0 - \overline{D^0}$ azimuthal dependence will have high enough precision after the combinatorial background is subtracted.

4.1.4 Ultra-soft photons and tests of quantum field theories

As laid out in the previous chapters, the origin of the excess in the soft-photon regime is still unknown. A candidate for the origin of this excess is the understanding of Low's theorem and the predictions

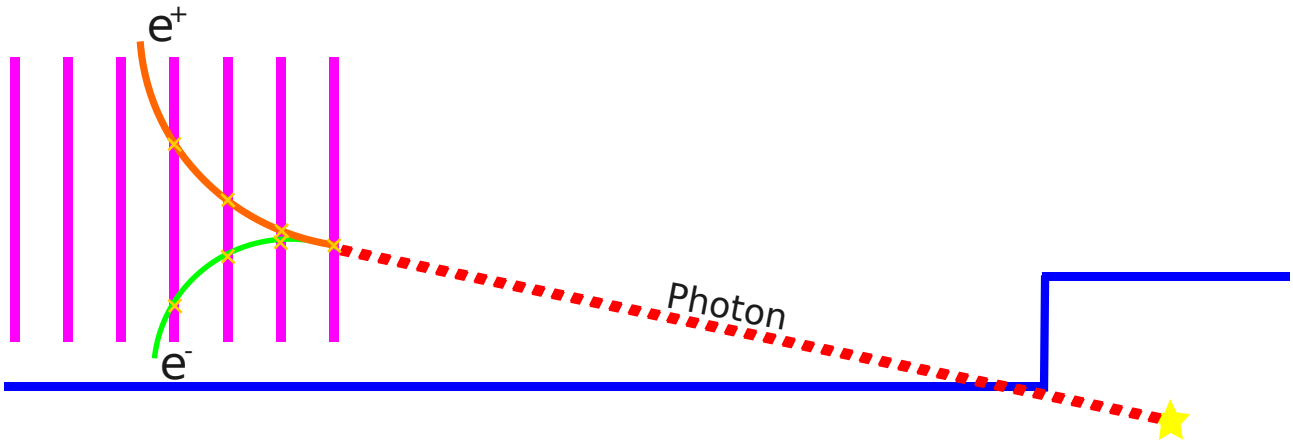

Figure 11: A schematic overview of a pair-producing photon incident on a telescope setup similar to the Forward Conversion Tracker of ALICE 3. The blue line represents the beam pipe, and the magenta lines the disks of the telescope setup. The photon (red dashed line) converts into a electron (green)/positron(orange) pair. The hits are indicated with yellow crosses on the intersection of the trajectories of the e^+e^- pair on the telescope disks. A fit is then performed on the trajectories of these particle to extract the momentum and this is then grouped in a V^0. The properties of the V^0 are then used to reconstruct the incident photon. Technically, in the presence of a dipole magnetic field the electrons only bend this way (i.e. toward and away from the beam pipe) in the xz plane. This figure merely serves illustrational purposes of the concept.

that can be made with it. The goal of the FCT is not only to measure the soft-photon spectrum excess, but extract its quantifying features, i.e. whether it follows a $1/k_{\mathrm{T}}$ relation. In ALICE 3, the soft-photon spectrum is measured in the forward direction with the FCT in the pseudorapidity range $4 < \eta < 5$. The electron-positron pairs that are created due to the conversion of incident photons are tracked using the consecutive layers of the FCT. Grouping these tracks together into a so-called "V^0", its properties are then used to reconstruct the photon that created it. Fig. 11 shows a schematic view of the reconstruction of an incident pair-producing photon on a telescope setup including a magnetic field similar to the FCT. In the LoI [8], previous studies of the photon reconstruction efficiency of the FCT showed that a pointing angle resolution of 0.025 mrad and a transverse momentum resolution of 15 % can be achieved. Since soft-photon production is not limited to accelerating initial- and final-state particles, background reduction is an important step in this measurement to unveil the specific properties of the potential excess. A large amount of background is attributed to the formation of external bremsstrahlung in detector material in front of the FCT. To this end, the material budget in front of the FCT is kept to a minimum by placing as little other detectors and support material in front of the FCT as possible. In section 5, the simulation of the FCT is discussed. In section 6 the performance of the FCT is discussed which includes different strategies to reduce the background. A setup with a conical beam pipe to reduce the effective material budget is explored in Sec. 6.3.

4.2 Reconstruction with ALICE 3

The interaction rate at which ALICE 3 will operate equates to 24 MHz, as outlined in the LoI [8]. Since the bunches travel at the speed of light, the number of orbits per second is $c/27\,\mathrm{km} \approx 11000/\mathrm{s}$. At an interaction rate of 24 MHz, this means that there will be $24\,\mathrm{MHz}/11\,\mathrm{kHz} \approx 2180$ collisions per orbit. By construction, 3564 bunch crossing happen per LHC orbit, this would mean that the average in-bunch pile-up equates $\mu \approx 2180/3564 \approx 0.61$. However, the number quoted in the LoI for $\mu \approx 1.2$. This is due the fact that the LHC never operates with all bunches populated with protons, so even if a bunch crossing would occur of a "bunch" that is not populated, or rather a "gap", no collisions would occur. The filling scheme of the LHC defines the amount of bunches per beam. In the LHC, there are two beams that run in opposite direction which collide at interaction points, IP2 for ALICE. The more realistic scenario is that of a representative fill of Run 3 which had $\sim$ 1840 proton-proton collisions per orbit of the LHC. To achieve the desired interaction rate, the in-bunch

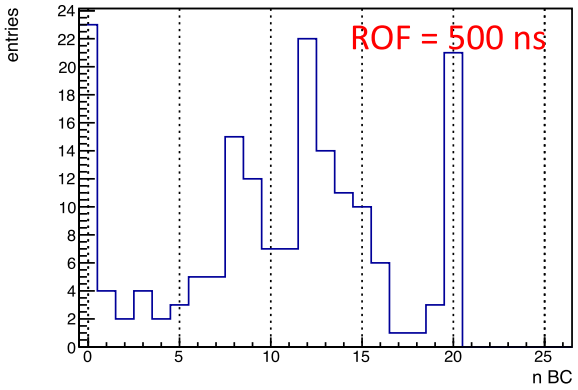

(a) Frequency of occurrence of number of collisions per ROF for a single orbit of the LHC.

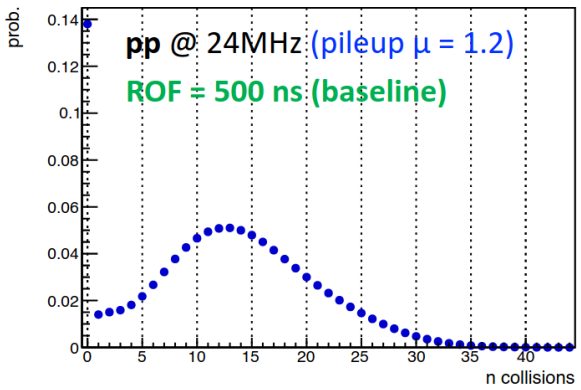

(b) Probability for number of collisions per ROF.

Figure 12: Figures taken from Ref. [35].

pile-up would then be $\mu \approx 2180/1840 \approx 1.18$, which is much closer to the quoted 1.2 in the LoI. To then actually acquire data on these collisions, one LHC orbit needs to be sliced into readout frames (ROFs). Each bunch is separated from the next by 25 ns in time. Assuming a 500 ns ROF, the baseline for ALICE 3 [32], this means there are $500/25 = 20$ bunch crossings per ROF. In one beam, populated bunches are packed closely together in a so-called train, of which there are multiple per injection. In-between trains there is a gap of unpopulated bunches which causes a significant portion of the ROFs to record zero collisions. For a particular fill of Run 3 the frequency of the number of collisions per ROF was recorded, see Fig. 12a. Based on this a short sampling simulation was performed. To get the probability for n collisions to happen in a single ROF, ROFs with n collisions based on the frequency of occurrence in the fill were simulated. Sampling each collision by a Poisson distribution with $\mu \approx 1.18$, the probability for n collisions to happen in a single ROF is given in Fig. 12, Ref. [35]. In this figure, the probability to have 0 collisions in one ROF is a lot higher than having n collisions where $n \neq 0$. This is due to the fact that ROFs are tied to the orbit of the LHC, which means that some ROFs can fall in "gaps" between trains due to the filling scheme. The global reconstruction which makes use of the information of the primary vertex location, provided by the tracker, and the time of flight of the particles, provided by the TOF, then disentangles the information in one ROF to enable analysis on an event-by-event basis.

4.3 Integrated luminosity requirement for the FCT

Initial studies showed a pointing angle resolution of 0.025 rad for photons with the FCT is possible [8]. Charged particles, however, due to their interactions with the material and the bending of their tracks in the magnetic field, are more tricky to trace back to their respective primary vertex if the amount of events in one readout frame exceeds 1. The presence of more than 1 event in a ROF complicates the applicability of certain cuts to reduce the background which will be made more concrete in the rest of the thesis. Crudely said, without a detector to provides timestamps for charged particles like the TOF and RICH, additional events in the same ROF effectively function as pileup. For ALICE 3, as given in Fig. 12, the probability for n events occurring in a single ROF is highest at $n = 13$, but not zero at $n = 1$. The probability of a single event in a given ROF $P \approx 0.015$, or 1.5% of all the readout frames.

In order to calculate how many collisions need to be recorded to achieve similar statistics as will be presented in this thesis, 10M, the following equation needs to be solved

$$N_{\text{Events}} = \frac{1}{\text{R}_{\phi\text{ cov.}}} \times \frac{1}{\text{P}_{\text{Phot. conv.}}} \times \frac{1}{\text{P}_{\text{Meas. V}_0}} \times N_{\text{Events for acc. stat.}}, \tag{42}$$

where N_{Events} is the number of events required that are available for single event-by-event analysis, $\text{R}_{\phi\text{ cov.}}$ the ratio of the azimuthal coverage, $\text{P}_{\text{Phot. conv.}}$ the probability of a photon to convert in the

FCT, $P_{\text{Meas. } V_0}$ the probability that an e^+e^- pair of a converted photon can be reconstructed with the FCT and $N_{\text{Events for acc. stat.}}$ the number of events required for acceptable statistics. This is often expressed as the integrated luminosity, L_{int}, given by

$$N_{\text{Events}} = \sigma_{\text{Events}}^{\text{pp, non-dif}} \times L_{\text{int}}, \tag{43}$$

where $\sigma_{\text{Events}}^{\text{pp, non-dif}}$ is the cross section for recorded non-diffractive proton-proton collisions. ALICE 3 plans to record $L_{\text{int. A3}} = 3\,\text{fb}^{-1}$ of pp collisions per operational year under the assumption that every ROF independent of the number of collisions that occur inside of it can be reconstructed. Fig. 12 shows the probability of n collisions occurring in a single ROF. The contribution to the total amount of integrated luminosity per operational year for ROFs with n collisions is given in Fig. 13. For the

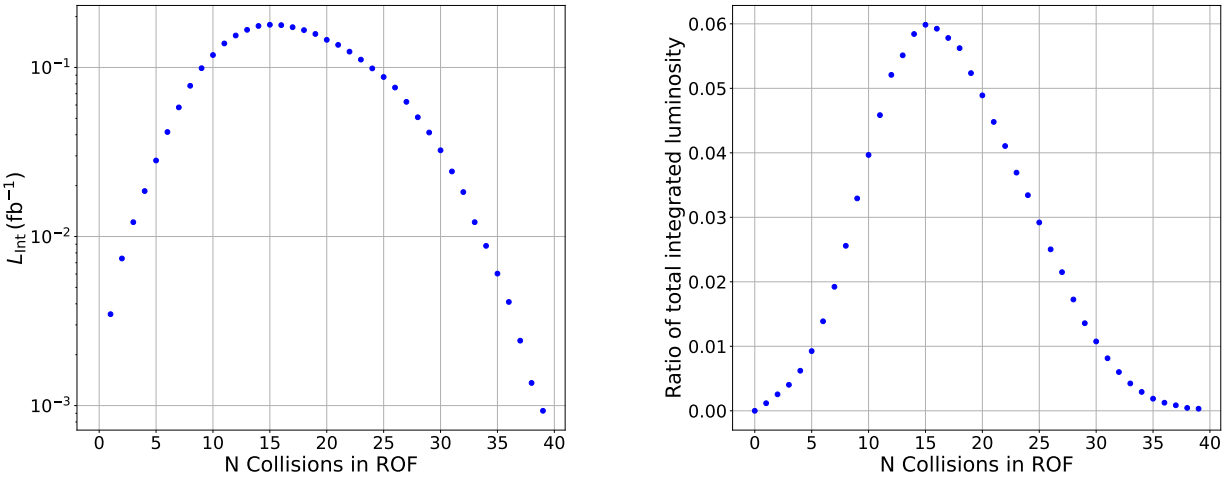

(a) Contribution

(b) Ratio

Figure 13: The contribution to the total amount of integrated luminosity per operational year of ALICE 3 for ROFs with n collisions (left). The ratio of the aforementioned contribution (right).

calculation of the number of diffractive collisions that need to occur, N_{events}, the values will be given in this thesis. $R_{\phi\text{ cov.}}$ is 1 for circular disks, but less for square layers, see 9. For simplicity, this is assumed to be 1/2, but in actuality this will be slightly lower. The probability for a photon to convert in the first two layers of the FCT is given by $7/9\,x/X_0$, so this is ~ 0.016 since the first two layers have 2% of a radiation length as material budget. The probability to measure an e^+e^- pair of a converted photon that can be reconstructed with the FCT depends on the geometry of the FCT, the energy of the converted photon and the strength of the dipole magnetic field. It is assumed that 10% of the converted photons can be reconstructed for this calculation. In this thesis, for the "Default ALICE 3" simulation set, see 5, 10M events were simulated, so to achieve similar statistics as presented in this thesis, $N_{\text{Events for acc. stat.}} = 10\text{M}$. Plugging this all in gives $N_{\text{Events}} \approx 1.25 \times 10^{10}$ events. For a center-of-mass energy of $\sqrt{s} = 13\,\text{TeV}$, CMS reported [36] a cross section for inelastic pp interactions, $\sigma_{\text{inel}}^{\text{pp}} = 71.26 \pm 0.06\text{ (stat.)} \pm 0.47\text{ (sys.)} \pm 2.09\text{ (lum.)} \pm 2.72\text{ (ext.)}$ mb, comparable to what ATLAS reported [37]. The fraction of non-diffractive events of the proton-proton collisions at LHC energies is roughly 75–80% and for $\sqrt{s} = 14\,\text{TeV}$, PYTHIA [9] reports this as $\sigma_{\text{Events}}^{\text{pp, non-dif}} = 57.17\,\text{mb}$ which was also used in the simulations of this thesis. This then gives a corresponding integrated luminosity of $L_{\text{int}} \approx 220\,\text{nb}^{-1}$. The integrated luminosity recorded $L_{\text{int. n=1}} \approx 3.5\,\text{pb}^{-1}$ when only the ROFs with $n = 1$ are considered, as shown in Fig. 13a. Since this measurement does not require any special beam time, it is expected that this can be achieved during Run 5. However, to increase the statistics for this measurement, a dedicated low-luminosity run could be requested. This would also greatly simplify the analysis process since it eliminates the requirement to check all recorded ROFs of all fills for those that only contain 1 collision. No research has gone into the feasibility of performing a measurement where there are two collisions present in a single ROF, but if it is, this would reduce the operation

time by a factor 2 or more. The single event-by-event analysis is a requirement when a ePID detector is included in the setup or when the distance to the closest charged particle is required as a cut on the background, but this restriction can be loosened when these things are not required.

5 Simulation of the measurement of the soft-photon spectrum with the FCT

The Forward Conversion Tracker of ALICE 3 measures the soft-photon spectrum via the tracking of e^+e^- conversion pairs in a dipole magnetic field with a strength of $\hat{B}_y = 0.25\,T$. These pairs are tracked by 11 circular disks positioned around the beam pipe equipped with MAPS. The inner radius, outer radius, z-position and thickness of the individual disks is given in Tab. 5. The radii of the disks cover the pseudorapidity region of $4 < \eta < 5$.

Disk	Inner Radius (cm)	Outer radius (cm)	Position z (cm)	Material thickness $\%X_0$
0	5	17	442	1.0
1	5	17	444	1.0
2	5	17	446	1.0
3	5	17	448	1.0
4	5	17	450	1.0
5	5	17	452	1.0
6	5	17	460	1.0
7	5	18	470	1.0
8	5	18	480	1.0
9	5	19	490	1.0
10	5	19	500	1.0

Table 5: The inner radius, outer radius, z-position and thickness of the disks of the Forward Conversion Tracker in ALICE 3.

The spacing of the first 6 layers of the FCT is close together so even low-energetic e^+e^- pairs, which equates to small bending radii, can be tracked. For more energetic pairs, the later layers are more spaced out. Since the vast majority of the contribution to the momentum of incoming photons in this pseudorapidity region comes from p_z, a dipole magnet with a magnetic field in the $\hat{y}$ direction was chosen. Charged particles in a magnetic field in the $\hat{y}$ direction bend in the xz-plane, giving the FCT the opportunity to track very forward photons. A tracked e^+e^- pair together forms a so-called V^0 where its name comes from the resemblance of the shape of the tracks of the pair with the letter "V" and the 0 comes from the fact that it finds its origin through a neutral particle which do not leave tracks, e.g. through the decay of a neutral particle or the conversion of a photon. Through the properties of the tracks and the V^0, the photon is reconstructed.

Earlier studies on the tracking and reconstruction efficiency of the FCT, presented in the LoI [8], showed that a pointing angle resolution of 0.025 mrad and a transverse momentum resolution of 15 % can be achieved. These numbers are taken as estimates of the results presented there and are used for the results in this thesis.

5.1 Simulation strategy

The simulations in this thesis were performed with the ALICE O^2 software [27], which stands for online-offline computing system. It contains the code for the reconstruction, calibration and simulation for the ALICE experiment used for Run 3 and 4. In addition, it is under development for Run 5 and 6, for which it contains the current ALICE 3 detector design based on the upcoming Scoping Document [32]. O^2 performs its simulations in multiple steps, a schematic overview of which is given in Fig. 14. First, the event generator, e.g. PYTHIA [9] or FLUKA [38, 39], generates an event. The so-called particle stack that contains the generated particles then gets passed to the propagator, e.g. GEANT3 or GEANT4 [40–42]. The propagator propagates the particles through the detector setup and calculates which material interactions take place. In addition, it also takes care of the magnetic

field present in the setup. The particles then leave so-called hits in user-defined sensitive volumes which generally contain the particle type, momentum of the particle that passed through, position on the sensitive volume and energy deposited by the particle in the particular volume. Based on these hits the digitization step occurs which simulates the actual detector response. The digitizer is usually a custom piece of code and highly detector specific, whereas the generator and propagator can more or less be tweaked by configuration parameters. The output of the digitizer is then used for track & vertex reconstruction and particle identification after which events can be analyzed. The analysis is performed with O2Physics [27]. It is being studied to have parts of this workflow be performed by A Common Tracking Software Project (ACTS) [43], predominantly the vertex and track reconstruction. The usage of ACTS for the FCT is discussed in more detail in Section 5.6. Specific details of the simulation settings used for this thesis can be found in Sec. 5.2.

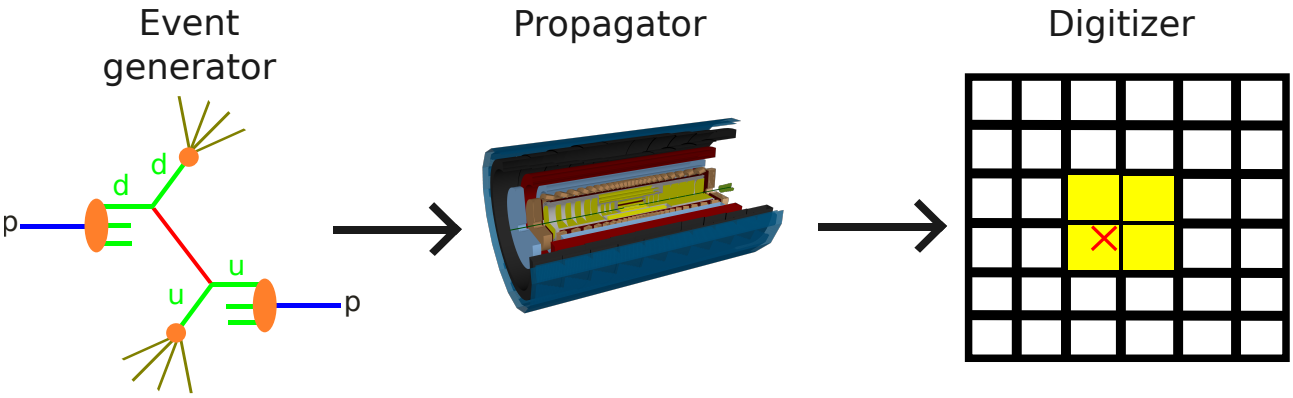

Figure 14: A schematic overview of a simulation workflow of high energy particle collisions with a detector setup to read out the data. The events are generated by the event generator, then propagated through the detector setup with the propagator which simulates material interactions and finally the detector response is done by the digitizer. An example of a digitization process is represented in this figure by an incident charged particle on a grid of MAPS (red cross). The propagator calculates the energy deposited in the material and the digitizer translates this in a cluster of pixels that registered a binary readout through the simulation of charge sharing.

For the simulation of the soft-photon spectrum the Low Photon Generator (LPG), as described in Sec. 2.3, is included in the O^2 workflow. The LPG acts after the Generator has generated the particle collision and then calculates the soft-photon spectrum and adds the photons to the particle stack which then gets handed to the propagator.

5.1.1 Experimental setup

For this thesis, the simulations were predominantly carried out by O^2. Although O^2 contains all the subdetectors of ALICE 3 as given in Fig. 8, only a subset of these modules was activated for these simulations. The motivation for the exclusion of the solenoid magnet, ECAL, absorber and muon chambers is to speed up the simulation process. These modules are at such a big radius that they have no influence on the soft-photon spectrum that reaches the FCT. The Forward Calorimeter (FOCAL), the dipole for the FCT and FCT Ring Imaging Cherenkov detector (FCT RICH) that are present in the figure, were also not present in the simulation. The dipole magnet and FOCAL are at positions, e.g. behind the FCT, where they do not influence the soft-photon spectrum. The inclusion of a RICH detector behind the FCT, the FCT RICH, which was done with a separate simulation, is discussed in Sec. 6.5. Even though both magnets were absent in the simulation, it is only their material that was missing. The magnetic field during the propagation step was still present which can be set through O^2. Later, it will be discussed that the dominant source of background comes from external bremsstrahlung made in material in front of the FCT. To better illustrate the modules that contribute to the material budget, a zoom-in of the setup is given in Fig. 15.
All the modules in O^2 at the date of writing are represented by a more-or-less simplified geometric version of their final design, but the material budget, which is the important factor for accurate

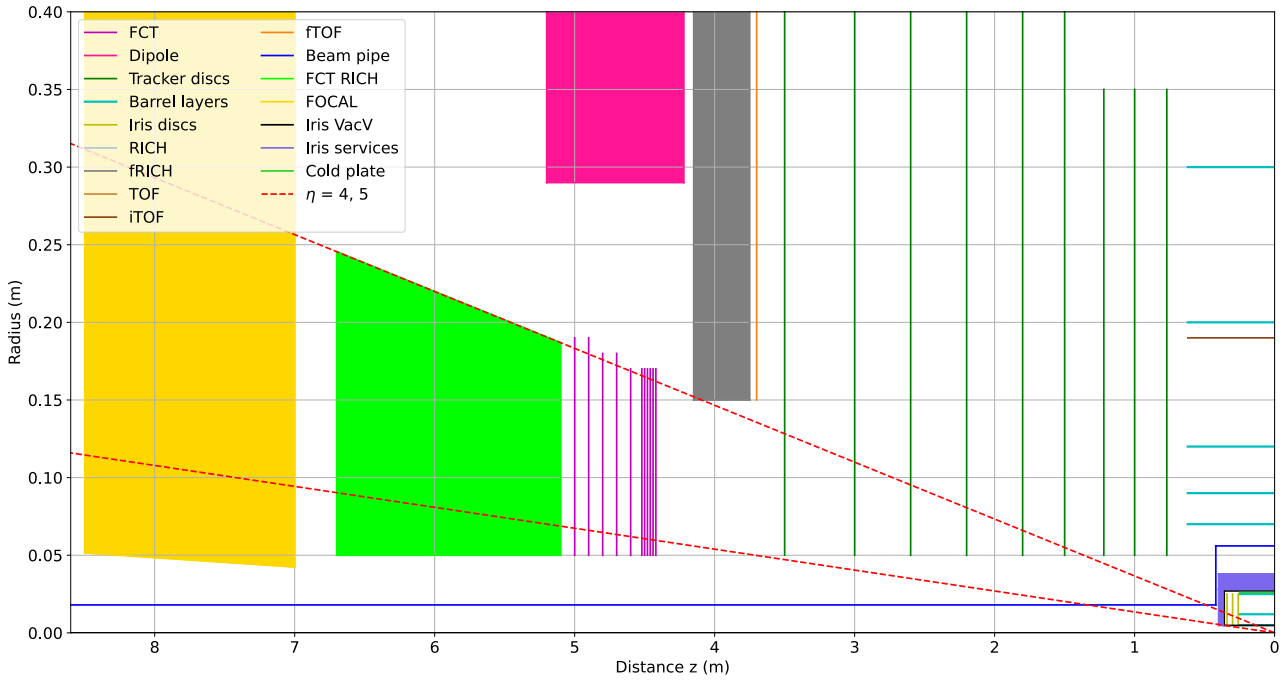

Figure 15: Schematic radial projection of ALICE 3 zoomed in to show just that which contributes to the material budget in front of the FCT.

propagation of the particles through the setup, is given accurately. The geometric parameters of most of these modules present in this figure are given in Tab. 6, 7, 8, 9.
The beam pipe is split in three sections: the A-side, the primary vacuum vessel and the C-side. At all points, the thickness of the beam pipe is 0.8 mm and it is entirely machined out of beryllium. The primary vacuum vessel, with a half length of 38 cm centered at the origin ($z = 0$), has an inner radius of 5.6 cm and houses the IRIS vacuum vessel, which in turn contains the IRIS tracker. The beam pipe sections at the A and C sides connect to the primary vacuum vessel on either side and have an inner radius of 1.8 cm and 5.6 cm, respectively. The inner radius of the C side beam pipe section is larger to house the majority of the services needed for the IRIS tracker (e.g. cables for data and power, the rotational mechanism, support structures, etc.). Since the IRIS tracker is retractable it sports a modular design divided in four equally sized modules which are allowed to rotate/move in order to settle in their closed position around the interaction point. To provide structural integrity to these modules needed for rotation and to prevent the contamination of the beam pipe vacuum through the outgassing of the detector parts, these modules are placed in a secondary vacuum provided by the so-called petal cases. These petal cases, together with their three petal barrel layer sections, six petal disk sections and the cold plate section are displayed in Fig. 16 which showcases the in- and outside of the petal cases.
The left figure, Fig. 16a, shows the IRIS tracker in its contracted or closed state. For each of the four petal cases, different modules have been deactivated in the viewer allowing for a look inside. For the top left petal case all modules are active, but only the petal case itself, which provides the secondary vacuum for the instruments inside, is visible. Going in the clockwise direction, the petal case for the next quadrant has been deactivated in the viewer and the front three petal case disk sections and cold plate are visible. For the next quadrant, the petal disk sections have been deactivated so the petal barrel layer sections along with the cold plate are visible. In the last quadrant only the cold plate is visible. The figure on the right shows the IRIS tracker in the open state, and again, some modules have been deactivated in the viewer allowing for a look inside. Fig. 17 shows the radial projection of the IRIS tracker in its contracted or closed state, whereas Fig. 18 shows the radial projection of the IRIS tracker in its retracted or open state.

Layer	Inner Radius (cm)		Outer radius (cm)	Position $\|z\|$ (cm)	Material thickness ($\%X_0$)
	A Side	C Side			
0	0.5	0.5	2.5	26	0.1
1	0.5	0.5	2.5	30	0.1
2	0.5	0.5	2.5	34	0.1
3	5.0	7.0	35	77	1.0
4	5.0	7.0	35	100	1.0
5	5.0	7.0	35	122	1.0
6	5.0	7.0	68	150	1.0
7	5.0	7.0	68	180	1.0
8	5.0	7.0	68	220	1.0
9	5.0	7.0	68	260	1.0
10	5.0	7.0	68	300	1.0
11	5.0	7.0	68	350	1.0

Table 6: Geometric specifications of the outer tracker disks.

Layer	Length Δz (cm)	Radius (r) (cm)	Material thickness ($\%X_0$)
0	50	0.5	0.1
1	50	1.2	0.1
2	50	2.5	0.1
3	124	7	1.0
4	124	9	1.0
5	124	12	1.0
6	124	20	1.0
7	124	30	1.0
8	258	45	1.0
9	258	60	1.0
10	258	80	1.0

Table 7: Geometric specifications of the barrel tracker layers.

	Inner TOF	Outer TOF	Forward TOF disks
Radius (m)	0.19	0.85	0.15 to 1.0
z range (m)	-0.62 to 0.62	-3.5 to 3.5	± 3.70
Acceptance	$\|\eta\| < 1.9$	$\|\eta\| < 2$	$2 < \|\eta\| < 4$
Material thickness ($\%X_0$)	1 to 3	1 to 3	1 to 3

Table 8: Geometric specifications of the TOF, iTOF and fTOF.

	Barrel RICH	Forward RICH disks
Radius (m)	0.9 to 1.2	0.15 to 1.15
z range (m)	-3.5 to 3.5	$3.75 < \|z\| < 4.15$
Acceptance	$\|\eta\| < 2$	$2 < \|\eta\| < 4$
Material thickness ($\%X_0$)		

Table 9: Geometric specifications of the RICH and fRICH.

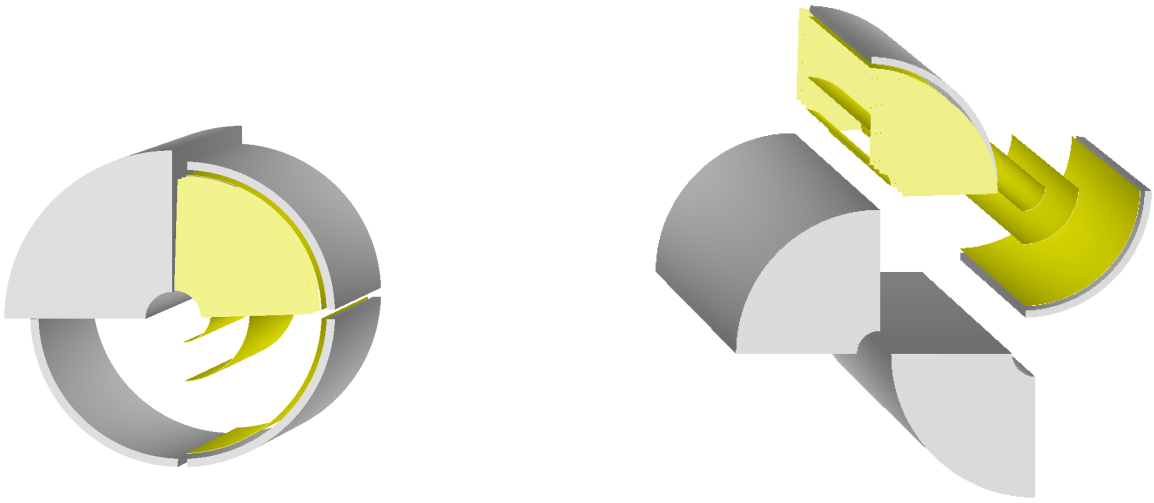

(a) (b)

Figure 16: The geometric representation of the IRIS tracker in O^2. In the viewer, different modules of the petal cases have been activated to showcase all its parts.

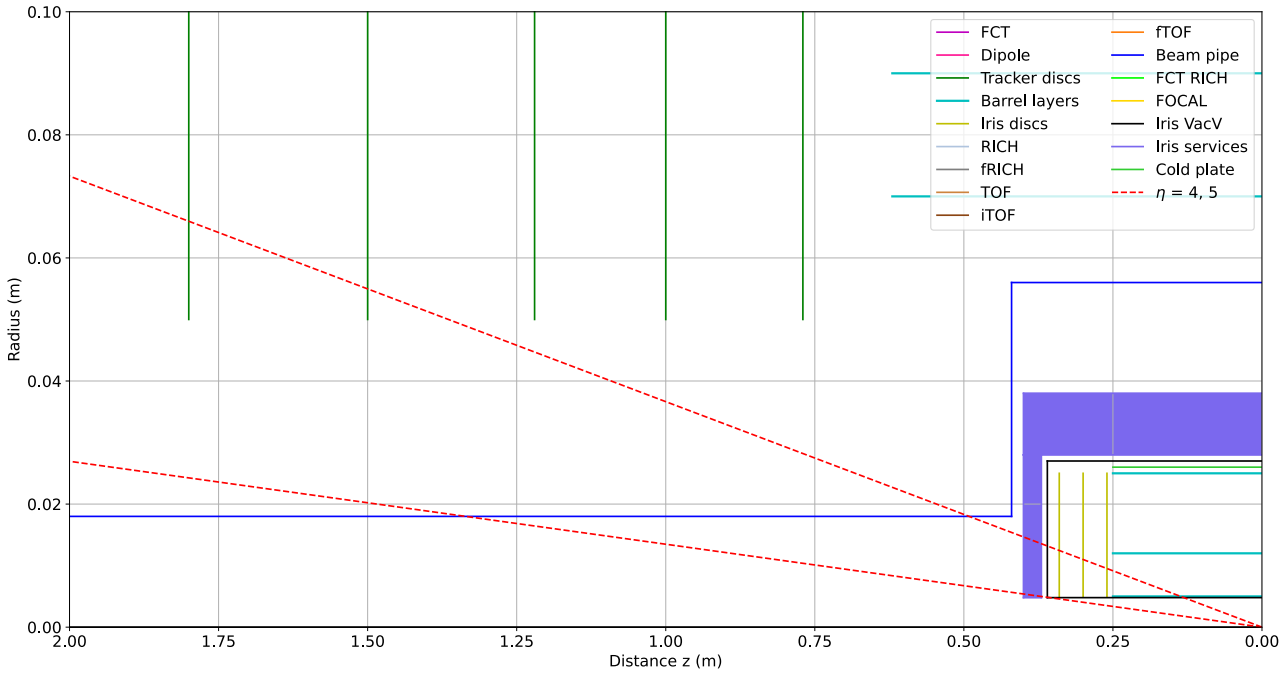

Figure 17: Radial projection of the IRIS in the contracted/closed position.

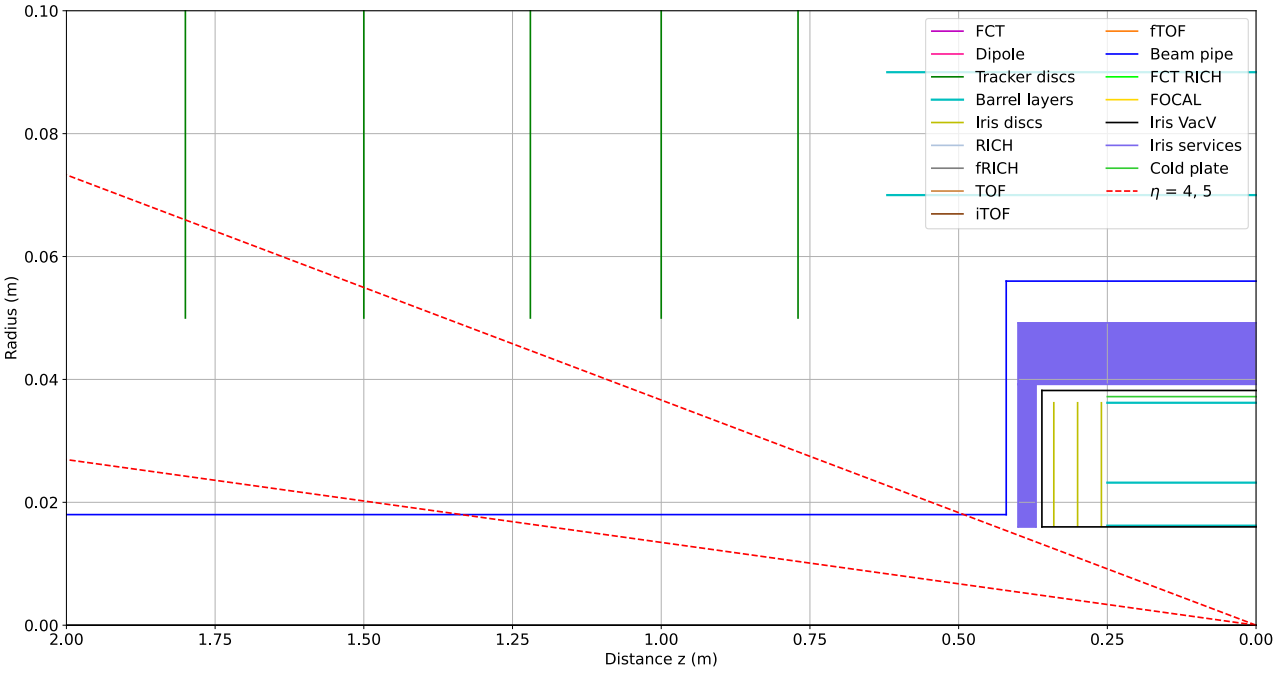

Figure 18: Radial projection of the IRIS in the retracted/open position.

5.2 Simulation settings and generation of datasets

For this thesis, five simulations with different layouts of ALICE 3 were carried out with O^2. For these simulations, the following parameters were used:

Listing 1: Command line prompt to run the simualtions with O^2.

```
export ALICE3_SIM_FIELD=ON
export ALICE3_MAGFIELD_MACRO=$magFieldPath

o2-sim --detectorList ALICE3 -m "FCT TRK FT3 A3IP TF3 RCH"
-j ${NWORKERS} -n ${SIGEVENTS} -g external --configKeyValues
"GeneratorExternal.fileName=$LPGMacroPath;
GeneratorExternal.funcName=GeneratorLow();
FCTBase.configFile=$fctConfig" --configFile $o2simConfig
```

Since O^2 can perform simulations for both ALICE 2 and 2.1, as well as ALICE 3, the "–detectorList" flag allows the user to select which detector lists to select their modules from[8]. The specifier "-m" allows the user to select which modules to activate. In O^2, modules sometimes have different names than what is used in the LoI or SD. The "TRK" contains the barrel layers as well the IRIS tracker. The "FT3" contains the outer tracker disks. "A3IP" takes care of the beam pipe and the TOFs and RICH's are activated by "TF3" and "RCH", respectively. "-g" selects the generator and setting this to "external" allows for the activation of an external generator. Then the LPG is selected as an external generator and, together with PYTHIA, generates the events. The generator can be specified with "-e", but since that flag is not present the default generator, GEANT4, was used. For the FCT, the geometry of the disks can be provided through a .cfg file, and the settings for the generator, i.e. PYTHIA, get passed through the o2simConfig file. An additional flag "TRKBase.irisOpen=true" allows to set the IRIS tracker in its retracted, or open position. The settings for PYTHIA, the LPG, GEANT4 and the magnetic field in O^2 are given in Tab. 10. In O^2 a custom magnetic field is set through the two "export" lines in bash where the range of applicability is specified in an external .C file.

[8] A combination is possible to make a hybrid detector. This is useful to perform simulations with the current magnet activated in addition to the one of ALICE 3 since the current magnet will not be removed from the cavern for the installation of ALICE 3 due to the high costs of the operation.

PYTHIA settings	Value	Low Photon Generator	Value
Version	8.311	η range	$[3, 5.5]$
Beams:idA	2212	Number of η bins	250
Beams:idB	2212	ϕ range	$[0, 2\pi]$
Beams:eCM	14000. # GeV	Number of ϕ bins	250
SoftQCD:nonDiffractive	on	Energy range	$[0.001, 1]$ GeV
ParticleDecays:limitTau0	on	Number of energy bins	1000
ParticleDecays:tau0Max	10.	Photon status	201
Random:setSeed	on		

Magnetic field settings	Value	GEANT4 settings	Value
Region 1		Version	geant4-11-02
Field strength $[\hat{B}_x, \hat{B}_y, \hat{B}_z]$	[0., 2.5, 0.] # kGauss	Hadron physics list	FTFP_BERT_EMV
z range	$[440, 500]$ # cm	EMoption	1
r range	$[0, 50]$ # cm		
Region 2			
Field strength $[\hat{B}_x, \hat{B}_y, \hat{B}_z]$	[0., 0., 20] # kGauss		
Range (r, z)	Outside region 1		

Table 10: Simulation settings for PYTHIA, LPG, GEANT4 and the magnetic field in O^2. The LPG sets the "status" of produced photons to 201, which is a flag used in PYTHIA to signal that these come from user-defined processes. The range of region 2 of the magnetic field is defined such that it applies whenever a particle is outside region 1.

Setting \ Name	**Default ALICE 3**	**IRIS Opened**	**Window 1**	**Window 2**	**Window 3**
Number of events	10^7	$5 \cdot 10^6$	$2.5 \cdot 10^6$	$2.5 \cdot 10^6$	$2.5 \cdot 10^6$
IRIS position	Closed	Open	Closed	Closed	Closed
Window activated	No	No	Yes	Yes	Yes
Window length	-	-	150 cm	200 cm	250 cm

Table 11: Differences in simulation settings for the five simulations carried out for this thesis.

The differences for the five simulations can be viewed in Tab. 11. The code of O^2 was modified such that the sensitive volumes of the FCT also record photons and not only charged particles.
The simulation set "Default ALICE 3" was executed with the setup for ALICE 3 as described in this and previous chapters. The simulation set "IRIS Opened" has the same properties, except that the IRIS tracker is in the opened/retracted position. For the sets "Window x" the beam pipe in O^2 was modified to include a conical section in order to reduce the effective material budget in front of the FCT. This will be explored more in Sec. 6.3.

5.3 Material budget

It is of critical importance to implement the material budget of the ALICE 3 detector properly for the simulations with the FCT since many sources of background find their origin through material interactions. This is especially so for external bremsstrahlung which is the biggest source of background in the low k_T regime and entirely dependent on the material budget in front of the FCT. A big contribution to the background also originates from hadronic interactions with the material. To this end it is important to understand which parts of the ALICE 3 detector contribute the most. The material budget in terms of radiation lengths as function of pseudorapity is presented in Fig. 19.
Zooming in on the layout of ALICE 3 in Fig. 9 to display just that which contributes to the material

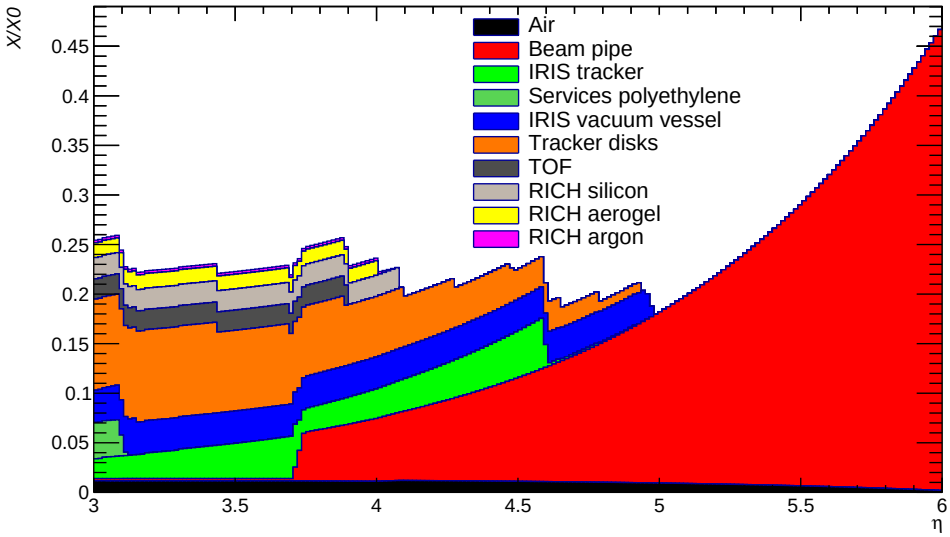

Figure 19: The material budget as function of the pseudorapidity of ALICE 3 as per the "Default ALICE 3" simulation set. The material budget is counted by performing a scan of the geometric setup used for the simulations. The material budget is averaged over the azimuthal range of $[0, 2\pi]$.

budget in front of the FCT is done in Fig. 15. The main contribution to the material budget comes from the beam pipe (red) which increases as the psuedorapidity increases due to the shallower angle under which the particles are incident on the beam pipe. The effective path length, d_e, through the material can be calculated through the geometric relation

$$d_e = d \cosh \eta, \tag{44}$$

where d is the thickness of the beam pipe, 0.8 mm of beryllium, and η is the pseudorapidity representing the incident angle of the particle on the beam pipe. Beryllium has a radiation length of 35.28 cm [44] and at $\eta = 4$ this gives a material budget contribution of $\sim 6.2\%$. Inside the beam pipe there is a vacuum, and as such, the amount of air a particle travels through before reaching the FCT[9] decreases at higher pseudorapidity. It is roughly equal to 1% at $\eta = 4$. At this η, particles pass through 4 sensitive volumes of the IRIS tracker: one barrel layer and three disks, which all have a thickness of 0.1% of a radiation length, but the barrel layer contributes the most through its effective material. The sensitive volumes of the IRIS tracker total a contribution of 2.8%. The petal cases have a wall thickness of 0.15 mm, but since they have radial walls as well, see Fig. 16, the material budget depends on the azimuthal angle of emission of the particle. As such, the contribution of the petal cases is averaged over the azimuthal range from $[0, 2\pi]$ giving a contribution of $\approx 4\%$. The particles traverse the disks of the outer tracker too, which contribute $1\% X/X_0$ each, for a total of 6%. Then there is the final contribution at $\eta = 4$ from aerogel, argon and silicon, which are materials present in the fRICH, totaling to a contribution of $\sim 3\%$. Summing this all up gives the material budget of $X/X_0 \approx 0.23$ at $\eta = 4$.

[9] That is, the z position of the first layer of the FCT

5.4 Classification of the background

To extract a possible excess on top of the predicted soft-photon spectrum in the acceptance of the FCT, the background and its sources need to be understood. In this thesis, the soft-photon production channels are grouped in seven different categories:

- Internal bremsstrahlung
- Hadronic decays and direct γ's
- External bremsstrahlung
- Secondary interactions/decays
- Hadronic inelastic interaction
- Positron annihilation (in flight)
- Other sources

This grouping is based on the production process of the photon and where in the simulation workflow these photons were produced. A schematic overview of the different ways such photons can be produced, together with their grouping, is given in Fig. 20. Each group has their own dedicated paragraph below, except for internal bremsstrahlung which was discussed in chapter 2. The photon spectrum to then arrive at the FCT for the simulation set "Default ALICE 3" is given in Fig. 21.

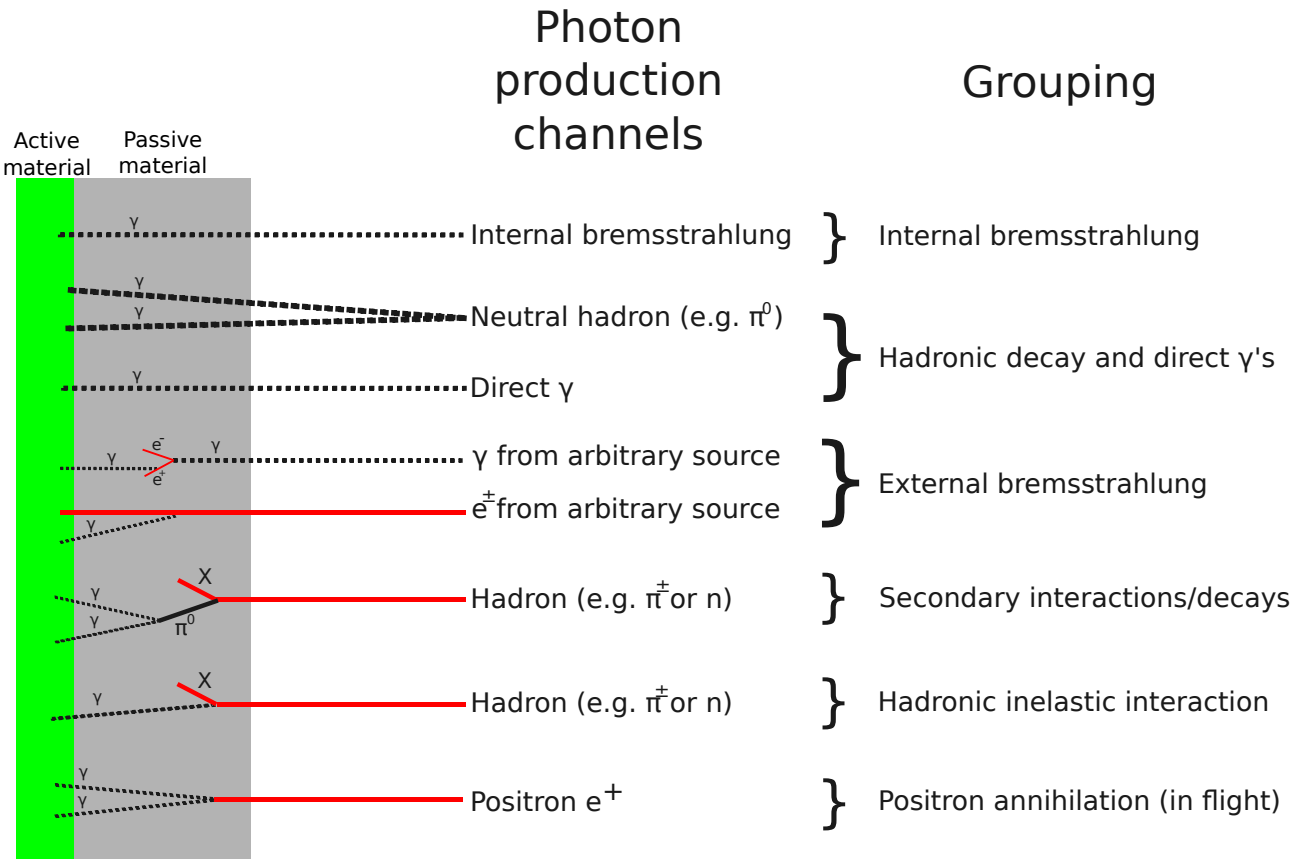

Figure 20: Grouping of the soft-photon sources based on their production channels.

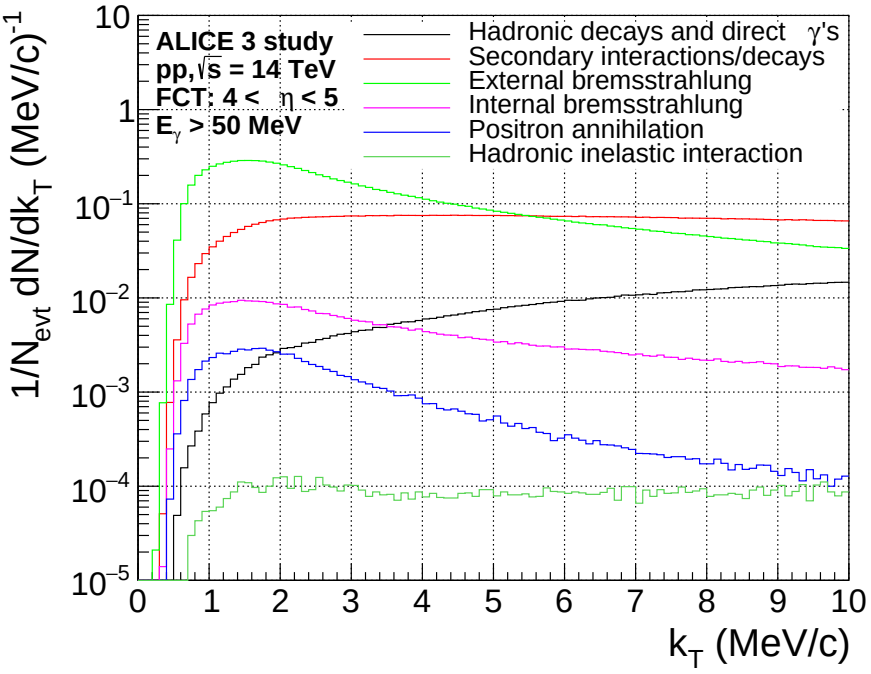

Figure 21: The photon spectrum to arrive at the FCT of ALICE 3. No cuts were applied to reduce the background. The different colors of the histograms indicate the different sources of background and signal.

The corresponding fraction per channel of the total spectrum is given in Fig. 22. In the lower k_{T} region

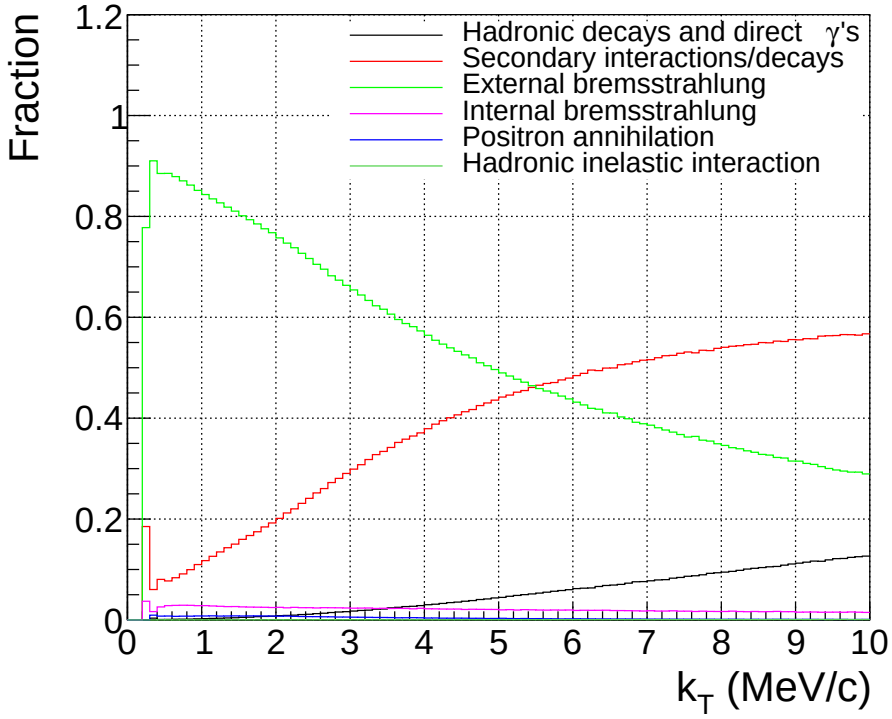

Figure 22: The fractions per photon channel of the total spectrum.

of the histogram, the contribution of external bremsstrahlung to the spectrum is largest, but this is overtaken by secondary interactions/decays at $k_{\mathrm{T}} \approx 5.4\,\mathrm{MeV}/c$ showing the importance of a good strategy to suppress the influence of both on the measurement. Earlier studies of the measurement of the soft-photon spectrum with the FCT in ALICE 3 hinted at similar issues, Ref. [45].

5.4.1 Hadronic decays and direct γ's

Through hadronization in a non-diffractive proton-proton collision, neutral hadrons like π^0's and η's are produced which then decay into photons, or any other production channel that contains a photon. Neutral hadrons by far dominate the contribution to this spectrum, but a decay from a charged hadron where the end product includes a photon is not impossible. Direct photons are produced through initial parton scattering, e.g. $q + g \to q + \gamma$ or $q + \bar{q} \to \gamma + g$. Their contribution is negligible, but they are included for completeness. Both channels are handled by PYTHIA.

5.4.2 External bremsstrahlung

External bremsstrahlung is formed when a charged particle passes through material and radiates a photon. In practice, however, electrons are the dominant source that emit photons produced via external bremsstrahlung. These electrons can have various origins, but most are produced through conversions of photons[10] to e^+e^- in material in front of the FCT. In Fig. 20 two production channels are grouped together in "External bremsstrahlung", but they are actually the same. This is to highlight that, even though spuriously produced electrons exist, most of the electrons[11] are created through photon conversion.

Before particles produced in a proton-proton collision get the chance to interact with any material in the detector setup, the dominant source of photon production is the decay of $\pi^0 \to \gamma\gamma$. These photons interact with material were e^+e^- pairs are produced and these electrons then radiate a photon. With the method described in Ref. [19], the aforementioned photon spectrum can be calculated. To understand how they came up with their method, the starting point is Eq. (34.30) from the Review of Particle Physics by the Particle Data Group [44]. The number of photons produced by an electron traveling a distance $x \ll X_0$ in the infrared limit (small $y = \omega_k/E$) is given by

$$\frac{dN_\gamma}{d\omega_k} = \frac{x}{X_0}\left(\frac{4}{3\omega_k} - \frac{4}{3E} + \frac{\omega_k}{E^2}\right) \approx \frac{4}{3}\frac{x}{X_0}\frac{1}{\omega_k}, \tag{45}$$

where X_0 is the radiation length (g cm^{-2}) and $y = \omega_k/E$ the fraction of the electron's energy transferred to the radiated photon. The approximation can be made because the electrons and positrons from photon conversions have large enough energies due to the forward boost. Rewriting this in terms of the photon transverse momentum k_T gives

$$\frac{dN_\gamma}{dk_\mathrm{T}} = \frac{4}{3}\frac{x}{X_0}\frac{1}{k_\mathrm{T}}, \tag{46}$$

through the trigonometric relation

$$\frac{d\omega_k}{dk_\mathrm{T}} = \cosh\eta, \quad \omega_k = k_\mathrm{T}\cosh\eta. \tag{47}$$

The e^+e^- pair-production cross section in the complete-screening limit valid at high energies is given in Eq. (34.32) [44],

$$\sigma = \frac{7}{9}\frac{A}{X_0 N_A}, \tag{48}$$

where A is the atomic mass (g mol^{-1}) and N_A the Avogadro number (mol^{-1}). As such, the interaction probability P_int is given by

$$P_\mathrm{int} = \rho_N \sigma x = \frac{N_A}{A}\rho\sigma x = \frac{7}{9}\rho\frac{x}{X_0} = \frac{7}{9}\frac{x}{\tilde{X}_0}, \tag{49}$$

where ρ_N is the number density of scattering centers, ρ the density of the material and $\tilde{X}_0$ the radiation length in cm. This means that a photon converts in passive material with a probability of $7/9x/\tilde{X}_0$.

[10] That can have any origin

[11] That then radiate a photon

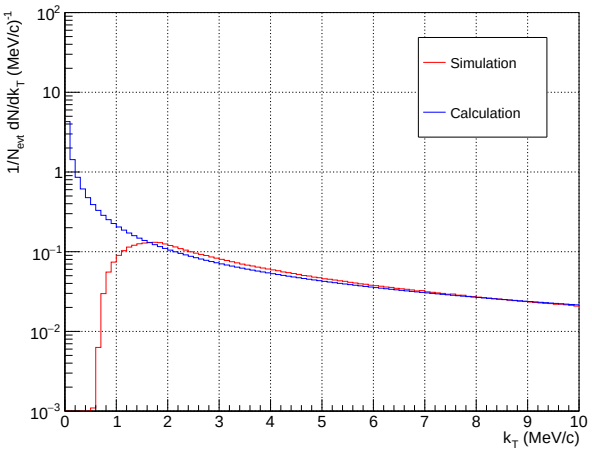

Figure 23: The transverse momentum spectrum of the external bremsstrahlung caused by decay photons for the pseudorapidity range $4 < \eta < 5$.

The pseudorapidity density for decay photons is represented by $dN_\gamma^{\text{decay}}/d\eta$. Putting this all together gives the transverse momentum spectrum for external bremsstrahlung caused by decay photons.

$$\frac{dN^{\text{ext. brems}}}{dk_{\text{T}}d\eta} = \frac{28}{27}\frac{dN^{\text{decay}}}{d\eta}\left(\frac{x}{\tilde{X}_0}\right)^2\frac{1}{k_{\text{T}}}. \tag{50}$$

In proton-proton collisions at $\sqrt{s} = 7\,\text{TeV}$, $dN_\gamma^{\text{decay}}/d\eta \approx 4$ which is approximately independent from η, Ref. [46]. According to Ref. [47], the charged particle multiplicity was found to scale with $\frac{dN_{\text{ch}}}{d\eta} \propto s^{1.03(2)}$. Due to the isospin symmetry of $\pi^\pm$ and π^0, the neutral pion multiplicity is expected to behave the same way. Since the biggest contribution by far to the decay photon spectrum comes from the channel $\pi^0 \to \gamma\gamma$, $dN_\gamma^{\text{decay}}/d\eta$ is assumed to scale the same way too. For η mesons, which deliver the second most dominant contribution to the decay photon spectrum, the story is a little more complicated, but the multiplicity is assumed to scale the same way as described above. Thus, at $\sqrt{s} = 14\,\text{TeV}$, $dN_\gamma^{\text{decay}}/d\eta \approx 4.6$. This, together with the material budget shown in Fig. 19, allows for the calculation of the transverse momentum spectrum of the external bremsstrahlung caused by decay photons in the pseudorapidity range $4 < \eta < 5$, which is done in Fig. 23. In the figure, the spectrum given by the calculation (blue) is compared to what is retrieved from the simulation (red). The simulated spectrum is retrieved from the full external bremsstrahlung spectrum of Fig. 21 by only requesting the photons that match the criteria of being created through external bremsstrahlung from electrons that were created by pair-production through decay photons. The full list of criteria in the form of a decision tree is given in Fig. 24. Following the decision tree from the top, for every external bremsstrahlungs photon it is asked whether electrons or other charged particles emitted them. From those electrons it is requested which production process created them, and subsequently if this was through a photon[12]. Of those photons it is then requested whether they were created through the decay of a π^0 or η meson which has an angle of emission in the region $4 < \eta < 5$. As a last step, it is then requested that this π^0 or η found its origin in the primary vertex. At the end, 57.7% of the external bremsstrahlung created finds its origin through this particular channel.

[12]Pair production is not limited to photons only. Direct production of electron positron pairs has been observed in colliding pion-proton experiments [48]. O^2 uses this terminology to classify these production channels which is adopted in this thesis.

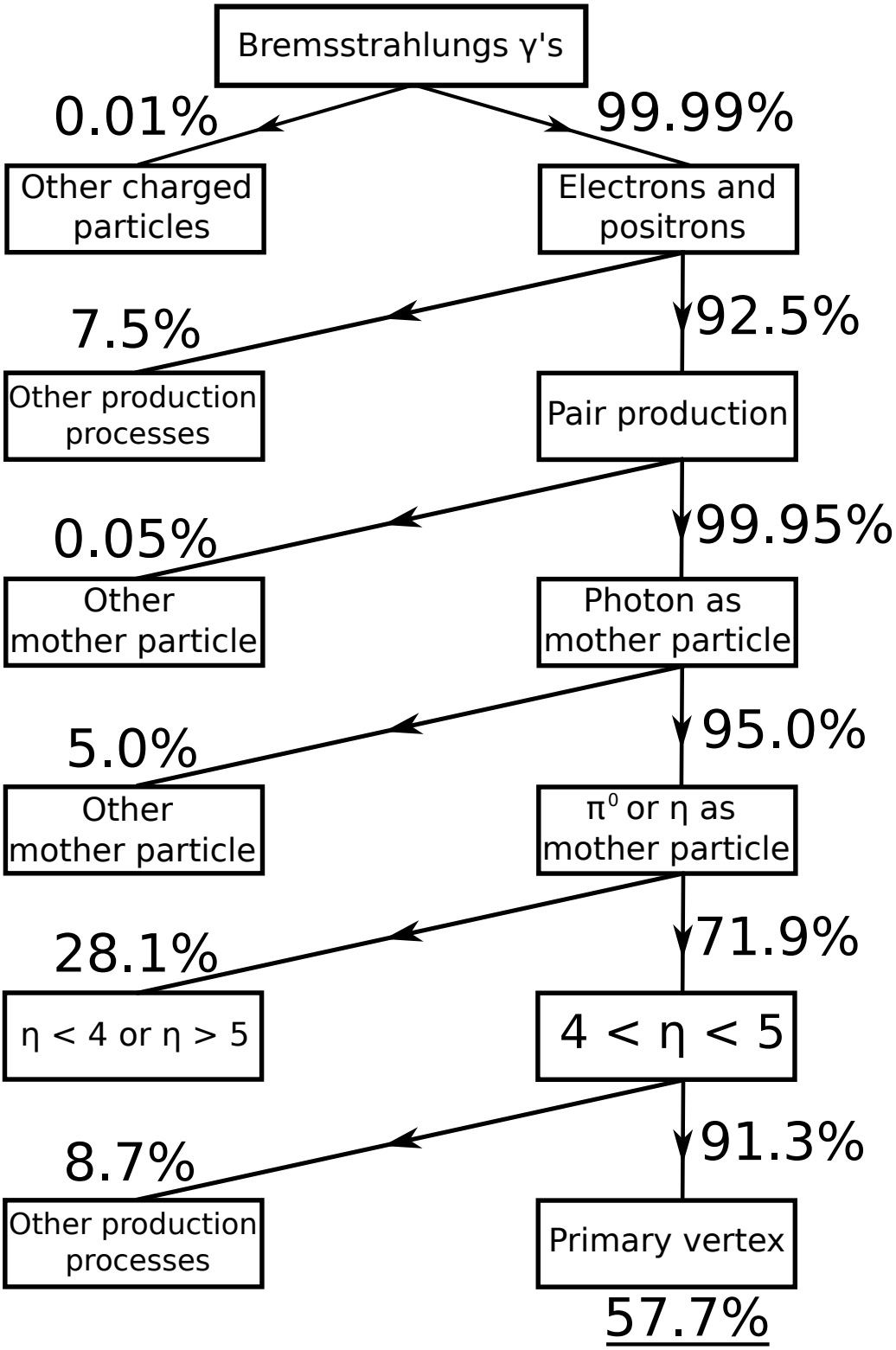

Figure 24: Decision tree to uncover external bremsstrahlung produced as a result of the decay of primary π^0 following the recipe presented in Ref. [19].

5.4.3 Secondary interactions/decays

The naming of the group "secondary interactions/decays" reflects the process in which these photons are produced, namely the decay of secondaries that are formed through interactions of highly energetic hadrons with material in front of the detector. An example retrieved from the simulation where a neutron with an energy of 51 GeV was incident on some material is given in the following:

$$n + M \rightarrow \pi^+ 2\pi^- 4\pi^0 2\gamma 4p 2n \eta \eta' K^+ 2\Sigma^0 1000020040 \tag{51}$$

where M stands for the material the neutron interacted with and 1000020040 is the pdg [44] code of a specific (hyper)nucleus. The hadrons that are created in these processes then decay through a channel where at least one photon is produced. The contribution to the soft-photon spectrum from these processes is entirely handled by GEANT4.

5.4.4 Hadronic inelastic interaction

This process has a lot in common with "secondary interactions/decays", but the difference is that the photons in this group are produced as a direct result of the hadron interacting with the material instead of requiring a decay of a hadron (i.e. a "secondary"). Again, the contribution to the soft-photon spectrum from these processes is entirely handled by GEANT4.

5.4.5 Other sources

This channel is to group all other sources together that do not contribute significantly to the soft-photon spectrum. These include, but are not limited to electron & positron nuclear interactions and miscellaneous hadronic interactions (that are not inelastic). These production channels were taken into account in the simulation, but their contributions were found to be so minimal that their exclusion has no visible effect on the results presented in this thesis.

5.5 Uncertainty on the background and background subtraction strategy

Fig. 21 shows that the dominant contributions to the total photon spectrum come from external bremsstrahlung and secondary interactions/decays which are both caused by in-material interactions of particles. The combined contribution from these two spectra are roughly a factor ≈ 30 higher than the signal, the internal bremsstrahlung. Sec. 6 will focus on the performance of the FCT and show ways how to reduce this background by implementing various cuts. In that section it is assumed that the uncertainty on the background is 5%, which will be argued in Sec. 7. To unveil the signal from the soft-photon spectrum, a background subtraction is performed, and thus it is assumed that the uncertainty on the background translates to the uncertainty on the spectrum after the background is subtracted, such that $\sigma_S = 0.05B$, where S is the signal and B the background. The significance of this measurement is then expressed as sig. $= \frac{S}{\sigma_S} = \frac{S}{0.05B}$. The significance will be presented for the case with the internal bremsstrahlung spectrum as predicted by Low's theorem, but also for the case when an enhancement is present as a factor of 4 w.r.t. the predicted internal bremsstrahlung spectrum, as was measured by a lot of experiment in the past, see Sec. 3.

5.6 ACTS and its use for ALICE 3

In its reconstruction workflow called Athena [49], ATLAS has incorporated the use of ACTS [43], which stands for A Common Tracking Software. ACTS promises to provide a detector-independent toolkit for (charged) particle track reconstruction in high energy physics experiments. The basic idea of ACTS is that the user can provide their detector geometry, of which ACTS then takes the material budget and maps this on the sensitive volumes which register the particles. By doing this a much simpler stepping algorithm for tracking can be used since only a few volumes have to be traversed, drastically speeding up the computation time. Tracking is then performed through the application of for example a Kalman Filter after which the vertices are reconstructed. Since these algorithms are all present in ACTS, the idea is that the user sets up a workflow in ACTS to perform the whole tracking

of the detector setup. Below, a summary of the workflow of ACTS is laid out and how it could be applied to the FCT. A more complete overview of ACTS can be found in Ref. [50].

Particle generation

Much like simulations in O^2, the first step is done through the simulation of an event. This can be done through e.g. PYTHIA or a so-called particle gun[13]. This is convenient as the LPG works with PYTHIA, ensuring the presence of internal bremsstrahlung photons.

Detector simulation

To perform the propagation of particles through the detector setup, ACTS can either employ GEANT4 or FATRAS, where FATRAS is an ACTS implementation for fast track simulation through a detector setup. In this step, the full, detailed detector geometry is used and hits are recorded in the sensitive volumes (e.g. a pixel sensor). In O^2, the ALICE 3 detector geometry is provided in ROOT geometry in a .root file. To use this in ACTS it has to be translated to either a .gdml format for GEANT4 or a format that FATRAS accepts. A magnetic field can then be set by the user and ACTS allows the user to specify multiple regions each with their own magnetic field.

Digitization

The digitization of recorded hits in a detector simulate the physical response of the detector and introduces efficiencies, uncertainties and clusterization to name a few detector effects. For digitization, the user has roughly four options which increase in complexity but also increase the accuracy of the simulation. In this stage, it is also possible to let ACTS analyze the data retrieved from a real detector through something called a "SourceLink".

- **1) Smear the hit position.** Through the smearing of the positions of the hits according to the spatial resolution of the sensitive volume, the performance of the detector is approximated.
- **2) Put the hits in a grid.** Along with the smearing introduced according to the spatial resolution of the sensitive volumes, the hits are placed in a grid. In this grid, since the readout is binary, no two hits can occupy the same cell. This more accurately incorporates the multiplicity dependence of the tracking.
- **3) Basic clusterization.** Along with the binary readout of the grid, clusterization of a hit is approximated based on the track length of the particle through the sensor. A clusterization algorithm can then be used to find and identify clusters.
- **4) Custom digitization.** Since the digitization is highly detector dependent, ACTS presents itself as "detector agnostic", meaning it knows nothing of the detector apriori and this has to be set by the user since the user knows best how their detector behaves. Among some other things, the user has to set their own
  - Digitization
  - Cluster finding
  - Charge sharing between neighbouring pixels
  - Alignment that aligns the detector geometry to the actual placement of the sensitive volumes in the real world.
  - SourceLink that translates the data provided by the user of their own experiment to something that ACTS can read (i.e. hits on sensitive volumes).

[13] Which just "shoots" a list of particles through the detector setup specified by the user

For the FCT, the spatial resolution is dictated by the MAPS used[14] and results in a spatial resolution of $\sigma_{\text{pos}} \approx 10\,\mu\text{m}$. Through this, a digitization on level 2 should be relatively easy to achieve since the MAPS are highly geometric. After cluserization algorithms have been developed based on the particular features of the MAPS, an extrapolation to level 3 seems feasible.

Seeding of tracks

To setup the track finding algorithm, first "seeds" have to be made from the hits from which a track can be formed[15]. A seed consists of 3 hits in a group from which a track can be developed. The criteria for three hits to form a seed can vary, but a specific example is the use of a Hough transform where each space point is transformed into a line and the intersection of the space points of a single track are in a common area, allowing the algorithm to thus form the seeds. To do this, ACTS makes a couple assumptions, two of which would need some additional logic for the FCT. ACTS assumes the magnetic field of the detector setup to be in the z-direction[16]. The FCT, however, sports a dipole magnet with a magnetic field in the y-direction. To accommodate for this, a simple transformation of the coordinate axis for the hits is required. In addition, ACTS assumes the tracks to originate from the primary vertex, or origin. For the FCT, which is in the forward direction and that assumes the origin of the particles it wants to track happen in the first couple of disks, this requires a dedicated study. For other telescope experiments, like NA60+ [51], it is reported that this was successfully implemented, but the performance of this is not actively studied by the ACTS developers and thus users, including those studying the performance of the FCT, have to find their own implementation.

Track finding and fitting

In a particle collision experiment track densities are high and computational power is limited. Track finding, through the use of a Kalman filter, is a computationally expensive operation, but ACTS tackles this through the usage of a Combinatorial Kalman Filter (CKF) and its smart way of mapping passive material. The sensitive volumes in the detector setup are enveloped in so-called approach layers. A representative layer is then formed containing the mapping recipe to represent the material budget in a simplified way, i.e. solely on the representative layer. This material map is retrieved from the performing geantino scans with GEANT4. Doing this, ACTS significantly reduces computational times by requiring a less complicated step sequencing for the CKF. Starting from the seed, the CKF evolves the track by considering the hits at each sensitive surface that is encounter, branching the χ^2 fit and selecting the best track candidates. Since refitting of a found track will be done anyway, smoothing in this stage can be dropped to save computation time.

Since the goal of the FCT is to track low energy electrons, a CKF is not the optimal choice for track finding and fitting. As a CKF through the Kalman formalism performs well for Gaussian uncertainties, it will not perform well for the tracking of electrons, especially those of low-momentum. The energy-loss through bremsstrahlung for electrons in matter is highly non-Gaussian and follows a Bethe-Heitler distribution instead. Through a so-called Gaussian Sum Filter (GSF), the Kalman-Filter is extended to handle non-Gaussian uncertainties by modeling the track as Gaussian mixture approximating the Bethe-Heitler distribution. Ref. [52] presents the performance of tracking with ACTS for electrons with a transverse momentum distribution of 500 MeV to 100 GeV and a uniform distribution in $|\eta| < 3$, but this is momentum range is still outside that of the FCT, which aims to track electrons with momenta below 500 MeV. Additional studies are therefore foreseen in this regime.

Ambiguity resolution

Track finding, due to its combinatorial nature, is often plagued by a significant contamination of duplicate fake track candidates. After all, one seed can only sprout one track. In order to minimize this contamination, an ambiguity resolution algorithm is implemented based on a scoring function that

[14] same as the outer tracker

[15] or sprouted to keep the terminology in the same theme

[16] much like the solenoidal fields present in ALICE, ATLAS and CMS

evaluates individual track candidates through its track parameters. The remaining track candidates are fitted again in a final precision fit to extract the parameter estimates. These tracks are then used for reconstruction.

Vertex reconstruction

The final step is to reconstruct the primary vertex of a collision. ACTS has a primary vertex finder, but not a secondary vertex finder, or even a V^0 finder. This is because the inclusion of a secondary vertex finder has not aligned with the primary focus of the ACTS developers yet, but studies are on the way to include it. This complicates track reconstruction for the FCT, since ideally, it would want to benefit from the V^0 finding and consequent photon reconstruction that follows from it to relate the photon to the primary vertex, the origin of the internal bremsstrahlung.

5.6.1 ACTS summary for the FCT

As it stands at the time of writing, ACTS needs to be equipped with custom code to allow either for secondary vertex reconstruction, or the vertex to be reconstructible at a point in space that is not the primary vertex. The study of the implementation of a GSF to lower energetic regions is also needed to ensure good performance for the track finding. Despite its current shortcomings, ACTS is a promising toolkit for the FCT since it already incorporates much of what is needed to perform tracking. In addition, the digitization scheme for the FCT needs to be developed, but since the MAPS that are used are the same as for the outer tracker disks of ALICE 3, the FCT is expected to be able to piggy back on the results of the study for the outer tracker disks.

6 Performance of the FCT for the measurement of the soft-photon spectrum

To measure the soft-photon spectrum produced in non-diffractive proton-proton collisions, the only photons of interest are those that actually originate from the primary vertex, yet, as was shown in Fig. 21, the hadronic decay, external bremsstrahlung and secondary decay spectra completely outshine the internal bremsstrahlung spectrum. The external bremsstrahlung spectrum is about a factor 30 higher than the internal bremsstrahlung spectrum, and, annoyingly enough, also shares the $1/k_{\mathrm{T}}$ relation for the shape of its distribution. In order to reduce the background, multiple strategies can be applied that make use of the differences between the photons from the sources of background. This chapter will discuss the use of a cut on the pointing angle, a geometric cut that relies on the distance of a reconstructed photon to the closest charged particle track in the FCT, a veto that excludes events containing an electron in the acceptance of the FCT and a layout of ALICE 3 with a conical window in the beam pipe to reduce the material budget. The goal is to perform a background subtraction to isolate the internal bremsstrahlung, the effectiveness of which is of course defined by the uncertainty on the background.

6.1 Pointing angle cut

The pointing angle is defined by the angle between the momentum vector of the particle and the vector of the position of the particle at which it was measured in the detector starting at the primary vertex. If a particle originates from the primary vertex, its momentum and position vector point in the same direction, giving an angle of 0 rad between the two of them. This is extremely useful for photons, since their trajectory through the detector is straight because it is unaffected by the solenoidal magnetic field of ALICE 3. This is in contrast to charged particles whose tracks are bent in the presence of a magnetic field. Consider a photon that finds it origin through some interaction of a particle with material in front of the FCT. This process can be either external bremsstrahlung, a hadronic inelastic interaction or the decay of a secondary particle which was created through a hadronic interaction with material or the annihilation of positrons in flight. For example for external bremsstrahlung, electrons are by far the dominant particles to emit a photon. Since electrons are charged, their trajectories are bent by the magnetic field, and in addition, they scatter when they traverse material, which also alters their trajectory. That, in combination with the way electrons are produced, predominantly from photon pair-conversions to e^+e^- and the angle between the emitted pair being non-zero, cause the pointing angle to be non-zero of a large portion of the external bremsstrahlung photons. However, since the FCT is in the forward direction, most of the momentum of particles produced in the acceptance of the FCT is in the z component which is unaffected by the solenoidal field along that axis. This causes electron to not bend as much as they would in the central[17] region, and thus the pointing angle is smaller. This causes the external bremsstrahlung spectrum to be persistent, although significantly reduced, even after the application of a cut on the pointing angle. As discussed in previous chapters, the achievable pointing angle resolution is 0.025 rad based on tracking studies published in the LoI [8]. The photon spectrum shown in Fig. 25 is the soft-photon spectrum to arrive at the FCT after the application of a cut on the pointing angle. As can be seen in the figure, the external bremsstrahlung spectrum is reduced by roughly one third, the secondary interactions/decays spectrum is significantly reduced as well and the background coming from hadronic inelastic interactions is as good as gone. The corresponding fraction per channel of the total spectrum is given in Fig. 26. This figure clearly shows the impact of the cut on the pointing angle on the reduction of the secondary interactions/decays photon channel when compared to the spectrum when the cut on the pointing angle is not applied, see Fig. 22. The corresponding significance and signal-to-background ratio of this spectra is given in Fig. 27.

[17] small psuedorapidity

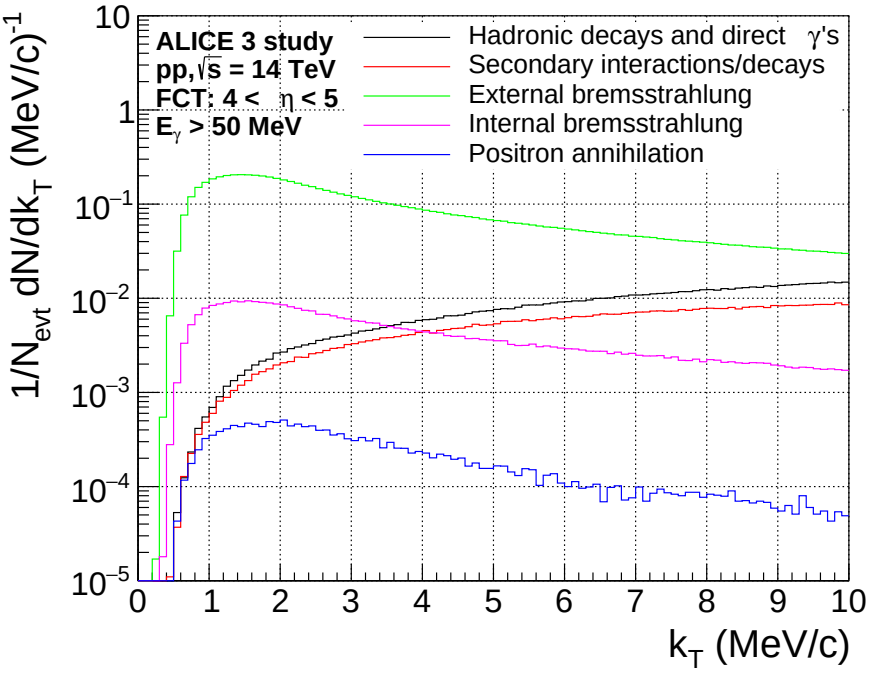

Figure 25: The photon spectrum at the FCT after the application of a cut on the pointing angle.

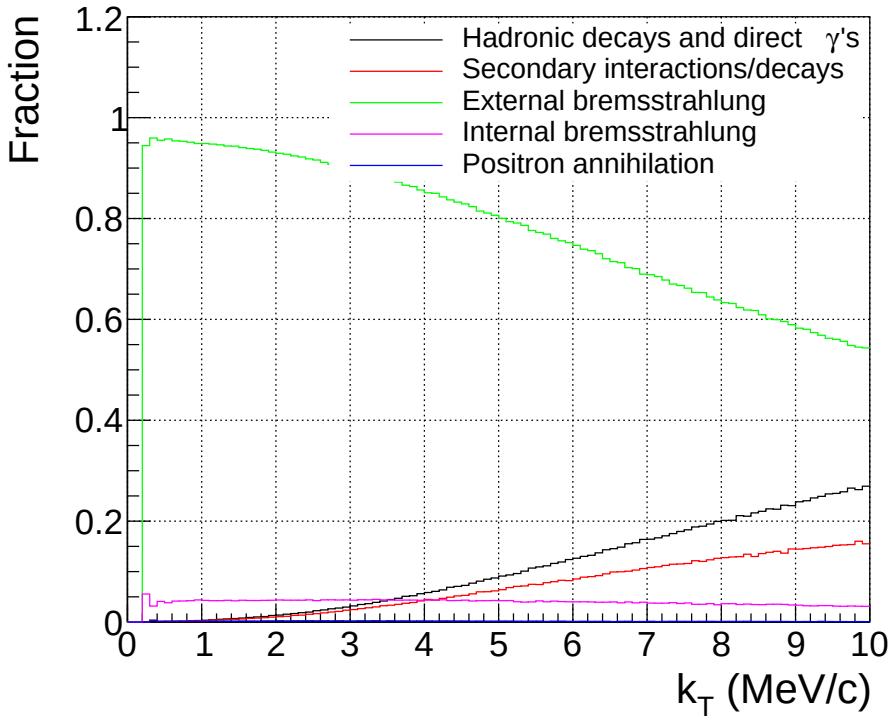

Figure 26: The fraction per channel of the total photon spectrum.

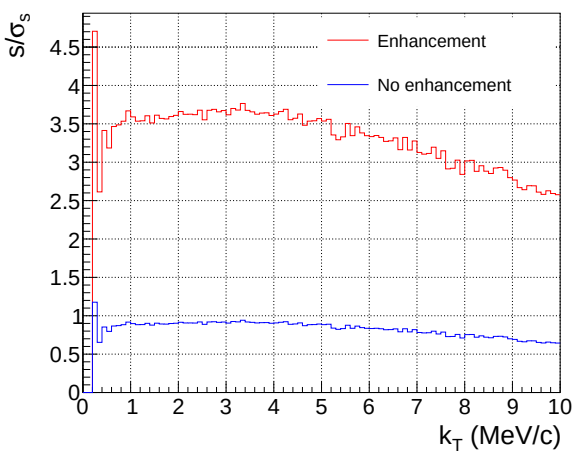

(a) Significance

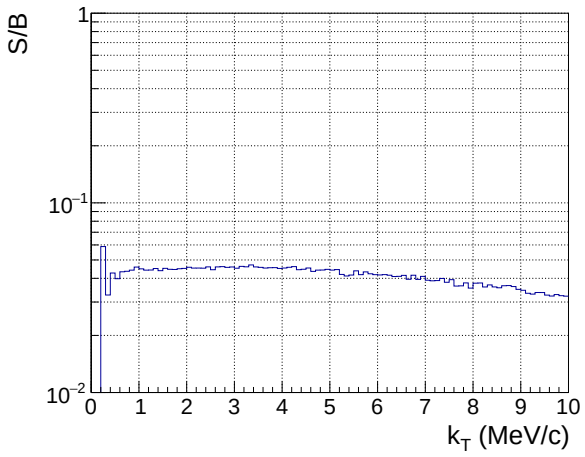

(b) Signal-to-background ratio

Figure 27: The significance assuming a 5% uncertainty on the background after subtraction of the background from the data is shown in the left figure. The red line shows the case that an enhancement of a factor 4 of the internal bremsstrahlung is indeed present, the blue line shows the case when the enhancement is not the present. The figure on the right shows the expected signal-to-background ratio when no enhancement is present.

6.2 Cut on the distance to the closest charged particle

To reduce the background further a cut based on the distance of a photon in the FCT to the closest charged particle in the same disk is applied. This distance is defined by

$$d = \sqrt{(x_\gamma - x_q)^2 + (y_\gamma - y_q)^2}, \tag{52}$$

where $(xy)_\gamma$ is the position of the reconstructed photon on the disk of the FCT and $(xy)_q$ the position of the charged particle track closest to that photon on the same disk. From now on, the distance of a photon to the closest charged particle is referred to as d_{cq}. The advantage of this cut is that the momentum of the charged particle does not need to be reconstructed, rather only a track needs to be associated to it. The distribution of the distance of photons from different sources to the closest charged particle on the first disk of the FCT is given in Fig. 28. What can be seen is that the distribution for external bremsstrahlung is strongly peaked where d_{cq} is close to 0, so a cut on this value to exclude those photons that satisfy $d_{cq} < a$ proves beneficial. It must be noted that the values in the bin where $d_{cq} = 34\,\text{cm}$ of the figure are not a strange artifact. Rather, since the diameter of the first disk of the FCT is 34 cm, those events that did not contain a charged particle but did contain a photon (effectively rendering d_{cq} to be undefined) where placed there. Since no cut was placed to exclude them, they are there to complete the spectrum. To figure out the optimal value a to place the cut on d_{cq}, the ratio of cut external and internal bremsstrahlung as function of the cut $d_{cq} < a$ is given in Fig. 29. The integrated significance over k_T as a result of this cut is given on the right in the same figure.

The integrated significance continuously rises as the cut on d_{cq} becomes stricter, but as seen in the figure on the left, the amount of the internal bremsstrahlung that is cut rises quickly too. To avoid the regime where statistical fluctuations dominate, the cut on d_{cq} is limited to 5 cm. To figure out why this cut is effective, it is useful to observe the same photon spectra as function of their origin of creation in z, see Fig. 30.

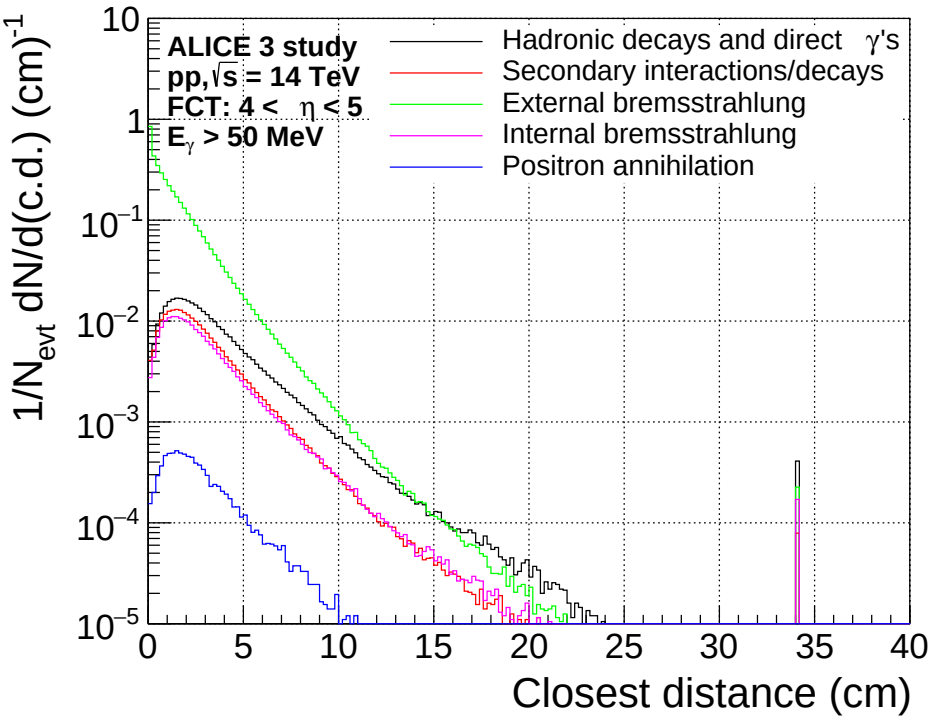

Figure 28: The spectrum of the distance of photons from different sources to the closest charged particle on the first disk of the FCT.

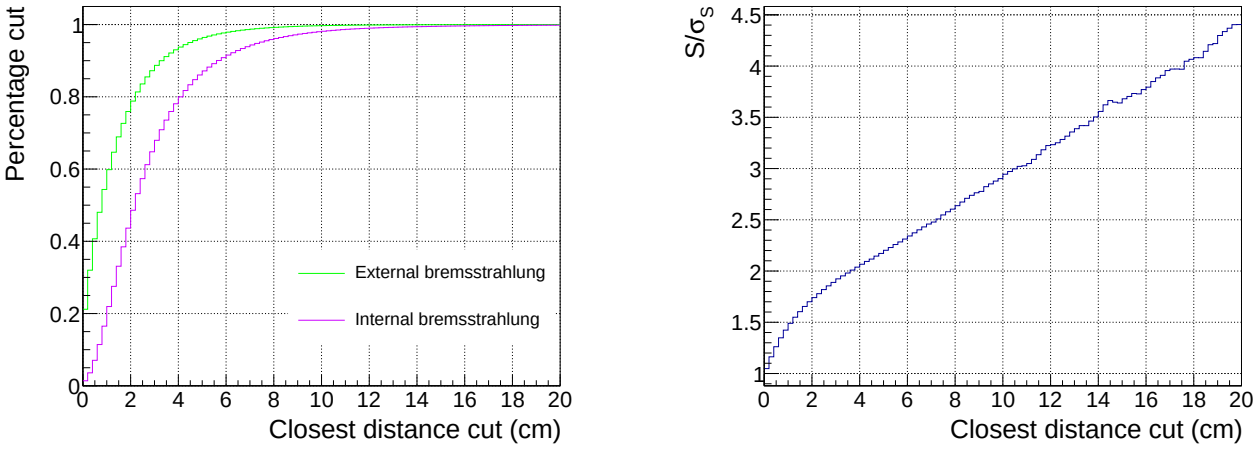

(a) (b)

Figure 29: The ratio of cut external and internal bremsstrahlung as function of the cut $d_{cq} < a$ (left). The integrated significance assuming an uncertainty on the background of 5% as function of the cut $d_{cq} < a$ (right).

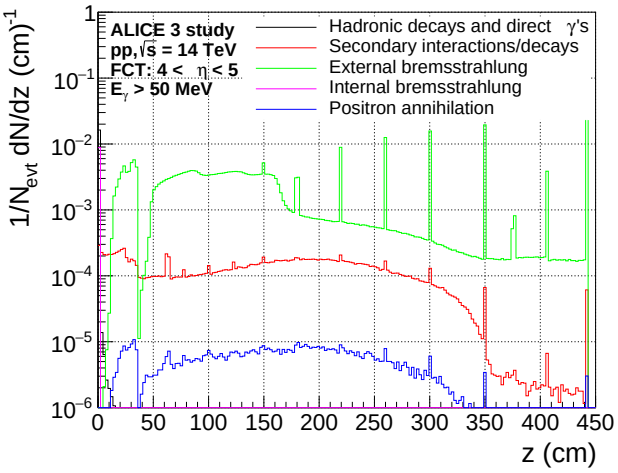

(a) Spectrum before the cut

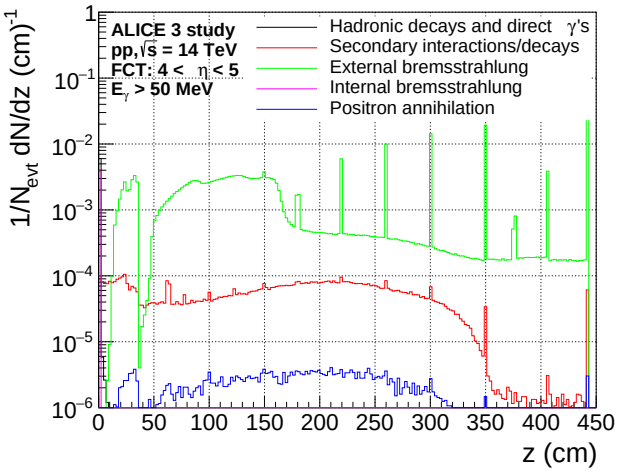

(b) Cut spectrum

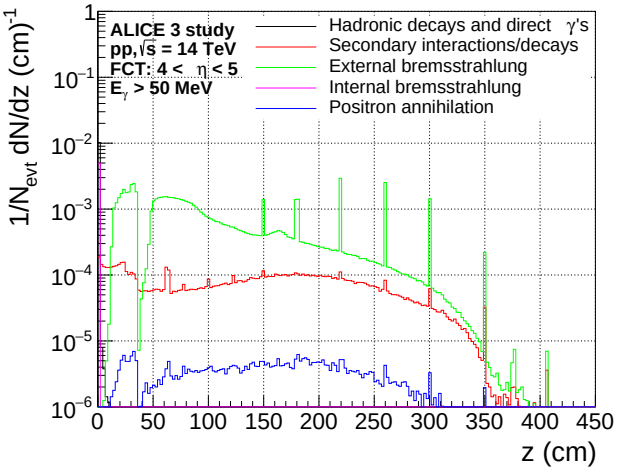

(c) Remaining spectrum

Figure 30: The photon spectrum to arrive at the FCT as function of the photon origin in z for the spectrum before the cut (top left), the spectrum that is excluded as a result of the cut $d_{cq} < 2\,\text{cm}$ (top right) and the remaining spectrum after the cut $d_{cq} < 2\,\text{cm}$ (bottom) for the different sources of soft photons.

What this shows is that the cut on d_{cq} is especially effective to reduce the external bremsstrahlung that is created close to the FCT in z. An interesting observation is that the geometry structure of ALICE 3 can be retrieved from these figures. To name a few structures, the "dip" of the external bremsstrahlung spectrum can be related to the radial wall of the beam pipe at $\approx 37\,\text{cm}$ and the disks of the outer tracker are clearly visible as sharp peaks at their respective z position. The external bremsstrahlung that is created closer to the interaction point ($z = 0$) is also cut significantly, but there the correlation between the distance to the FCT and d_{cq} is not as strong due to multiple scattering, the presence of the solenoidal magnetic field and separation of the charged particle and its emitted photon due to the initial angle between them and the distance traveled. The photon spectrum after the application of the cut $d_{cq} < 2\,\text{cm}$ is given in Fig. 31. The corresponding fraction per channel of the total spectrum is given in Fig. 32. As a result of this cut, the increase of the fraction internal bremsstrahlung of the total spectrum is clearly visible. Again assuming an uncertainty on the background of 5%, the significance is shown in Fig. 33 on the left. The signal-to-background ratio is shown in the same figure on the right.

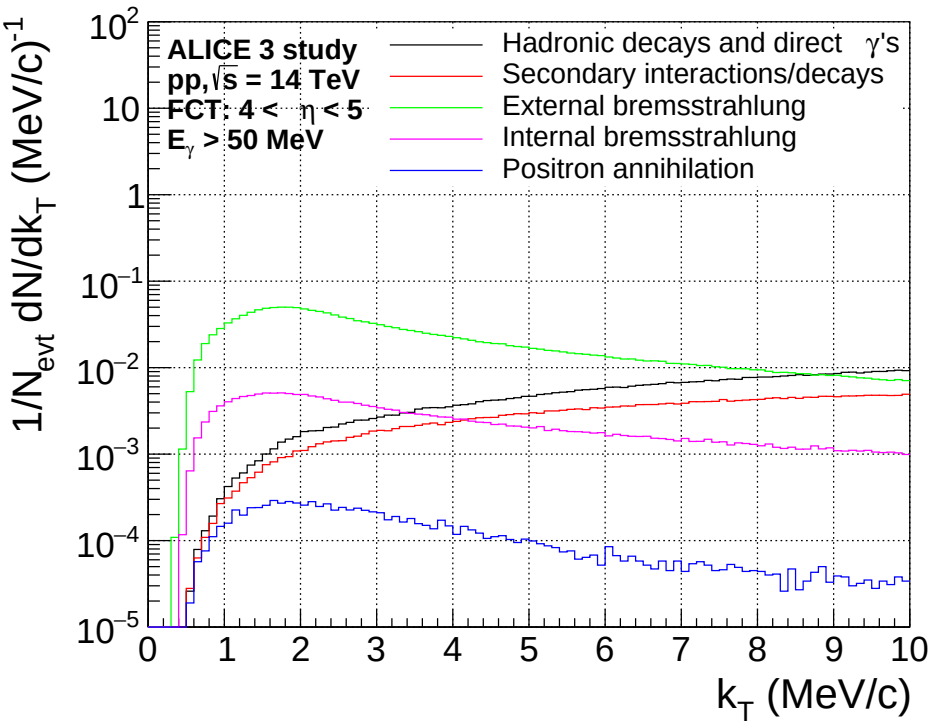

Figure 31: Photon spectrum after the application of the cut on the distance to the closest charged particle $d_{cq} < 2\,\text{cm}$.

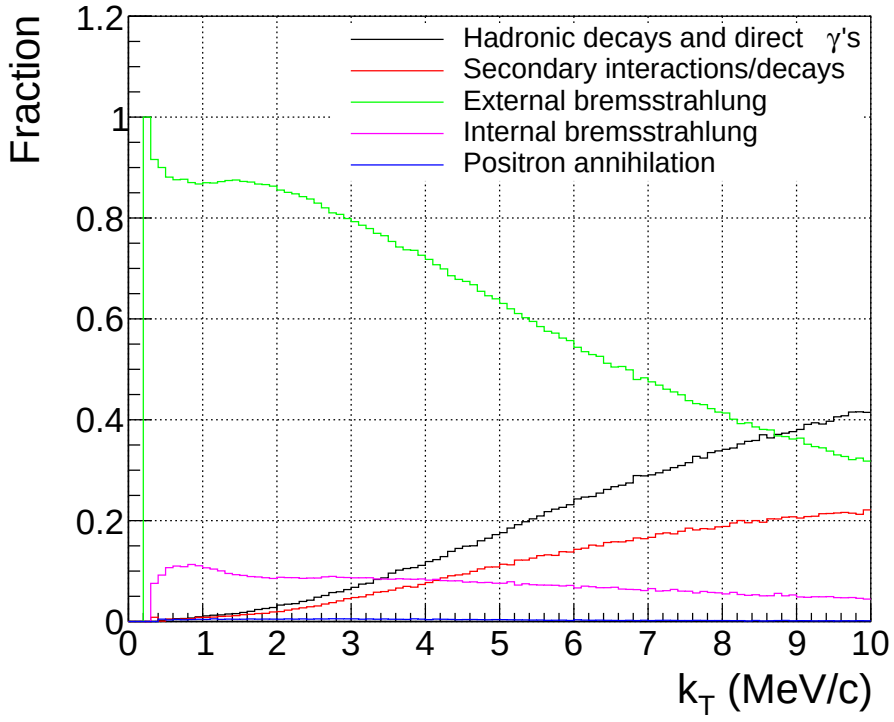

Figure 32: The fraction per channel of the total photon spectrum.

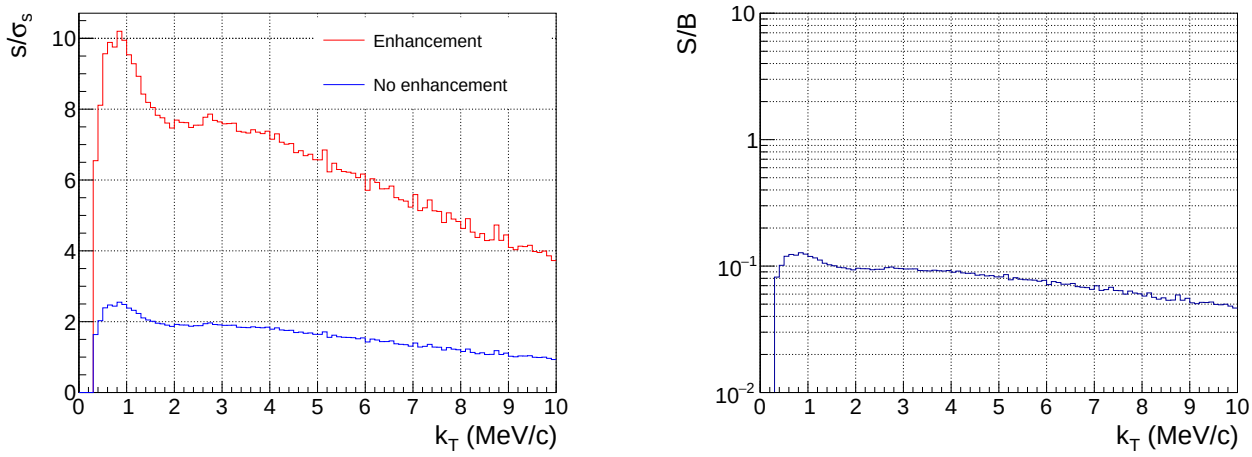

(a) Significance

(b) Signal-to-background ratio

Figure 33: The significance assuming a 5% uncertainty on the background after subtraction of the background from the data is shown in the figure on the left. The red line shows the case that an enhancement of a factor 4 of the internal bremsstrahlung is indeed present, the blue line shows the case when the enhancement is not the present. The figure on the right shows the expected signal-to-background ratio when no enhancement is present.

6.3 Window in the beam pipe

After the cut on d_{cq}, there is still a large amount of background left as can be seen in Fig. 31. To further reduce this, it is important to understand the origin of the background. The dominating contribution is still external bremsstrahlung formed by electrons passing through material in front of the FCT. To that end, the contribution in percentages of the total amount of photons of the spectra in Fig. 31, except hadronic decays and internal bremsstrahlung, as function of their spatial origin is shown in Fig. 34. What becomes clear is that the beam pipe, and especially the part in the pseudorapidty region of the FCT ($4 < \eta < 5$) is the main source of the remaining photons. This motivates a different shape of the beam pipe in order to reduce the effective material budget in front of the FCT. Because the primary vacuum vessel has a significant larger radius than the other part of the beam pipe at the A-side, a conical shape to increase the angle of incidence of traversing particles is a logical choice. This conical shape is referred to as the window. Fig. 35 shows the layout of ALICE 3 with the inclusion of such a window. In this design, the window has a length of 150 cm and with this setup the third set is simulated, see Tab. 11. There is a gap of about half a centimeter between the window and the first disk of the outer tracker. This means that the support structures of the outer tracker disks close to that point have to be made with stricter restrictions than the others, but the benefit for the measurement with the FCT is significant. With the inclusion of the window in the design of ALICE 3, the material budget in front of the FCT is consequentially reduced, as can be seen in Fig. 36 when compared to the setup with a straight beam pipe as seen in Fig. 19.

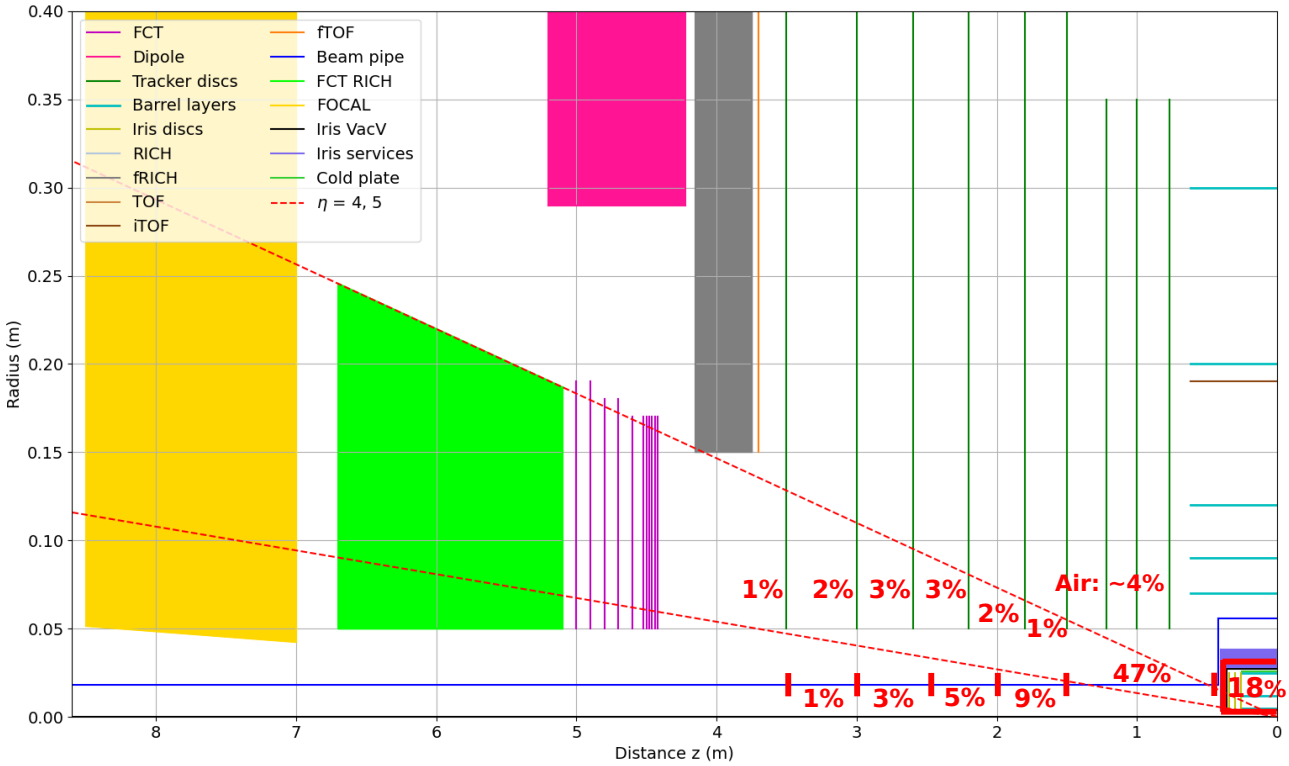

Figure 34: The contribution in percentages of the total amount of photons of the spectrum in Fig. 31 as function of their spatial origin.

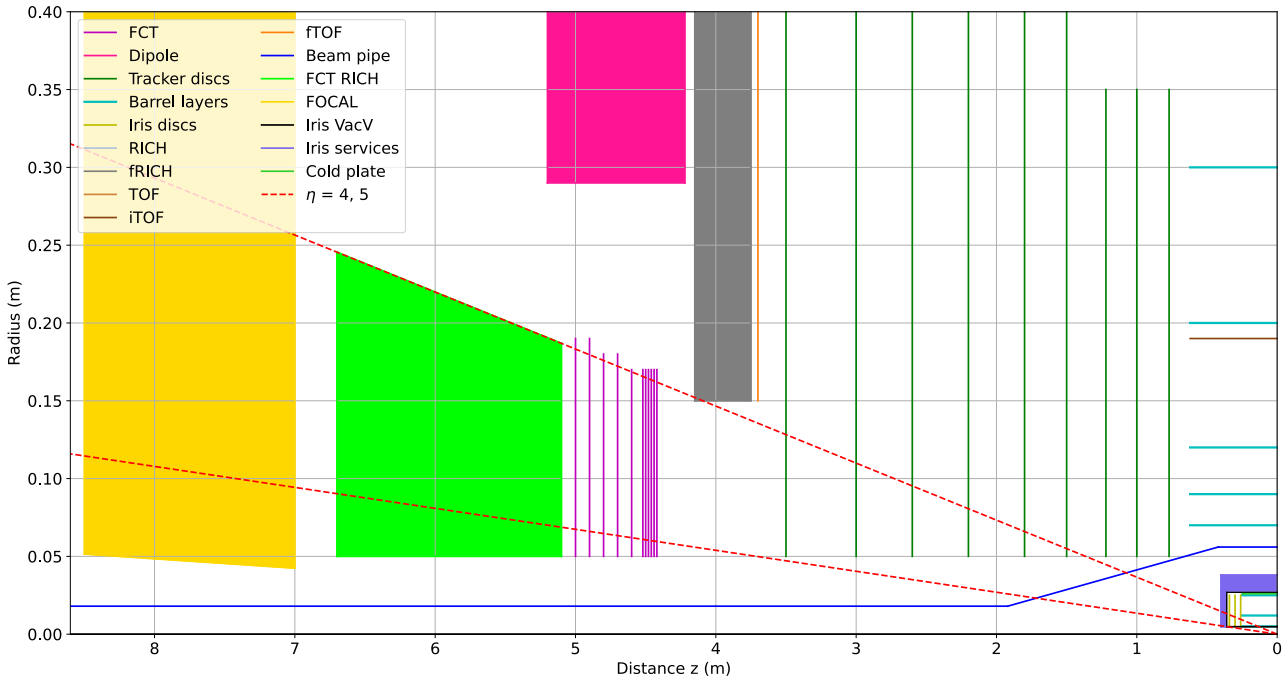

Figure 35: Window in the beam pipe in the ALICE 3 layout.

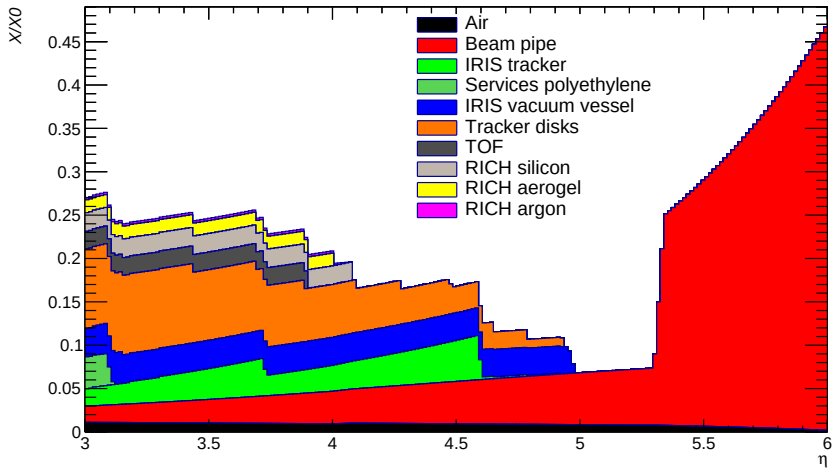

Figure 36: The material budget in front of the FCT in terms of x/X_0 as function of the pseudorapidity with a window in the beam pipe of the ALICE 3 setup.

After the application of the pointing angle cut and the cut on $d_{cq} < 2\,\text{cm}$, the photon spectrum to arrive at the FCT for this layout is given in Fig. 37. The corresponding fraction per channel of the total spectrum is given in Fig. 38. As the external bremsstrahlung gets reduced further, the contribution of hadronic decays and direct γ's starts to become more and more visible in the region $k_{\text{T}} > 7\,\text{MeV}/c$. For this setup with the window in the beam pipe, the contribution in percentages of the total amount of photons of the spectra in Fig. 37, except hadronic decays and internal bremsstrahlung, as function of their spatial origin is shown in Fig. 39. Comparing the contributions for the setups with and without a window in the beam pipe, the percentage of the photon spectrum coming from the section of the beam pipe that is in the pseudorapidty range $4 < \eta < 5$, it is significantly reduced. The contribution from IRIS tracker is now dominant and this clearly shows the two biggest sources of external bremsstrahlung and secondary decays.

Again assuming an uncertainty on the background of 5%, the significance is shown in Fig. 40 on the left. The signal-to-background ratio is shown in the same figure on the right.
Simulations with a window in the beam pipe that is of length 200 and 250 cm were also performed. However, in these cases the window cuts through the first disk of the tracker instead of barely passing under it. For these setups, a reduction in the size of the first disk of the tracker in the order of up to 1 cm is required which might impact the physics program of ALICE 3. The photon spectra along with the significance and signal-to-background ratio for these simulations are given in the Appendix, Figs. 62.

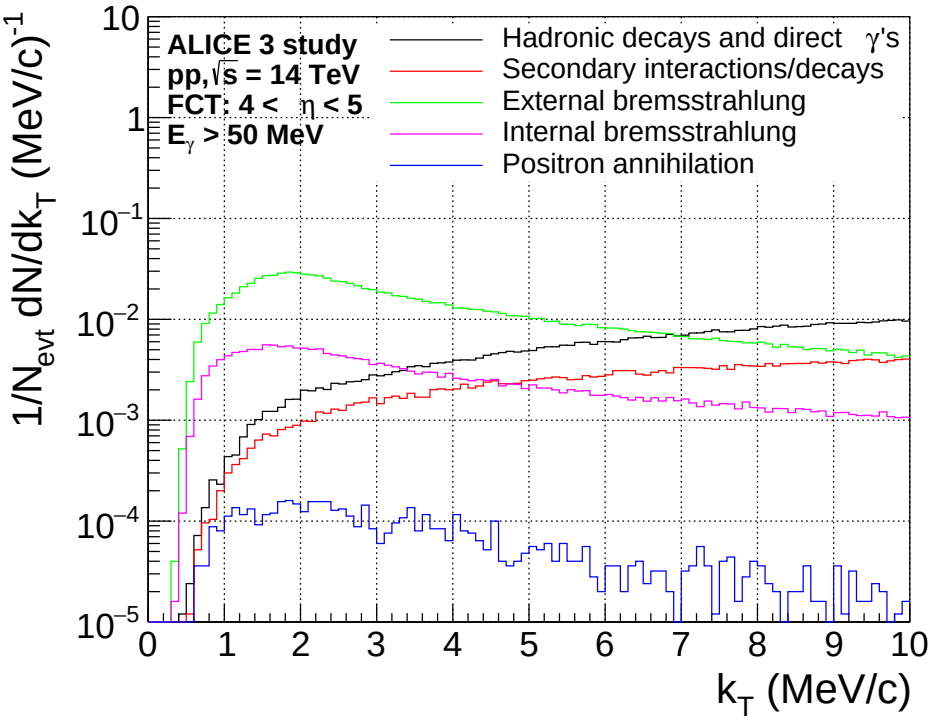

Figure 37: Photon spectrum to arrive at the FCT as function of the photon k_{T} with a cut on the pointing angle and distance to the closest charged particle $d_{cq} < 2\,\mathrm{cm}$. The layout of ALICE 3 contains a window in the beam pipe with a length of 150 cm.

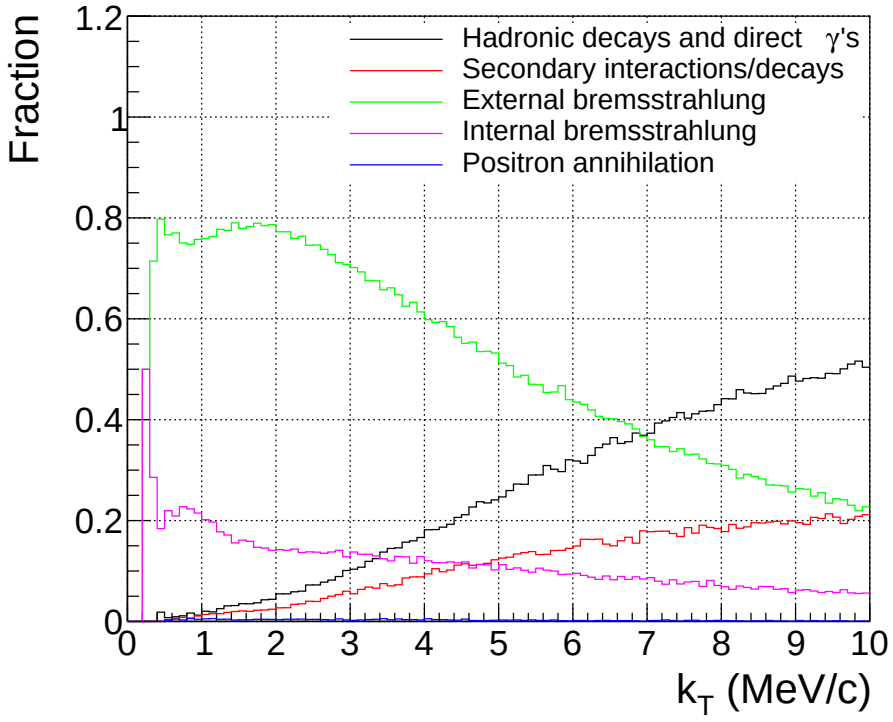

Figure 38: The fraction per channel of the total photon spectrum for the setup with a window in the beam pipe.

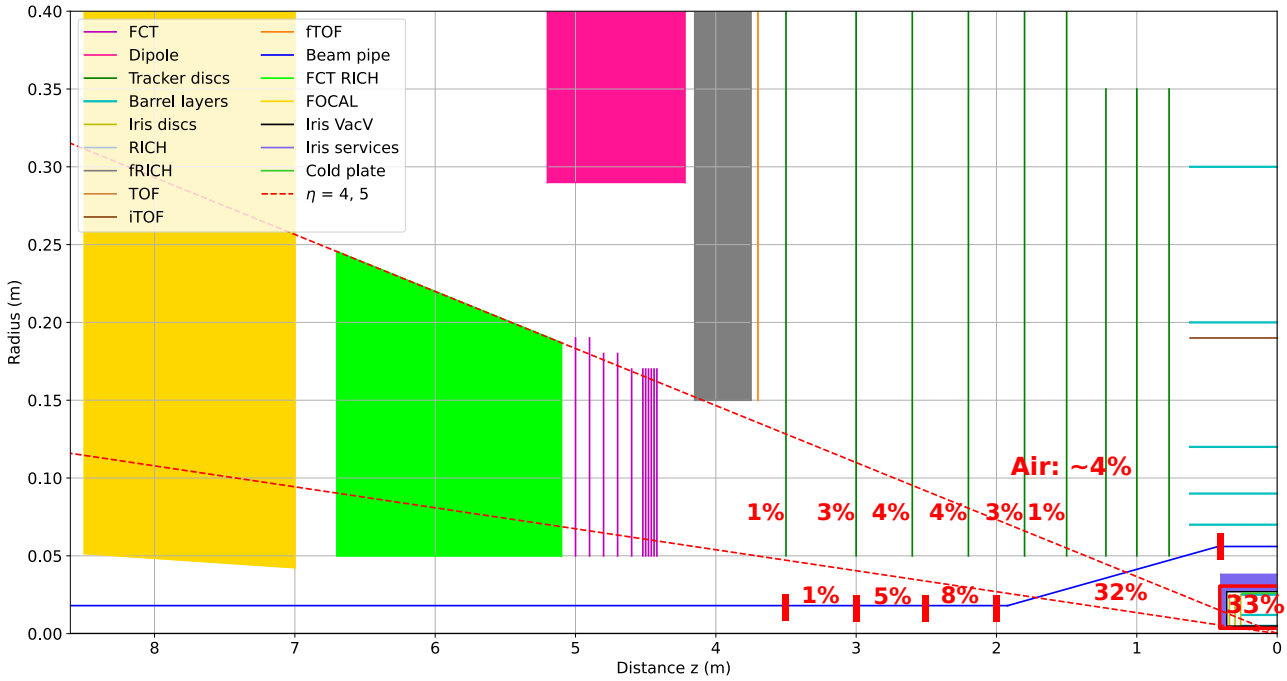

Figure 39: The contribution in percentages of the total amount of photons of the spectrum in Fig. 37 as function of their spatial origin for the setup of ALICE 3 with a window in the beam pipe.

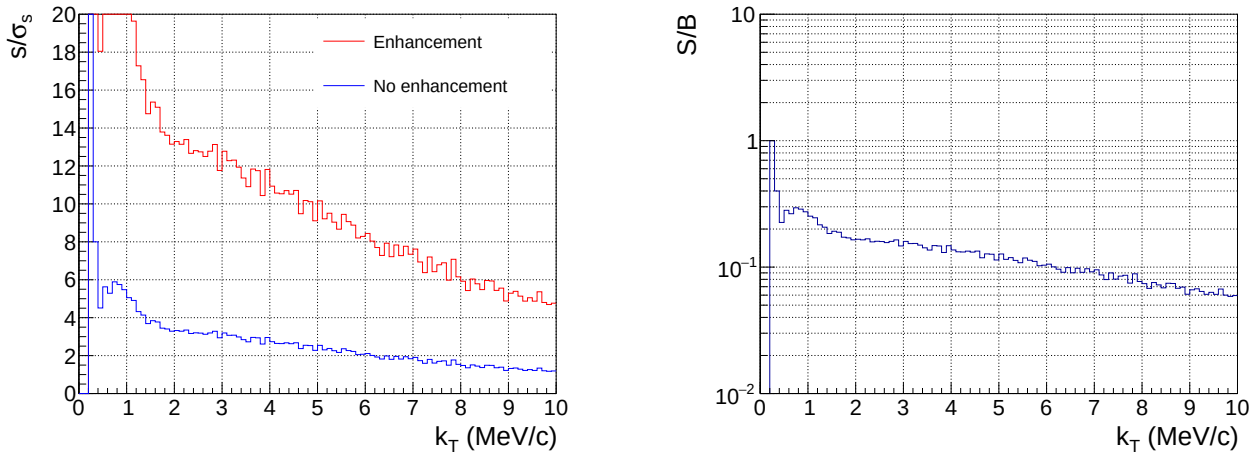

(a) Significance

(b) Signal-to-background ratio

Figure 40: The significance assuming a 5% uncertainty on the background after subtraction of the background from the data for the setup with a conical window in the beam pipe of ALICE 3 is shown in the figure on the left. The red line shows the case that an enhancement of a factor 4 of the internal bremsstrahlung is indeed present, the blue line shows the case when the enhancement is not the present. The figure on the right shows the expected signal-to-background ratio when no enhancement is present.

6.4 Ideal e^+e^- event veto

A defining difference between internal and external bremsstrahlung is that most of the external bremsstrahlung is created through electrons that radiate photons, whereas internal bremsstrahlung is mostly emitted by charged hadrons. This is mainly due to the fact that there are not many final state electrons created in a pp collision and final state charged hadrons are not as likely to radiate bremsstrahlung when interacting with material. Since the emission angle of bremsstrahlung is small, the responsible charged particle will end up in the spacial vicinity of the photon it emitted in the absence of a magnetic field. The solenoidal magnetic field of the ALICE 3 detector with a strength of 2 T in the $\hat{z}$-direction causes charged particles to bend in the xy-plane, but this is not a big influence, since in the forward direction the main component of the momentum of a charged particle is p_z. Therefore the photons and charged particle that created it, either through external or internal bremsstrahlung, will both end up in the acceptance of the FCT, assuming they are not destroyed or stopped through some interaction with the material in front. One could then ask if this could motivate the inclusion of the study to exactly figure out which final state charged hadron radiated a soft photon, but since ALICE 3 has little to no tracking capabilities in front of the FCT in the same acceptance, this would prove exceedingly hard. However, the aforementioned relation between photons and their producing charged particles motivates the use of an offline veto on events that contain an electron in the acceptance of the FCT, also studied in Ref. [45]. In similar fashion, DELPHI excluded jets with identified electrons to suppress external bremsstrahlung [17]. For this section, an ideal particle identification is assumed to explore the potential performance of such a veto. A more realistic approach is taken in the next section, Sec. 6.5.

6.4.1 Experimental setup

For this approach it is assumed that a single event-by-event analysis with the FCT is possible, i.e. that ALICE 3 records enough ROFs which only contain 1 collision. Considerations about the feasibility of a single event-by-event analysis are given in Sec. 4.3. The dataset for this analysis is the "Default ALICE 3" as described in Sec. 5.2. To perform the veto, the identification of the particles that reach the last layer of the FCT are requested per event and if any of the particles is identified as an electron, the corresponding event is vetoed. It must be noted that the FCT measures photons through the tracking of e^+e^- conversion pairs, and the events containing such a pair are therefore also vetoed through this method, but this does not necessarily introduce a problem through the following reasoning. In this section the focus lies on photon spectrum to arrive at the FCT. Since the first couple of layers of the FCT will function as conversion layers for the photons, it is reasonable to assume that the efficiency for the identification of a V^0 will be good. Electrons that are part of a V^0 would have to be excluded from the spatially isolated, single track electrons that the reasoning for this veto is based on. The actual conversion probability of a photon in the FCT is small, and as such, vetoing events that contain a converted photon did not worsen the result of this section significantly.

6.4.2 Results

The photon spectrum to reach the FCT by vetoing all the events that contain an electron in the acceptance of the FCT is given in Fig. 41. The significance, again assuming an uncertainty on the background is 5%, together with the signal-to-background ratio are given in Fig. 42. The gain in significance and signal-to-background ratio clearly motivate the inclusion of a particle identification detector that can provide a way to facilitate such a veto.

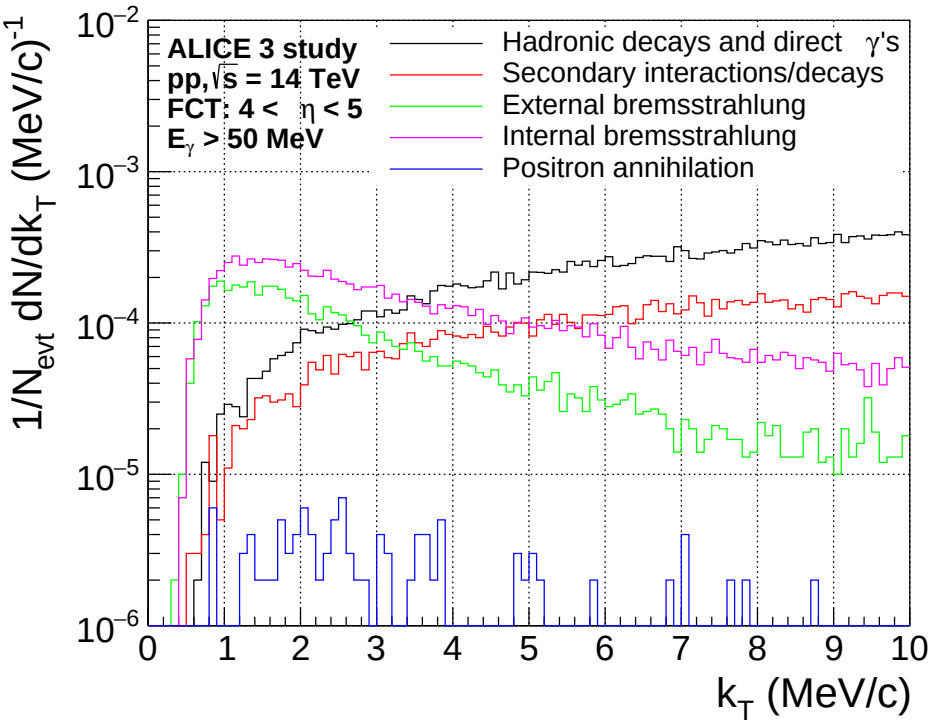

Figure 41: The photon spectrum to reach the event by vetoing all the events that contain an electron in the acceptance of the FCT.

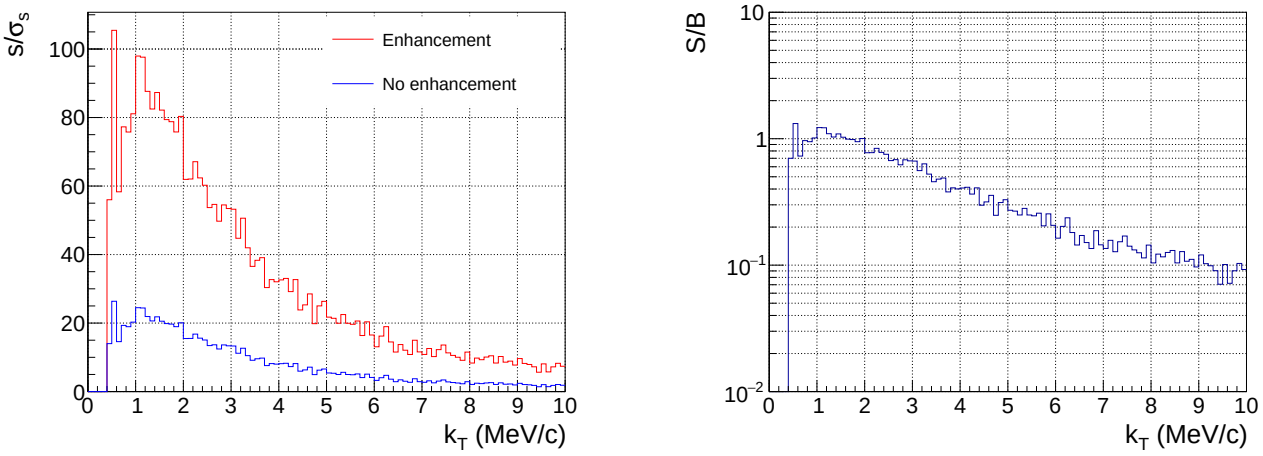

(a) Significance

(b) Signal-to-background ratio

Figure 42: The significance assuming a 5% uncertainty on the background after subtraction of the background from the data where events containing an e^+e^- are vetoed is shown in the figure on the left. The red line shows the case that an enhancement of a factor 4 of the internal bremsstrahlung is indeed present, the blue line shows the case when the enhancement is not the present. The figure on the right shows the expected signal-to-background ratio when no enhancement is present.

6.5 Cherenkov detector for ePID for e^+e^-vent veto

A more realistic approach for particle identification would be the inclusion of a Cherenkov detector either before or behind the FCT. In this section, the design and performance of such a detector is discussed. The simulation set "Default ALICE 3" is used for this section. To quantify the performance the Cherenkov detector behind the FCT needs to achieve, the momentum spectrum of the charged particles to arrive at the FCT is requested from the simulation and plotted in Fig. 43. To clarify, any of these electrons has a probability to emit an external bremsstrahlung photon in the momentum range in which the FCT is sensitive.

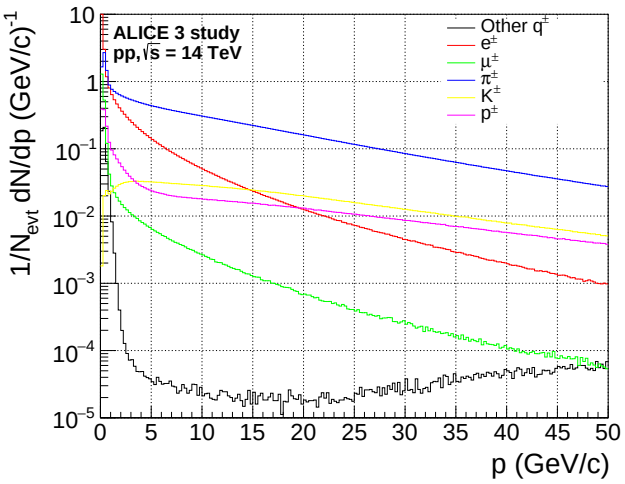

Figure 43: The charged particle momentum spectrum to arrive at the FCT.

The multiplicity of electrons to arrive at the FCT drops significantly as momentum increases. The ability to identify electrons with a momentum of up to $\sim 15\,\mathrm{GeV}/c$ will therefore act as a loose guideline.

In a transparent medium, the angle θ_{ch} at which a photon is radiated from a charged particle through the process known as Cherenkov radiation is given by

$$\cos\theta_{ch} = \frac{1}{n\beta} \tag{53}$$

where n is the refraction index of the medium and β the ratio v/c of the particle. The RICH and bRICH of ALICE 3 [32] will have a $n = 1.03$ to provide, together with the TOFs, an electron/pion separation up to $2\,\mathrm{GeV}/c$ through the reconstruction of the radiation angle together with a measurement of the momentum of the charged particle. This, however, is not sufficient when the momentum spectrum of the electrons to arrive at the FCT is considered.

In Fig. 44, the spectrum is replotted to show the cumulative fraction (0-1) of electrons as function of their momentum.

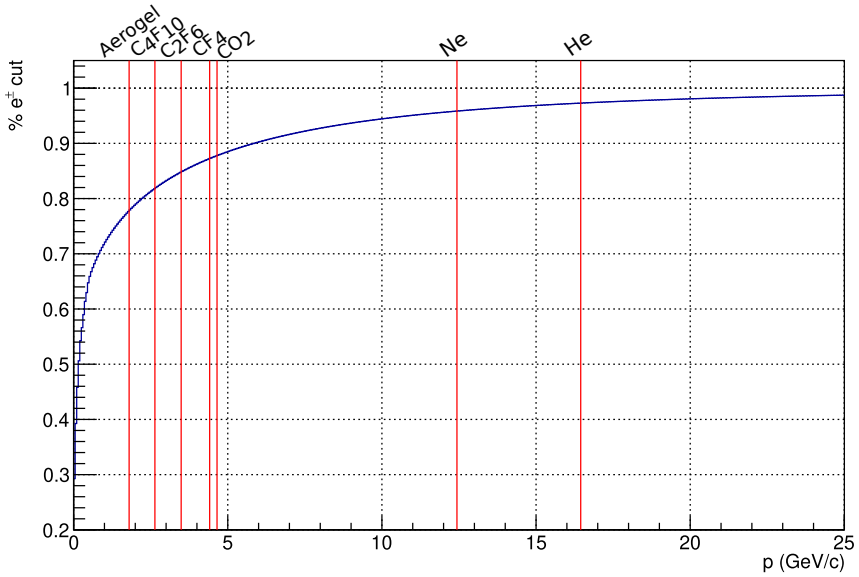

Figure 44: Cumulative momentum spectrum of electrons to arrive at the FCT. The momentum thresholds for different gasses for pions are indicated with a red line giving the theoretical distinguishing power between electrons and other charged particles based on the presence of photons.

Since the particle identification only has to provide a way to tell electrons apart from other charged particles, a shortcut is taken with respect to traditional RICH detectors where ring reconstruction is used to reconstruct the angle of emission of the photons with respect to the charged particle. Instead, the mere presence of radiated photons together with the momentum of the charged particle can be used to tell electrons apart from others. The theoretical maximum amount of electrons that can be identified with this principle through the usage of different gases is illustrated in the aforementioned figure. The momentum at which a charged particle starts to radiate photons, called the threshold momentum in this thesis, is achieved by setting $\theta_{ch} = 0$, to get $\beta_{\text{th}} = 1/n$ which leads to

$$p_{\text{th}} = \frac{m}{\sqrt{n^2 - 1}}, \tag{54}$$

where m is the mass of the charged particle. Gases are chosen for their low refractive index, whereas solids, even aerogel, have a relatively high refractive index.

The Cherenkov angle for different charged particles in both aerogel with $n = 1.003$ and different gases is given in Fig. 45.

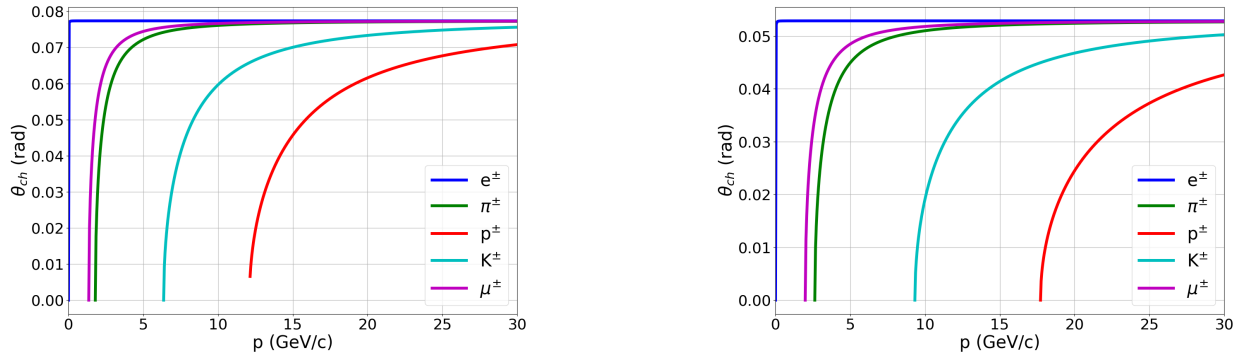

(a) Aerogel $n = 1.003$

(b) C_4F_{10}

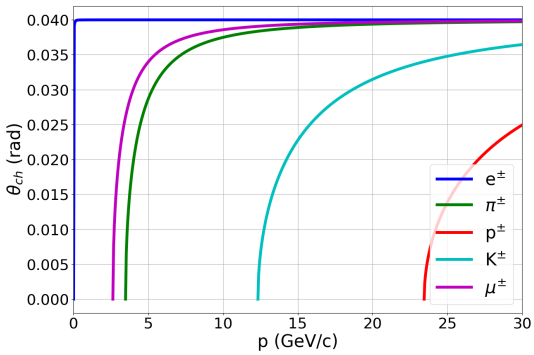

(c) C_2F_6

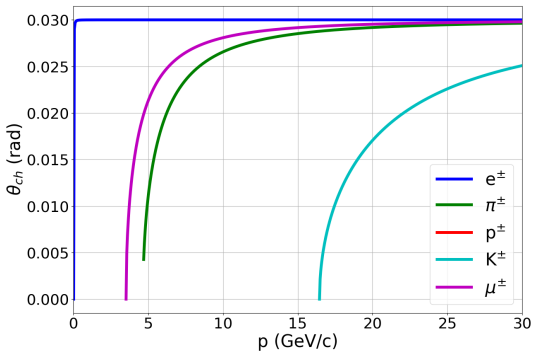

(d) CO_2

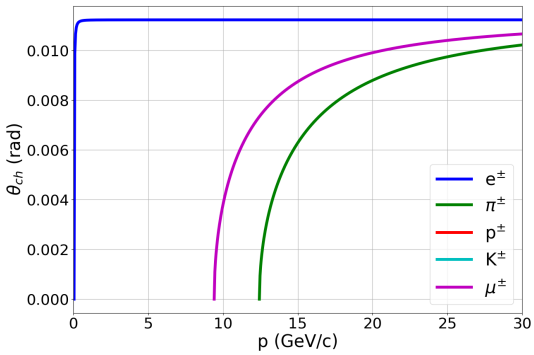

(e) Ne

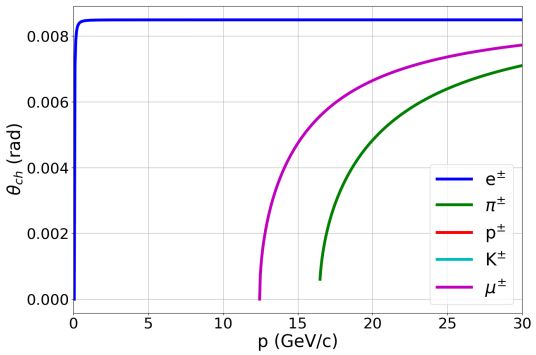

(f) He

Figure 45: Cherenkov angle as function of momentum for different charged particles in different mediums.

This figure serves to indicate the angular resolution that is required to be achieved for ring reconstruction if aerogel is used as a radiator. The method of identifying electrons based on the presence of photons makes a transparent gas a natural choice. Ring reconstruction when gas is used as a radiator, however, is far from trivial and requires the usage of spherical focusing mirrors. Frank-Tamm theory,

$$N_{\text{prod}} = \frac{\alpha}{\hbar c} Z^2 L \int_{E_1}^{E_2} \sin^2 \theta_{\text{ch}} dE_\gamma, \tag{55}$$

predicts the number of photons radiated (N_{prod}) in the emitted photon energy range $[E_1, E_2]$ when a charged particle with charge Z passes through a medium with refractive index n for a length L

in meters. In this formula, the β is hidden in the Cherenkov angle θ_{ch}. α, $\hbar$ and c are the fine structure constant, the reduced Planck constant and the speed of light, respectively. The gases that are considered, with their respective refractive index, momentum threshold for electrons & pions and the average number of photons radiated by an electron at $\beta = 1$ per meter through said medium for visible light are given in Tab. 12.

Medium name Molecular composition	Refractive index $(n-1)$	$p_{e^{\pm}\text{ th.}}$	$p_{\pi^{\pm}\text{ th.}}$	$\langle N_\gamma \rangle$ / m [380, 700] nm
Aerogel Aerogel dependent	3×10^{-3}	7 MeV/c	1.8 GeV/c	$3.3{\times}10^2$
Perfluorbutane C_4F_{10}	1.4×10^{-3}	10 MeV/c	2.6 GeV/c	$1.5{\times}10^2$
Hexafluoroethane C_2F_6	8×10^{-4}	13 MeV/c	3.5 GeV/c	88
Tetrafluormethane CF_4	5×10^{-4}	16 MeV/c	4.4 GeV/c	55
Carbon dioxide CO_2	4.5×10^{-4}	17 MeV/c	4.7 GeV/c	50
Neon Ne	6.3×10^{-5}	46 MeV/c	12.4 GeV/c	6.9
Helium He	3.6×10^{-5}	60 MeV/c	16.4 GeV/c	4.0

Table 12: The refractive index of aerogel is based on the lower end of refractive indices of commercially available aerogel [53]. The gases are assumed to be at atmospheric pressure.

In Fig. 46 the average number of photons produced within the visible spectrum for different kinds of charged particles per meter are plotted as function of the momentum for the aerogel and a variety of gases.

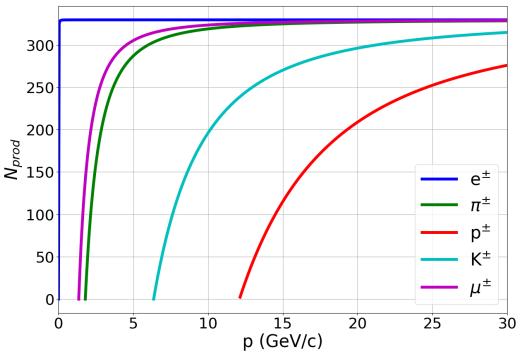

(a) Aerogel $n = 1.003$

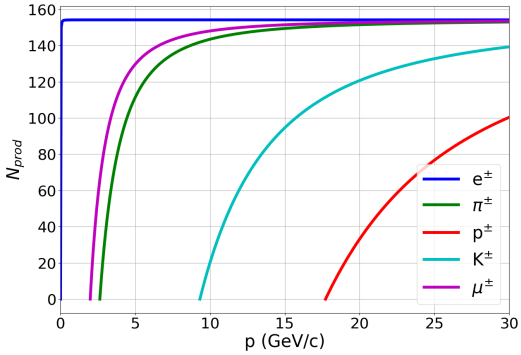

(b) C_4F_{10}

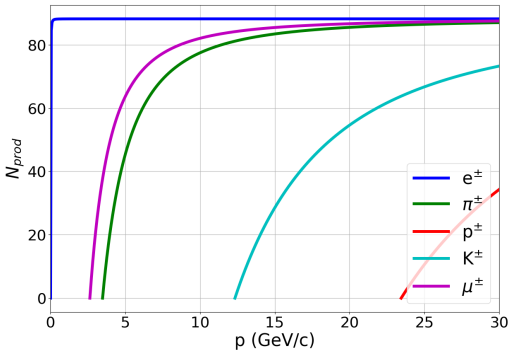

(c) C_2F_6

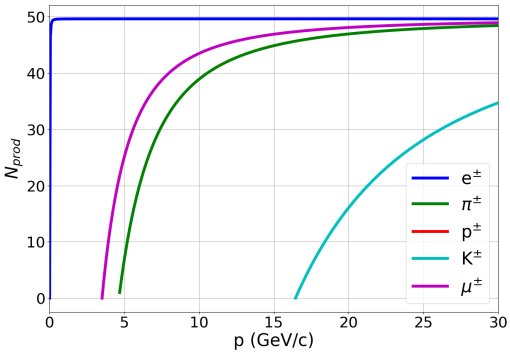

(d) CO_2

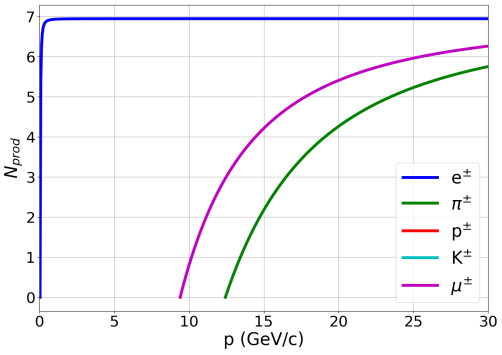

(e) Ne

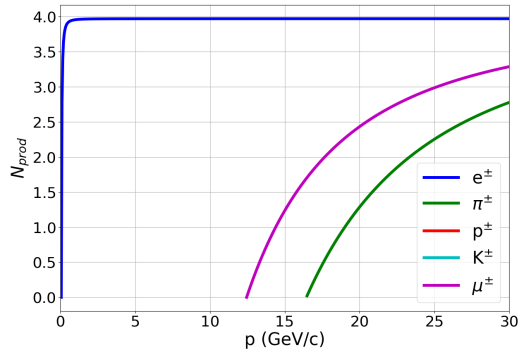

(f) He

Figure 46: Number of photons produced in the visible spectrum for different charged particles per meter through different mediums as function of the particle momentum.

A side-view of a particle traveling through a medium whilst radiating photons at a Cherenkov angle θ_{ch} along its track, as well as the photons arriving at a plane where the detections of said photons could take place, is given in Fig. 47. Due to the low amount of photons produced per meter of gas compared to solid media like aerogel, ring reconstruction is possible when focusing mirrors are used to retrieve the ring structure. In the case of a gas, a "blob" of photons arrives at a photon detection plane, as can be seen in the top-view of the figure.

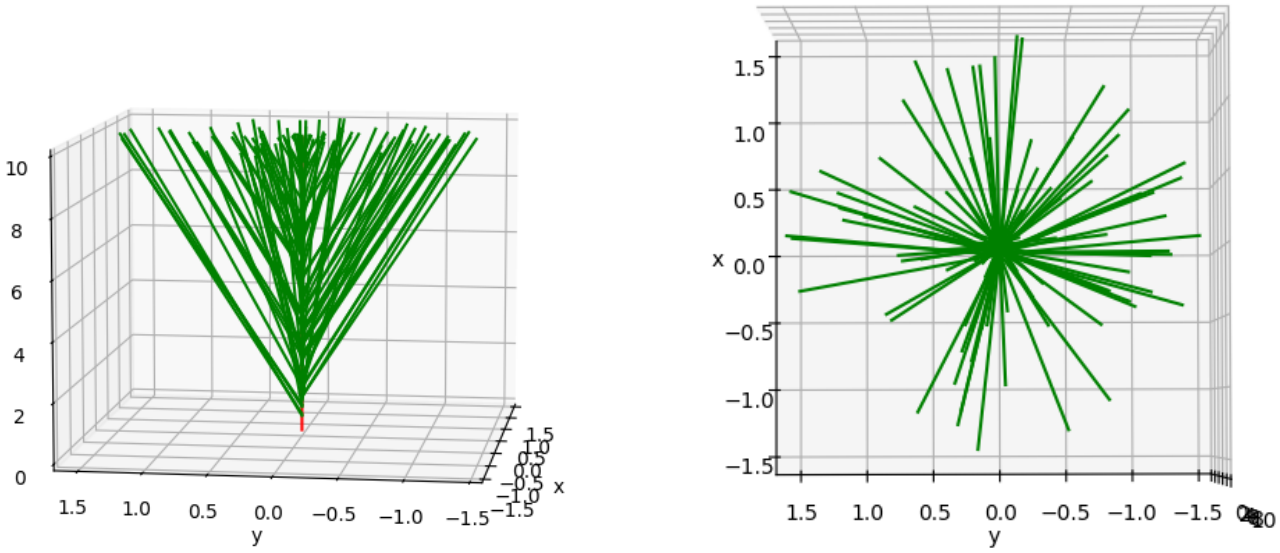

(a) Side view

(b) Top view

Figure 47: A charged particle (red) travels through a transparent gas and emits photons (green) along its track.

Later, it will be shown that focusing mirrors are needed to provide both ring reconstruction to increase the performance and to prevent significant irradiation to the silicon photon multipliers (SiPM). The shortcut based on the presence of photons is used to serve as a baseline of what can be achieved with a Cherenkov detector.

6.5.1 Experimental setup

To provide the parameters to distinguish electrons from charged particles, the FCT will be used to determine the momentum of the charged particle and a grid of SiPMs will be used to count the number of radiated photons that are incident on the detection plane. A schematic overview of a Cherenkov detector behind the FCT is given in Fig. 48. The Cherenkov detector consists of a radiation chamber filled with a transparent gas, helium in this case, and a plane with SiPMs to detect incident photons. In the figure, a charged particle is incident on the FCT and when it arrives in the radiation chamber, photons are emitted along the length of its track. The charged particle also creates photons when interacting with the material of the FCT, but these photons are outside of the sensitive range of the SiPMs and are therefore not counted as background. The SiPMs simulated were of the size ranging from 3 mm × 3 mm. To count the number of photons a charged particle emits, a circle[18] is drawn around the position of the charged particle on the photon detection plane and the number of photons inside is counted. A schematic overview of this is given in Fig. 49. In the figure, a charged particle (blue) is incident on a grid of SiPMs. Photons are emitted along the track of the particle (green) and end up in a cell of the grid. Both charged particles and photons have a chance to create a "hit" in the SiPM (purple). Around the position of the charged particle in the grid a circle is drawn (red) which indicates the so-called "check area", and all the hits from SiPMs within that range are counted. SiPMs are noisy and have a chance to create a hit even though there was no photon detected. This is called a dark count (black), and the rate at which this happens is called the dark count rate (DCR)

[18]Technically, this should be an ellipse, but a circle is a good approximation

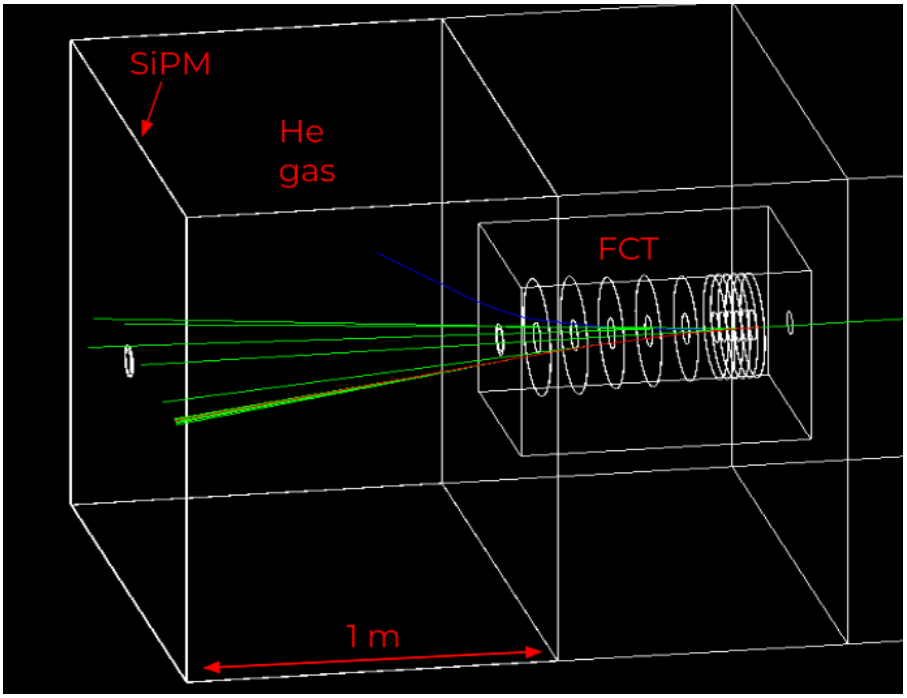

Figure 48: Schematic overview of a Cherenkov detector behind the FCT. An incident charged particle (red) radiates photons (green) in the Helium gas chamber.

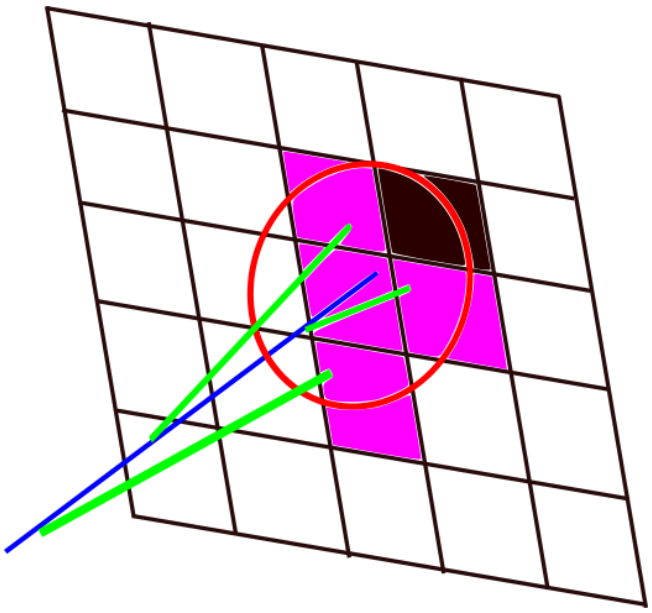

Figure 49: A schematic overview of the detection principle of a gas Cherenkov detector with SiPMs to detect photons.

which is given in MHz/mm. MHz/mm is a high order of magnitude, but SiPMs used in high radiation environments like at a LHC experiment get heavily irradiated and their DCR increases significantly. In the figure, 5 hits are counted within the check area.

6.5.2 Silicon photon multipliers (SiPMs)

The SiPMs simulated in this thesis are the Hamamatsu S13360-3050CS & S13360-3075CS [54] and FBK [55]. These SiPMs are sensitive to (near-) visible light[19], but their sensitivity is not uniform. In Fig. 50 the detection probability as function of the wavelength is given for the Hamamatsu S13360-3050CS. This detection efficiency is achieved at a low overvoltage where the probability of crosstalk is in the order of a few percent. The sensitive area of a SiPM comes with a fill factor (FF) which

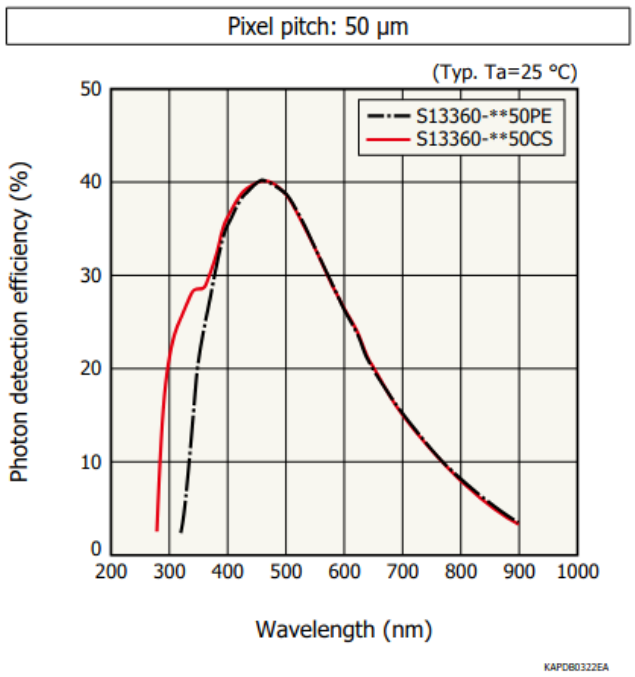

Figure 50: Photon detection efficiency of the Hamamatsu S13360-3050CS [54].

expresses the ratio of photosensitive area to total detector area. In addition, SiPMs have a casing which surrounds the photosensitive area for protection. For these studies, it is assumed that a smart placing of these individual modules reduces the influence of the dead zone between the photosensitive areas induced by this casing to be negligible. A study on the expected DCR of LHC-environment irradiated SiPMs is done in the scoping document [32]. Tab. 13 gives an overview of the parameters of the SiPMs simulated in this study.

SiPM	Wavelength sensitive range (nm)	DCR (MHz/mm)	Fill factor	Side length (mm)
Hamamatsu 3050CS [54]	[895, 274]	1	0.74	3
Hamamatsu 3075CS [54]	[898, 275]	1	0.82	3
FBK 3V [55]	[700, 284]	0.7	0.82	3

Table 13: Specific parameter values for different SiPMs.

[19] Visible light ranges from [380, 700] nm.

6.5.3 The simulation

To simulate the performance of the aforementioned setup, for each event, the charged particles that arrive at the last layer of the FCT are requested. For each charged particle, the following steps are performed:

- Calculate the expected number of photons emitted in the sensitive range of the SiPM with Frank-Tamm theory, $\langle N_\gamma \rangle$.
- Randomly draw the number of emitted photons from a Poisson distribution with $\mu = \langle N_\gamma \rangle$.
- Calculate the position where the charged particle will end up on the SiPM grid and in which SiPM.

Then, for each photon

- Randomly draw its energy from a $1/\lambda^2$ distribution.
- Randomly select the azimuthal angle between $[0, 2\pi]$ and calculate its direction by rotating it around the charged particle using the Rodrigues' rotation[20] [56], [57].
- Randomly place the starting position of the photon on the track of the charged particle.
- Calculate the position where the photon will end up on the SiPM grid and in which SiPM.

For each photon or charged particle that ends up on the SiPM grid in a specific SiPM

- If it is a charged particle, check if it is in the active area of the SiPM based on the fill factor.
  - If yes: A hit was registered in that SiPM.
  - If no: No hit was registered in that SiPM.
- If it is a photon, check if this photon is in the active area of the SiPM based on the fill factor.
  - If yes: Randomly decide whether the photon registered a hit in that SiPM based on the photon detection efficiency of the SiPM.
  - If no: No hit was registered in that SiPM.

Then, for each charged particle,

- Calculate the radius of the check area around the charged particle based on the radiator length L, such that $r_{\text{check area}} = L \tan(\theta_{\text{ch}})$.
- Count the number of SiPMs that registered a hit either from a photon or the charged particle. This is N_{Hits}.
- Account for overlapping hits in SiPMs and reduce N_{Hits} accordingly. The SiPMs are used with a binary readout, so a SiPM can only detect one hit even if there are multiple photons or charged particles are present in the same SiPM.
- Count the number of SiPMs inside the check area.
- Subtract from that the number of SiPMs that already registered a hit as result from a photon or charged particle to get N_{SiPM}.
- Based on the ROF, the DCR and the photosensitive area of the SiPM, calculate the expected number of SiPMs that would register a dark count, $\langle N_{\text{DC}} \rangle = N_{\text{SiPM}} \times \text{DCR} \times \text{ROF} \times A_{\text{SiPM}}$.
- Randomly draw the number of dark counts from a Poisson distribution with $\mu = \langle N_{\text{DC}} \rangle$.
- Add this to N_{Hits}. To sum up, $N_{\text{Hits}} = N_{\text{Detected photons}} + N_{\text{Dark Counts}} + N_{\text{Detected charged particles}}$.

Electron hypothesis decision table	$p < p_{\text{th. }\pi}$	$p > p_{\text{th. }\pi}$
$N_{\text{Hits}} < N_{\text{Hits th.}}$	Not electron	Not electron
$N_{\text{Hits}} \geq N_{\text{Hits th.}}$	Electron	Not electron

Table 14: Electron hypothesis decision table

A decision based on the number of hits registered in the check area of each charged particle and the momentum of the charged particle is made. The decision table is given in Tab. 14. Each event is vetoed based on whether that event contains an electron based on the decision table. Along with the SiPMs that come with their own parameters, summarized in Tab. 13 and the medium of the Cherenkov detector, these other parameters are varied:

- The radiator length L of the Cherenkov detector. This was allowed to vary between 1 and 2 meters due to space restrictions induced by the FOCAL.
- The read-out-frame (ROF). Either 2 (ideal scenario) or 20 ns (worst case scenario).
- The threshold number of hits that are needed inside the check area of a charged particle for this charged particle to be guessed an electron, $N_{\text{Hits th.}}$.

6.5.4 Optimization of the radiator length

To get an idea what the optimal radiator length of such a Cherenkov detector would look like, a rough optimization can be done. The idea is to optimize the difference in number of expected photons that get detected and the expected number of dark counts that get detected. This way, the distinguishing power of whether a charged particle is an electron based on the number of hits is expected to grow. To come to this optimization, it is first needed to consider the average number of photons produced when a charged particle traverses through a transparent medium which is given by Frank-Tamm theory55, which can be written down as $\langle N_\gamma \rangle = F_T \times L$, where L is the radiator length. The photon detection efficiency (PDE) of a SiPM is a function of the wavelength of the incident photon. The photons are emitted with a wavelength that is drawn from the probability density function (PDF) $1/\lambda^2$. So, the average photon detection efficiency (APDE)[21] of a photon drawn from that PDF would be

$$\text{APDE} = \frac{\sum(\text{PDF} \times \text{PDE})}{\sum \text{PDF}}. \tag{56}$$

Since SiPMs have a photosensitive area defined by their fill factor (FF), the effective PDE would be EPDE = FF × APDE. So, the expected number of detected photons is

$$\langle N_{\gamma\text{Det.}} \rangle = F_T \times \text{EPDE} \times L = aL. \tag{57}$$

The expected number of dark counts per SiPM per ROF is

$$\langle N_{\text{DC/SiPM}} \rangle = \text{DCR} \times \text{ROF} \times A_{\text{SiPM}}. \tag{58}$$

The expected number of detected dark counts is

$$\langle N_{\text{DC Det.}} \rangle = N_{\text{SiPM}} \times \langle N_{\text{DC/SiPM}} \rangle, \tag{59}$$

where N_{SiPM} is the number of SiPMs in a check area around a charged particle. The number of SiPMs per check area is given by $N_{\text{SiPM}} = A_{\text{c}}/A_{\text{SiPM}}$, where A_{c} is the check area given by $\pi\, r_{\text{c}}^2$. The check

[20] Not to be confused with the Euler-Rodrigues formula for 3D rotation.
[21] which is a number through the sum

radius, r_c, in its turn can be written as $L \tan \theta_{ch}$. This then allows the expected number of dark counts in a check area to be rewritten as

$$\langle N_{\text{DC Det.}} \rangle = \frac{\pi L^2 \tan^2 \theta_{ch}}{A_{\text{SiPM}}} \langle N_{\text{DC/SiPM}} \rangle = bL^2. \tag{60}$$

Then writing the aforementioned relations as the number of signal counts ($f(L)$) after subtraction of the expected background (bL^2) from the expected number of signal photons (aL) gives

$$f(L) = aL - bL^2. \tag{61}$$

To optimize the number of signal counts after the expected background subtraction to enhance the distinguishing power, the maximum of this formula is computed by taking the derivative and setting the result to 0, which gives

$$L = \frac{a}{2b}. \tag{62}$$

Of course, there is the term that depends on the charged particle as well, which would introduce a term $-c$ in the equation, but since this does not depend on L, the derivative remains the same. Writing the equation fully out again for the terms a and b, and integrating over the energy range of the photon from Frank-Tamm theory, gives

$$L = \frac{a}{2b} = \frac{\alpha}{\hbar c \pi} Z^2 \frac{(E_{\gamma 2} - E_{\gamma 1}) \times \text{EPDE}}{\text{DCR} \times \text{ROF}} \frac{\sin^2 \theta_{ch}}{\tan^2 \theta_{ch}}, \tag{63}$$

where all terms are either constants, or depend on the SiPMs specific, except for the Cherenkov angle θ_{ch}, but $\sin^2 \theta_{ch} / \tan^2 \theta_{ch} \approx 1$ when $\theta_{ch} \ll 1$, which is the case for these charged particles. In this optimization scheme, the effect of photons and dark counts occupying the same SiPM is not taken into account, but as will be shown below, the scheme is still effective.

6.5.5 Comparing the calculation and simulation

Tab. 15 shows the parameters for which the Cherenkov detector setup was simulated, making 36 sets in total.

Simulation settings Hamamatsu 3050cs	**Sim 1**	**Sim 2**	**Sim 3**	**Sim 4**	**Sim 5**	**Sim 6**
Gas	He	He	He	He	He	
Radiator length	1 m	1 m	1.8 m	1.8 m	1 m	
Photon hit threshold	2	3	2	3	2	
Read out frame	2 ns	2 ns	2 ns	2 ns	20 ns	
Simulation settings Hamamatsu 3075cs	**Sim 1**	**Sim 2**	**Sim 3**	**Sim 4**	**Sim 5**	**Sim 6**
Gas	He	He	He	He	He	He
Radiator length	1 m	1 m	2.45 m	2.45 m	2.45 m	1 m
Photon hit threshold	2	3	2	3	6	2
Read out frame	2 ns	2 ns	2 ns	2 ns	2 ns	20 ns
Simulation settings FBK 3V	**Sim 1**	**Sim 2**	**Sim 3**	**Sim 4**	**Sim 5**	**Sim 6**
Gas	He	He	He	He	He	He
Radiator length	1 m	1 m	2.98 m	2.98 m	2.98 m	1 m
Photon hit threshold	2	3	2	3	7	2
Read out frame	2 ns	2 ns	2 ns	2 ns	2 ns	20 ns
Simulation settings Hamamatsu 3050cs	**Sim 1**	**Sim 2**	**Sim 3**	**Sim 4**	**Sim 5**	
Gas	Ne	Ne	Ne	Ne	Ne	
Radiator length	1 m	1 m	1.8 m	1.8 m	1 m	
Photon hit threshold	2	3	3	4	2	
Read out frame	2 ns	2 ns	2 ns	2 ns	20 ns	
Simulation settings Hamamatsu 3075cs	**Sim 1**	**Sim 2**	**Sim 3**	**Sim 4**	**Sim 5**	**Sim 6**
Gas	Ne	Ne	Ne	Ne	Ne	Ne
Radiator length	1 m	1 m	2.45 m	2.45 m	2.45 m	2.45 m
Photon hit threshold	2	3	7	8	9	10
Read out frame	2 ns	2 ns	2 ns	2 ns	2 ns	2 ns
Simulation settings FBK 3V	**Sim 1**	**Sim 2**	**Sim 3**	**Sim 4**	**Sim 5**	**Sim 6**
Gas	Ne	Ne	Ne	Ne	Ne	Ne
Radiator length	1 m	1 m	2.98 m	2.98 m	2.98 m	0.298 m
Photon hit threshold	2	3	8	9	10	10
Read out frame	2 ns	2 ns	2 ns	2 ns	2 ns	20 ns

Table 15: Simulation settings for the use of different SiPMs, gases and radiator length of the FCT RICH.

In Tab. 16, some of the values discussed in the previous sections are calculated based on the input parameters and compared to the values retrieved from the simulations for three sets. The calculated values of a Cherenkov detector with a radiator length of 1 m is compared to the case when the radiator length is optimized according to the scheme as described in the previous section. The best performing two cases, in terms of significance and amount of signal remaining, for helium and neon are presented here. The performance of these sets will be discussed below as well. The results for these sets, i.e. the photon spectrum after the application of the veto and the significance, is presented in Sec. 6.5.6.
What becomes clear is that the number of photons detected per electron for which its momentum[22]

[22]In this paragraph, the momentum of any particle discussed satisfies this criteria unless specified otherwise.

Value \ Simulation setting	3050cs He Sim 1		3075cs He Sim 4		3075cs Ne Sim 4	
For electrons that satisfy $p_{\pi\text{ th.}} > p > p_{\text{e th.}}$	**Calc.**	**Sim.**	**Calc.**	**Sim.**	**Calc.**	**Sim.**
N_γ emitted	8.1	8.1	19.8	19.8	36.0	36.0
N_γ detected (no overlap)	1.6	-	5.3	-	9.9	-
Ratio of photons detected (no overlap)	0.196	0.196	0.266	0.266	0.273	0.273
Number of photons detected (including overlap)	-	1.3	-	4.5	-	8.4
Ratio of photons within check area	-	0.95	-	0.97	-	0.97
Check area (mm^2)	220	220	1319	1319	2374	2374
N_{SiPM} in check area	24.4	23.1	147	134	264	255
N_{DC} in check area	0.44	0.38	2.64	2.33	4.7	4.4
Ratio of detected electrons	0.74	0.69	0.82	0.57	0.82	0.49
N_{Hits}	2.8	2.2	8.7	7.4	15.1	13.2
For charged particles that satisfy $p_{\pi\text{ th.}} > p > p_{\text{e th.}}$	**Calc.**	**Sim.**	**Calc.**	**Sim.**	**Calc.**	**Sim.**
N_{DC} in check area	0.44	0.43	2.64	2.60	4.7	4.7
Ratio of detected charged particles	0.74	0.74	0.82	0.82	0.82	0.82
N_{Hits}	1.2	1.2	3.5	3.4	5.5	5.5

Table 16: Comparison between the calculation of certain values and the average as retrieved from the simulation.

satisfies $p_{\pi\text{ th.}} > p > p_{\text{e th.}}$ is less in the simulation. This is caused by a number of effects which will be discussed now. Since the SiPMs are arranged in a grid, the check area only considers a SiPM to be within the check area if its center lies within the check area. This was done to minimize the effect of dark counts of SiPMs for which only a small percentage of the total area lies within the check area. This causes some photons that were emitted within the check area and technically detected by a SiPM to not count towards the total N_{Hits}. Additionally, a circular check area is not the right shape since the charged particles are incident on the SiPM grid with a (small) angle. This causes the ratio of photons to be within the check area to range from ≈ 0.93–0.97. Photons can occupy the same SiPM and since photons can be emitted with equal probability along the track of the electron, the likelihood that a bin is occupied by more than one photon increases closer to the center of the check area. These contributions all cause the number of detected photons in the simulation (so including overlap) to be less than what is predicted through the calculation. The ratio of detected photons if there was no binary readout of the SiPMs (so no overlap) is the same for the simulation as what is calculated. In the simulation, the number of photons detected, charged particles that cause a SiPM to report a hit and number of dark counts that is detected are dependent on the order in which they are simulated. In a real scenario, these numbers all together form the number of total hits detected and cannot be distinguished from each other as can be done in the simulation due to the binary read out of the SiPM. In this simulation, the order of simulation was as follows

- Generate photons
- Detect photons and save N_γ detected.
- Emit charged particle and check if it would occupy a SiPM that is already occupied by a photon. Count the "detected" charged particle and treat it as a "photon" hit in the SiPM grid.
- From the number of SiPMs within the check area, subtract those that already detected a hit (i.e. N_γ detected) and randomly select which of the remaining SiPMs register a dark count.

Had the order been different, the numbers would have varied, but the total number of hits, N_{Hits}, would have remained the same. In the simulation, a charged particle caused the SiPM to read out a hit if the charged particle was within the active area of the SiPM, which is equal to $1 - FF$. Charged particles (not electrons), due to the fact that they do not emit photons in this momentum range, do not suffer from the overlap of photons and the charged particle ending up in the same SiPM, which can be seen in the table by the fact that the calculated ratio of "detected charged particles" is equal to the one simulated. For electrons, however, since they do emit photons in this momentum range, this overlap reduces the ratio of "detected electrons". An alternative explanation for this ratio is "the ratio of electrons/charged particles" that caused a binary read out of the SiPM. Since the generation of dark counts is last, the number of SiPMs that have not detected a photon yet are used to generate the number of dark counts. This causes the value in the table to be less than what is expected based on the number of SiPMs in a check area. For the simulations with a radiator length optimized based on the scheme described above, the difference in number of hits caused by photons and dark counts & the charged particle is larger than when a detector of 1 m was used, which increases the distinguishing power between electrons and charged particles. Since the values retrieved from the simulation are similar to those from the calculation, it is expected that the radiator length is close to its optimum and consequently further optimization through a scheme that incorporates the overlap of hits as discussed above will only yield minor improvements.

Comparing the ratio of vetoed events to the number of events that satisfy the veto in Tab. 17, i.e. the events that should be vetoed had the detector been perfect, it becomes clear that a strict veto is applied for these events. This is, however, necessary considering only $\approx 10\%$ of the events should be accepted.

Performance parameter		**Simulation setting**		
		3050cs He Sim 1	**3075cs He Sim 4**	**3075cs Ne Sim 4**
Formula	**Description**			
$N_{\text{Vetoed}}/N_{\text{Events}}$	Ratio of vetoed events	0.942	0.981	0.935
$N_{\text{Sat. veto}}/N_{\text{Events}}$	Ratio of events that satisfy veto criteria	0.904	0.904	0.904
$N_{\text{Cor. vetoed}}/N_{\text{Sat. veto}}$	Ratio of correctly vetoed events	0.983	0.999	0.994
$N_{\text{Cor. acc.}}/(N_{\text{events}} - N_{\text{Sat. veto}})$	Ratio of correctly accepted events	0.444	0.188	0.291
$N_{\text{Incor. vetoed}}/N_{\text{Vetoed}}$	Ratio of incorrectly vetoed events	0.057	0.080	0.040
$N_{\text{Incor. acc.}}/N_{\text{Accepted}}$	Ratio of incorrectly accepted events	0.265	0.049	0.090
For electrons that satisfy $p_{\pi\text{ th.}} > p > p_{\text{e th.}}$				
$N_{\text{Cor. guessed}}/N_{\text{Electrons}}$	Ratio of correctly guessed electrons	0.691	0.959	0.937
$N_{\text{Incor. guessed}}/N_{\text{Electrons}}$	Ratio of incorrectly guessed electrons	0.309	0.041	0.063
For charged particles that satisfy $p_{\pi\text{ th.}} > p > p_{\text{e th.}}$				
$N_{\text{Cor. guessed}}/N_{\text{Charged particles}}$	Ratio of correctly guessed charged part.	0.723	0.313	0.819
$N_{\text{Incor. guessed}}/N_{\text{Charged particles}}$	Ratio of incorrectly guessed charged part.	0.277	0.687	0.181

Table 17: Performance parameters for 3 highlighted Cherenkov detector simulations.

The 3075cs He Sim 4 settings applied the strictest veto, accepting only 2% of the events. It correctly vetoed 99.9% of the events that should be vetoed and in doing so, it retained 18.8% of the events that should be accepted. Its strictness is also reflected in the ratio of electrons it guesses correctly and the ratio of charged particles it mistakes for electrons. This results in the ratio of incorrectly accepted events to be 4.9% being rather low, or in other words, $\approx 1/20$ events is an incorrectly accepted event. This set is much better in guessing electrons than the set with the radiator length of 1 m and in doing so retains relatively pure data post veto. In comparison, the data purity for the simulation setting of 3075cs Ne Sim 4 is lower, but the amount of events retained post veto is a factor ~ 3.4 higher. Even though this set is better at recognizing charged particles, it takes a hit in electron identification, resulting in a less pure data set; $\approx 1/11$ events is an incorrectly accepted event. From this table it becomes clear that the optimization scheme as described in the previous section provides the detector with greater distinguishing power and increases the purity of the data post veto significantly. Sec. 6.5.6 shows the photon spectra and significance for these simulation settings, but the Appendix shows the full list of spectra from which a few more trends can be extracted with respect to the simulation settings. These will also be discussed in Sec. 6.5.6.

6.5.6 Results

Fig. 51 shows a selection of the spectra (left column) and significance (right column) from the simulations with the Cherenkov detector behind the FCT.

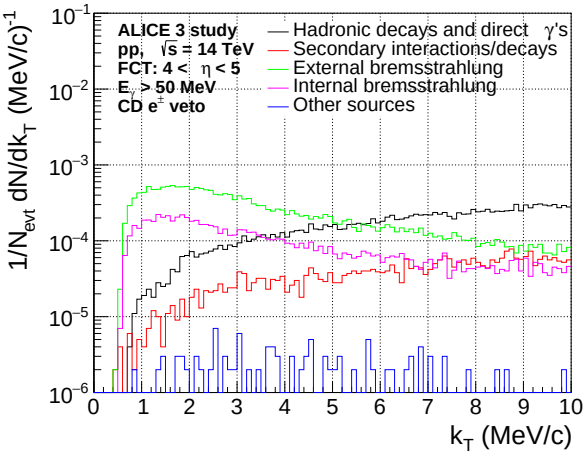

(a) Hamamatsu 3050cs SiPM's, $L = 1\,\text{m}$, helium gas, $N_{\text{Hits th.}} = 2$.

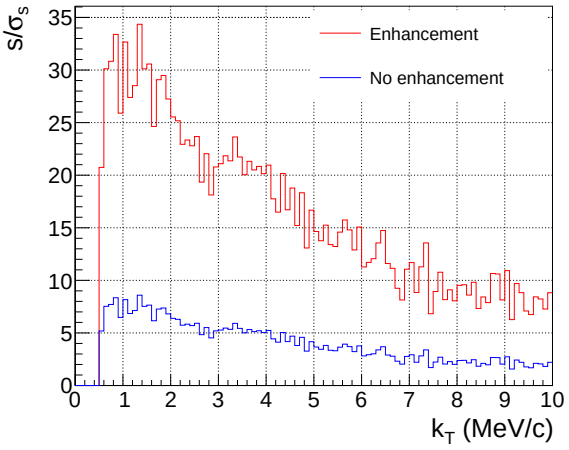

(b) Significance of Fig. 51a.

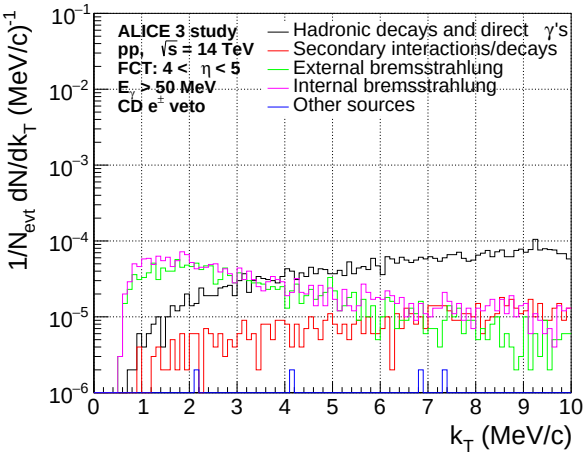

(c) Hamamatsu 3075cs SiPM's, $L = 2.45\,\text{m}$, helium gas, $N_{\text{Hits th.}} = 3$.

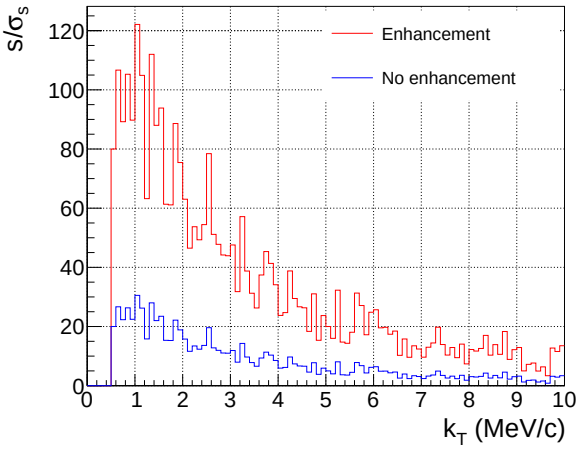

(d) Significance of Fig. 51c.

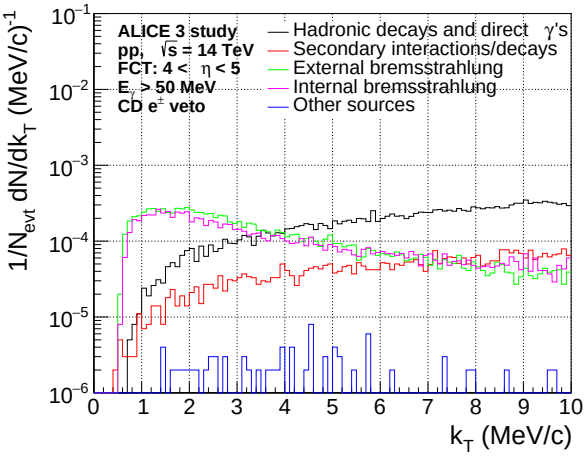

(e) Hamamatsu 3075cs SiPM's, $L = 2.45\,\text{m}$, neon gas, $N_{\text{Hits th.}} = 8$.

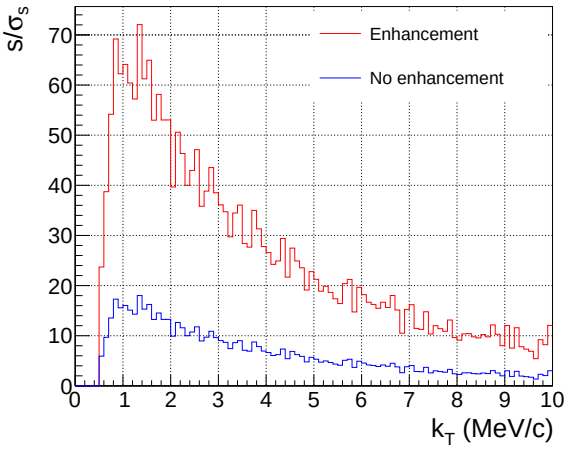

(f) Significance of Fig. 51e.

Figure 51: Photon spectrum after the e^+e^- event veto with a Cherenkov detector behind the FCT for a small selection of the simulation parameters (left column). Significance (right column) assuming 5% uncertainty on the background.

Due to the purity of the events in Fig. 51c, the significance is the most promising for these simulation settings, but due to the low acceptance rate of events, the impact of statistical fluctuations

is also much higher for these number of simulated events. Following the conclusion reached from the previous section, the purity of the events is lower in Fig. 51e, but the amount of events retained is considerably higher. Like in previous sections the uncertainty on the background is assumed to be 5%. In these figures, the spectrum from "Other sources" (blue) includes that of "positron annihilation" and "hadronic inelastic interactions" since they contribute negligibly to the whole spectrum.

Figs. 63, 64 and 65 in the Appendix (Sec. 11) show the full list of all spectra retrieved from the simulations of the Cherenkov detector done with the settings as described in Tab. 15.

6.5.7 Considerations - A Ring Imaging Cherenkov detector

The DCR of the SiPMs used for the simulations in this thesis was in the order of 1 MHz, which is a lot compared to the reported value by Hamamatsu [54] and FBK [55]. These are the estimates for operation in the high radiation zone that is the ALICE 3 experiment. In a high radiation zone, these SiPMs become irradiated, causing their DCR to drastically increase. The values used in this thesis come from the upcoming Scoping Document [32]. These values were estimated for the RICH and fRICH, but since the FCT will be operational in the more forward pseudorapidity range of $4 < \eta < 5$, the SiPM that would be used for the FCT RICH would experience a higher radiation dosage causing the values for the DCR to be underestimated. To mitigate this, focusing mirrors could be used to reflect and focus the Cherenkov radiation away from the pseudorapidity range of the FCT and onto a grid of SiPMs that is positioned in the radiation zone of the fRICH. An example of a design can be found when looking at the dual-radiator Ring Imaging Cherenkov detector (dRICH) [58] of the proposed Electron-Ion Collider (EIC) [59] at Brookhaven National Lab in the US. Fig. 52 shows the dRICH design of the EIC. As the name suggests, the dual-RICH makes use of two media to create Cherenkov

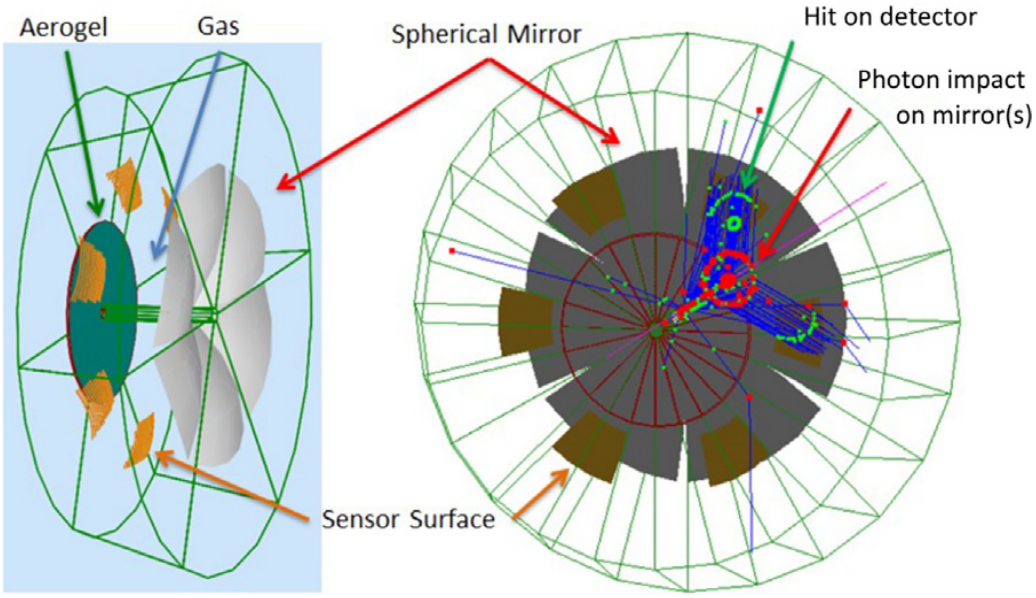

Figure 52: Design of the dRICH of the EIC. Figure taken from Ref. [58].

radiation: Aerogel and C_2F_6 gas with $n = 1.02$ and $n = 1.00085$, respectively[23] to achieve the electron/hadron separation needed for its physics program. In this design, the photo sensors are located outside of the acceptance of the dRICH. The spherical mirrors focus the Cherenkov radiation onto the photo sensors and through this focusing, ring reconstruction becomes available again. However, the design and optimization of the detector was, as reported in Ref. [60], a daunting task. Through the use of a AI-driven optimization based on Bayesian Optimization (BO), a parameter space with 8 parameters and $\mathcal{O}(10^{22})$ possibilities[24] was explored to optimize the PID capabilities of the detector. Even considering a design for the FCT where spherical mirrors are included, but ring reconstruction

[23] Some presentations mention $n = 1.0008$ for the gas.
[24] Based on the tolerances of Tab. 1 reported in Ref. [60].

is not possible, the spherical mirrors would focus the Cherenkov radiation on a smaller photo sensitive surface than what is currently used for the FCT. If the same amount of photons are radiated on a smaller photo sensitive surface, the contribution of dark counts goes down as shown in the previous sections, which in turn enhances the distinguishing power between electrons and hadrons. Through this fact alone, the performance of the FCT RICH is expected to increase, or at the very least stay the same as reported in the previous section if focusing mirrors are incorporated in the design.

If, however, similar PID capabilities of the dRICH can be achieved with the FCT RICH, the performance of the e^+e^- event veto is expected to increase significantly. The dRICH is reported to achieve electron/hadron separation up to $\sim 18\,\mathrm{GeV}/c$ with at least 3σ, see Ref. [59], which is more than sufficient for the purposes of the FCT.

7 Background uncertainty estimation

The determination of the uncertainty on the background is of vital importance to the measurements presented in this thesis, a first step towards the estimation of which will be covered in this section.

7.1 External bremsstrahlung and secondary interactions/decays

ALICE 1 [61–63] estimated the systematic uncertainty of photon spectrum measurements related to the material budget to be 4.5% [62, 64]. This was done by comparing the reconstructed number of photon conversions normalized to the number of charged particles between Monte Carlo (MC) simulations and the real data. To this end, precise knowledge of the material budget is key to reducing the aforementioned uncertainty. In ALICE 3 for the FCT, the dominant contribution to the material budget comes from the beam pipe, see Fig. 19. The beam pipe is also the dominant source of external bremsstrahlung and secondary decays/interactions, 47%, as shown in Fig. 34. The beam pipe will be a regular, symmetric structure that can be accurately resembled by a cylinder with a certain thickness of a certain material, 0.8 mm of beryllium as assumed in this thesis. In the production process, it can be weighed and x-ray scanned to give a precise estimation of the uncertainty of its material budget. The welding of the beam pipe in the places where it needs to be connected to other structures increases the material budget slightly, but this can also be scanned. The contribution of the uncertainty on the material budget of the beam pipe is thus expected to be small compared to the rest of the structures in front of the FCT. The second most contributing structure to the material budget is the IRIS tracker, and consequently it is the second most biggest source of external bremsstrahlung and secondary decays/interactions, 18%. Unfortunately, the same precision for the material budget is not expected for the IRIS tracker since it consists of many components (disks, petal cases, cold plate, services, etc.) which makes the whole structure asymmetric. In addition, as is often the case in (big) experiments, the exact placement of each service component does not get communicated equally well to the whole collaboration. The uncertainty of the material budget is therefore expected to be much bigger of the IRIS tracker than of the beam pipe. Fortunately, ALICE 3 has the advantage that the IRIS tracker is retractable and in the retracted state, as can be seen in Fig. 18, no material of the IRIS tracker is expected in the pseudorapidty range of $4 < \eta < 5$. This claim is strengthened by the fact that the aperture of the beam pipe is required to be 16 mm at beam injection, and unless the wish is to create a fixed target experiment, no parts of the services of the IRIS tracker will be inside this radius when the IRIS tracker is in the retracted state. This retractability can be exploited to perform measurements of the photon spectrum when the IRIS tracker is in the retracted state and when it is in the contracted state. These spectra and the difference of these spectra can then be compared to spectra and difference retrieved from MC simulations to isolate the contribution of the IRIS tracker to the photon spectra. The aforementioned spectra and the difference in spectra retrieved from the MC simulations performed for this thesis, simulation sets "Default ALICE 3" and "IRIS Opened", are given in Fig. 53. A cut on the pointing angle was not applied for these spectra as it is unknown what the primary vertex position resolution of the IRIS tracker is when it is in the retracted position. Fig. 19 shows that the outer tracker disks contribute a similar amount to the material budget as the IRIS tracker, however, with the inclusion of the cut on the pointing angle and the cut on the distance to the closest charged particle, Fig. 34, the fraction of photons that are mistaken to come from the primary vertex is not 1:1 related to its contribution to the material budget. The uncertainty on the material budget of the outer tracker is therefore also expected to be of lesser importance to the uncertainty on the measured photon spectrum. Assuming similar results for the FCT to Ref. [62, 64], an uncertainty of 5% on the external bremsstrahlung and secondary interactions/decays spectra could be achieved. Considering the beam pipe will be a very regular piece of material and a measurement of the contribution of the IRIS tracker to the photon spectrum can be made thanks to its retractability, it might be possible to reduce the uncertainty on these channels, but more studies are required.

In Ref. [65], the ALICE Collaboration managed to bring the estimated systematic uncertainty related to the material budget of ALICE 1 down to 2.5%. They claim their methods to be generic and applicable to any experiment in similar fashion. Taking inspiration from their methods, the idea to

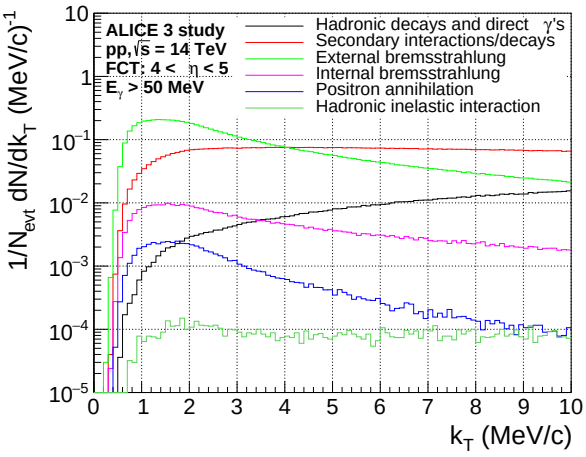

(a) The photon spectrum when the IRIS is in the retracted position.

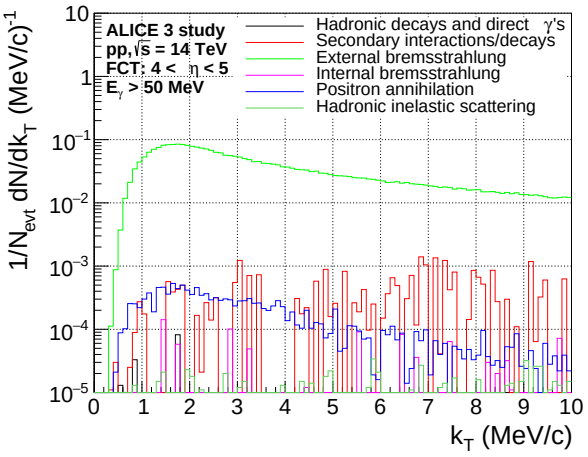

(b) The difference in photon spectrum between the IRIS in retracted and contracted position.

Figure 53: The photon spectrum to arrive at the FCT when the IRIS tracker is in the retracted position (left). The difference in the photon spectrum to arrive at the FCT between the IRIS in the contracted and retracted position (right).

reconstruct π^0's coming from secondary vertices could shine light on the material structures of the ALICE 3 geometries. As will be shown in Sec. 8, reconstructing low p_{T} π^0's coming from the primary vertex is possible, but the question is whether the position resolution of the FCT is good enough to accurately reconstruct the position of secondary π^0's created through material interactions in for example the IRIS tracker. As external bremsstrahlung is dominant, the fraction of combinatorial background could be much higher than what is presented in 8 for the reconstruction of the invariant mass of primary π^0's.

7.2 Hadronic decays and direct γ's

The hadronic decays and direct γ's spectrum is dominated by the decay of neutral pions, $\pi^0 \rightarrow \gamma\gamma$. To estimate the uncertainty on this spectrum, three strategies are laid out in this section.

Measure the π^0 spectrum with the FCT

In Sec. 8 it will be shown that the π^0 spectrum in the low p_T region can be measured. In the decay channel of $\pi^0 \rightarrow \gamma\gamma$, two photons are produced and since both need to be measured, the uncertainty on the background (external bremsstrahlung and secondary decays/interactions) induced by the material budget would enter twice in the uncertainty of measuring the photon spectrum from the decays of π^0's. Assuming that the systematic uncertainty related to the material budget for the measurement of the photon spectrum is 5%, the resulting uncertainty on the photon spectrum from primary π^0 decay would be 10%. As argued in the previous section, it could be possible to reduce this uncertainty and consequently reduce the uncertainty on the photon spectrum from primary π^0's.

Tune PYTHIA to the $\pi^{\pm}$ spectrum

Utilizing the capabilities of the other detectors of ALICE 3, the $\pi^{\pm}$ spectrum will be measured in the pseudorapidty region of $|\eta| < 4$ and the RICH, bRICH, TOF, fTOF and iTOF can provide particle identification for these charged pions. Due to the isospin symmetry, the number of charged pions that is produced in inelastic collisions is similar to half[25] of the number of neutral pions produced. Using a PYTHIA simulation the measured and predicted spectra can be related. Performing an extrapolation to the pseudorapidty region of the FCT, the π^0 spectrum could be predicted as well as the uncertainty on its contribution to the soft-photon spectrum through the decay to 2 photons.

[25] $N_{\pi^+} \sim N_{\pi^-} \sim N_{\pi^0}$

Extrapolate the higher p_T π^0 decay spectrum to lower regions

In the lower k_T region of the photon-spectrum to arrive at the FCT, the external bremsstrahlung spectrum dominates as shown countless of times in this thesis. To still get a value for the uncertainty on the hadronic decays and direct γ's channel an extrapolation of the neutral pion transverse momentum spectrum, $dN_{\pi^0}/dp_{\mathrm{T}}$, could be performed through a measurement of this spectrum at higher p_{T}. As will be shown in Sec. 8, the simulations performed in this thesis show that the FCT could measure the transverse momentum spectrum of the π^0's in the region where $p_{\mathrm{T}} > 10$–$20\,\mathrm{MeV}/c$. This could then be used to predict the neutral pion decay spectrum. Comparing the measured data of the photon spectrum with the predicted neutral pion decay spectrum in the transverse momentum regime where the hadronic decays and direct γ's channel starts to dominate the photon spectrum allows for a similar scaling of the predicted hadronic decay spectrum in the desired lower transverse momentum regime. The hadronic decays and direct γ's channel is dominated by the decays of $\pi^0 \rightarrow \gamma\gamma$ and other sources are expected to not contribute much. Fig. 54 shows the transverse momentum photon spectrum in the $k_{\mathrm{T}} < 100\,\mathrm{MeV}/c$ region. These figures show that the hadronic decays and direct γ's channel starts to dominate the photon spectrum to arrive at the FCT at $k_{\mathrm{T}} = 10$–$15\,\mathrm{MeV}/c$, depending on the cuts that are implemented. In the LoI [8], studies were performed for the momentum resolution up to $500\,\mathrm{MeV}/c$. In the transverse momentum range of $10 < k_{\mathrm{T}} < 20\,\mathrm{MeV}/c$ in the pseudorapidity region of $4 < \eta < 5$ the momentum of the photons ranges from $270 < k < 1500\,\mathrm{MeV}/c$. As discussed in Sec. 5.6, a Gaussian Sum Filter (GSF) is a promising method for low-momentum electron tracking. Ref. [52] presents good performance of electron tracking with ACTS with a transverse momentum distribution of $500\,\mathrm{MeV}/c$ to $100\,\mathrm{GeV}/c$ and therefore similar performance is expected for the FCT when a GSF is used for tracking in the lower transverse momentum regime.

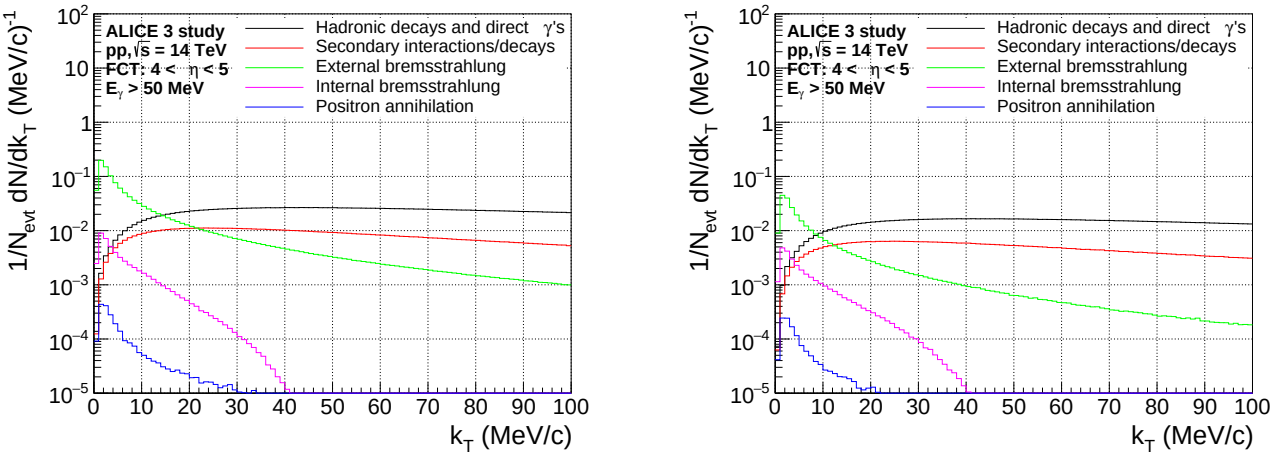

(a) Pointing angle cut applied.

(b) Pointing angle cut and cut on the distance to the closest charged particle, $d_{cq} < 2\,\mathrm{cm}$ applied.

Figure 54: The transverse momentum photon spectrum in the $k_{\mathrm{T}} < 100\,\mathrm{MeV}/c$ region.

8 Neutral pion reconstruction with the FCT

Due to the FCT's capabilities to measure low k_{T} photons in an acceptance unlike any other detector of ALICE 3, the FCT provides an unique opportunity to measure the π^0 invariant mass spectrum through the channel $\pi^0 \rightarrow \gamma\gamma$ and the transverse momentum spectrum down to low p_{T}. This is not only interesting to map out the uncertainty on the hadronic decay background as described in Sec. 7, but it also offers insights into some unique physics cases. In a recent paper a quantification of the excess of low transverse momentum pions was given when compared to fluid dynamics models for various heavy-ion collision systems at different LHC energies [66]. Measuring low transverse momentum pions remains an experimental challenge, but the proposed ALICE 3 detector will provide a new way to measure particles below $p_{\mathrm{T}} < 100\,\mathrm{MeV}/c$. Some of the potential sources of the excess of these low p_{T} pions are given in the paragraphs below. In Sec. 8.1 it will be shown that the the reconstruction of low p_{T} neutral pions works well for proton-proton collisions with the FCT. It is therefore most likely to be feasible in peripheral heavy-ion collisions and it might as well work in central heavy-ion collisions because of the significant difference in signal-to-background ratio of a measurement of the internal bremsstrahlung compared to the decay photon spectrum from neutral pions. In addition, the following sources of excess of low transverse momentum neutral pions that are postulated to exist in heavy-ion collisions were also searched for in hadron-hadron collisions, but not yet at a center-of-mass energy of $\sqrt{s} = 14\,\mathrm{TeV}$, and thus a clear motivation exists to pursue this measurement with the FCT in the pseudorapidty range of $4 < \eta < 5$.

According to Ref. [67], most of the hydrodynamic calculations used to successfully reproduce harmonic flow coefficients in the QGP, experience difficulties to predict the very low transverse momenta spectrum of pions. They postulate a possible onset of Bose-Einstein condensation at LHC energies which would increase the π^0 yield in lead-lead collisions in the very low transverse momentum regime, $p_T < 200\,\mathrm{MeV}/c$, compared to the full equilibrium model.

In the quark-gluon plasma (QGP), where chiral symmetry is restored at high temperatures, chiral condensates can form and potentially become disoriented where they are chirally rotated from their usual orientation in isospin space. The details of the formation of these regions are outside of the scope of this thesis, but two scenarios are highlighted as examples: the baked Alaska model [68] where a cooler interior in the QGP is isolated by a rapidly expanding shell of hot partons and through phase transition dynamics [69], [70] where the cooling of the QGP might cause the chiral field to settle in a non-equilibrium configuration as the system expands. These disoriented chiral condensates (DCC) are postulated regions of misaligned chiral symmetry breaking and their decay could lead to coherent emission of pions with an anomalous ratio of neutral to charged pions [71] in the low p_{T} region [72], amplifying the isospin asymmetry. The scenario where low p_{T} neutral pions dominate an event, called anti-Centauro [73] [74], would also be an interesting venue for the FCT to explore. An overview of the theoretical and experimental status can be found in [75].

8.1 Reconstruction results

Fig. 55 shows the reconstructed transverse momentum, p_{T}, as function of the rapidity of the π^0's where a clear hotspot can be seen for $p_{\mathrm{T}} < 1\,\mathrm{GeV}/c$. For this figure, the dataset "Default ALICE 3" was used. The π^0's were requested to have both of their photons in the FCT.

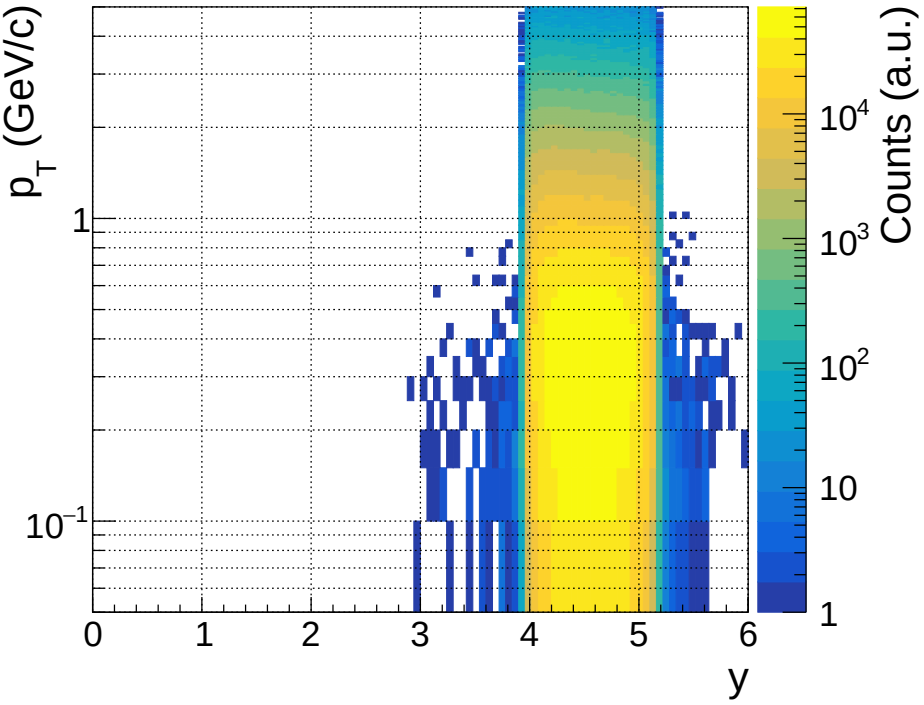

Figure 55: The transverse momentum of the π^0 as function of its rapidity.

Fig. 56 shows the π^0 invariant mass spectrum as function of its transverse momentum. The recipe of cuts and modification of the geometry of ALICE 3, as described in Sec. 6, have been applied to this spectrum as well to reduce the amount of photons before they were used to construct the spectrum. The photons were smeared before they were used to reconstruct the π^0 mass spectrum. The corresponding significances are given in Fig. 57.

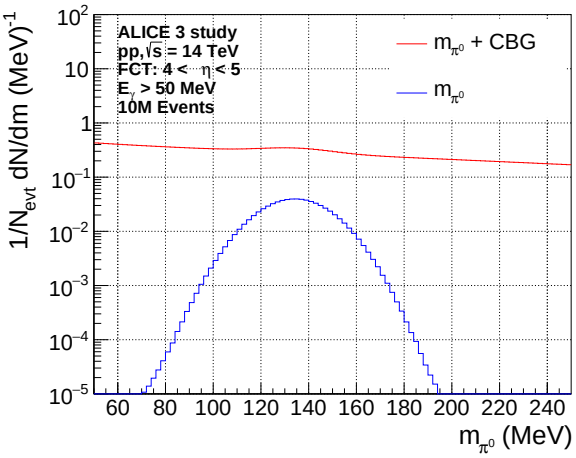

(a) π^0 mass spectrum without the application of any cuts or modification of the ALICE 3 setup.

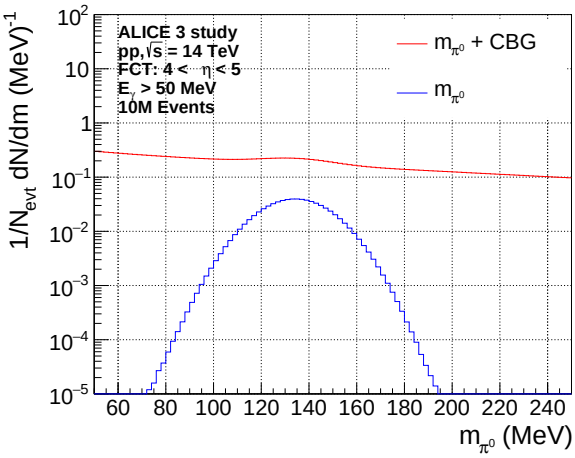

(b) π^0 mass spectrum with the application of the cut on the pointing angle.

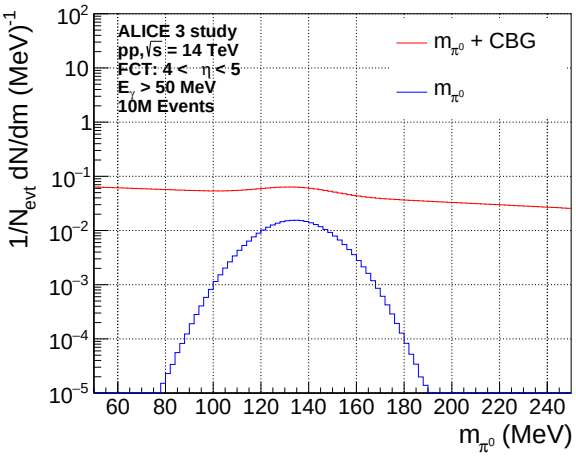

(c) π^0 mass spectrum with the application of the cut on the pointing angle and closest distance, $d_{cq} < 2\,\text{cm}$.

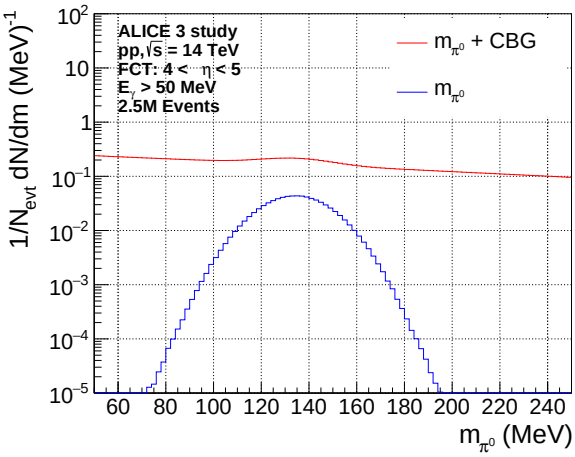

(d) π^0 mass spectrum for the ALICE 3 geometry with the window in the beam pipe and the cut on the pointing angle applied. For this figure, the dataset "Window 1" was used.

Figure 56: The π^0 mass spectrum including the application of cuts on the spectrum and the ALICE 3 geometry including a window in the beam pipe. The π^0 mass spectrum (blue) is the true π^0 mass spectrum without contamination of other sources. The other spectrum (red) shows the π^0 mass spectrum including the combinatorial background.

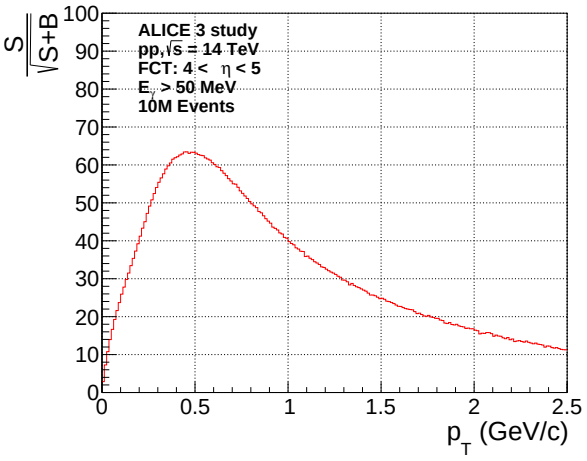

(a) No cuts applied.

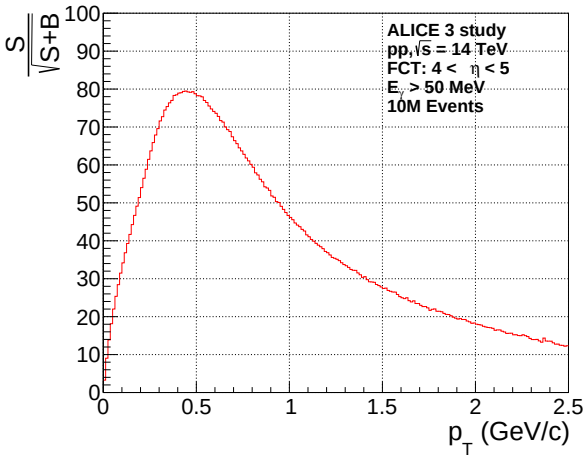

(b) Cut applied on the pointing angle.

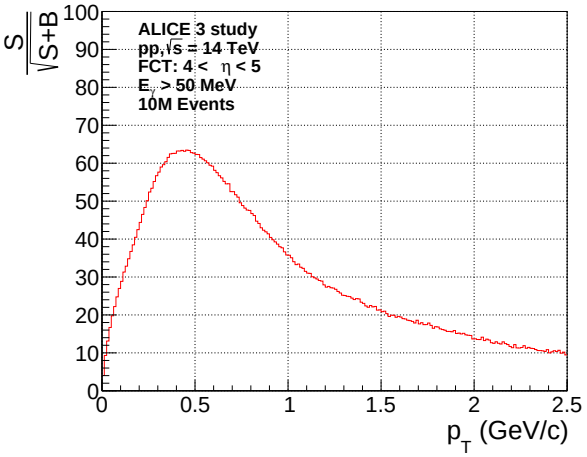

(c) Cut applied on the pointing angle and distance to the closest charged particle, $d_{cq} < 2\,\mathrm{cm}$.

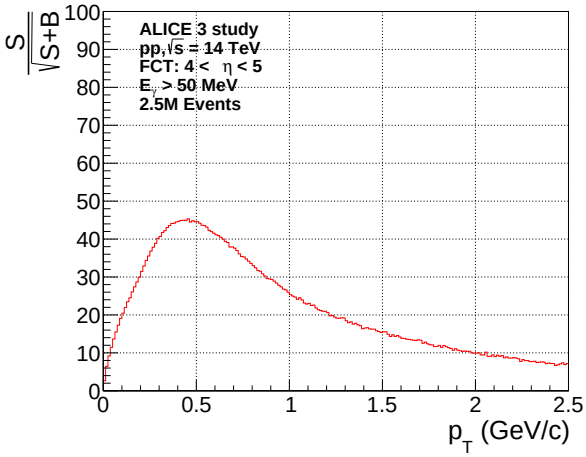

(d) ALICE 3 geometry with a window in the beam pipe and a cut applied on the pointing angle.

Figure 57: The corresponding significances of the π^0 invariant mass spectra in Fig. 56.

What must be noted is the difference in number of events simulated to make these histograms. For the "Default ALICE 3", 10M events were simulated. For the "Window 1" simulation set, 2.5M events were simulated. This causes the ratio $S/\sqrt{S+B}$ to be a factor 2 lower for the simulation set "Window 1". Taking this into account, the peak of the significance of Fig. 57d would then appropriately be at 90, which is higher than the 80 reported for Fig. 57b. Considering the figures with the significances and that low momentum photon reconstruction is the region where the FCT is most sensitive, the question then becomes how low in transverse momentum the FCT can reach for the measurement of the π^0 transverse momentum spectrum. Zooming in on the region of $p_{\mathrm{T}} < 200\,\mathrm{MeV}/c$ reveals just that in Fig. 58. The zoom in on these significances reveal that a significance of 5 is possible for the measurement of the π^0 transverse momentum in the range of 15–20 MeV/c and above.

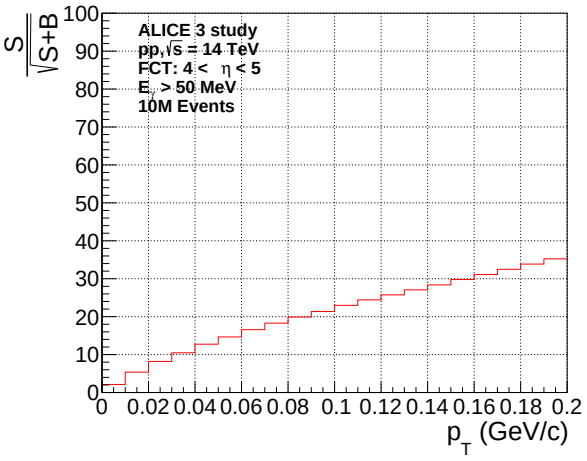

(a) No cuts applied.

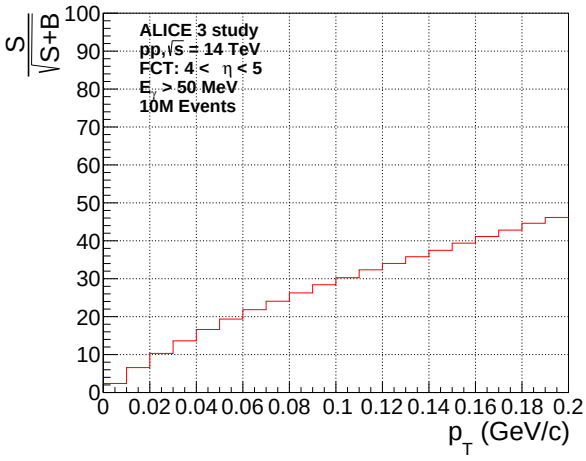

(b) Cut applied on the pointing angle.

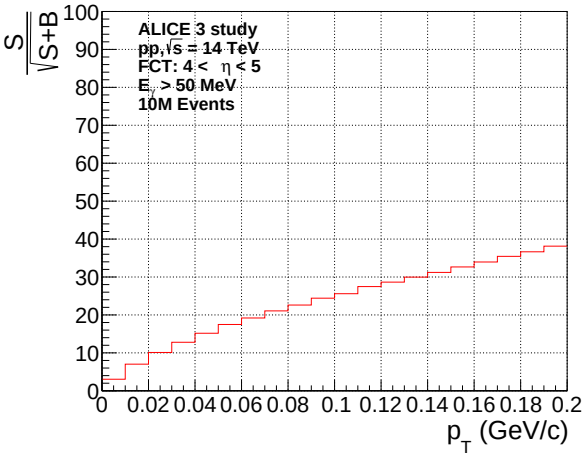

(c) Cut applied on the pointing angle and distance to the closest charged particle, $d_{cq} < 2\,\mathrm{cm}$.

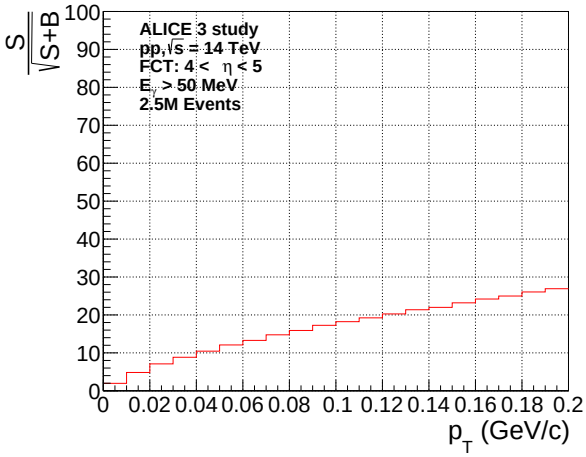

(d) ALICE 3 geometry with a window in the beam pipe and a cut applied on the pointing angle.

Figure 58: Zoom in on the significances of the π^0 transverse momentum spectra in Fig. 58 for $p_{\mathrm{T}} < 200\,\mathrm{MeV}/c$.

The acceptance for neutral pions as function of the p_{T} is shown in Fig. 59. The acceptance is the

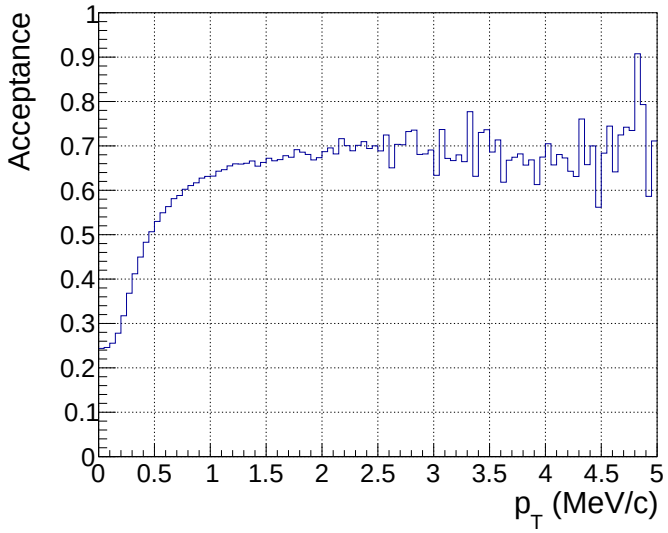

Figure 59: The acceptance of the FCT for π^0's in the rapidity range $4 \leq y \leq 5$ as function of their p_{T}.

ratio of number of π^0's with both photons in the FCT and the number of π^0's emitted in the rapidity

range of the FCT. For the number of π^0's emitted in the range of the FCT a PYTHIA simulation with 1M events was performed and the number of π^0's in the rapidity region $4 < y < 5$ recorded. For the number of π^0's with both photons in the FCT, the dataset "Default ALICE 3" was used and all π^0's with both their photons in the FCT in the same rapidity region were recorded. As can be seen, the material budget of ALICE 3 and the angle of emission between the two photons of a π^0 have a significant impact on the acceptance. This acceptance ratio can then we used to scale the data to retrieve the actual production of π^0's in pp collisions.

The ALICE Collaboration measured the π^0 transverse momentum spectrum in the range of $0.2 < p_{\mathrm{T}} < 200\,\mathrm{GeV}/c$ at mid-rapidity ($|y| < 0.8$) for pp collisions at $\sqrt{s} = 13\,\mathrm{TeV}$. Figs. 58 show that the FCT could measure the transverse momentum spectrum of π^0's in the pseudorapidity range $4 < y < 5$ above a significance of 5 for $p_{\mathrm{T}} > 10$–$20\,\mathrm{MeV}/c$ for pp collisions at $\sqrt{s} = 14\,\mathrm{TeV}$.

9 Discussion

9.1 How to improve the signal-to-background ratio?

As shown in this thesis, the material budget in front of the FCT, as given in Fig. 19, causes the dominant background of external bremsstrahlung and secondary interactions/decays. In the scoping document of ALICE 3 [32] and the Letter of Intent [8] it is quoted that the pseudorapidity coverage of the outer tracker disks should only extend up to $\eta < 4$, however, as shown in Fig. 9, these disks extend down to a much larger pseudorapidty range. As of writing, no studies have been undertaken which make use of this part of the outer tracker disks. Therefore the suggestion made in this thesis is to limit the outer tracker disks to their quoted pseudorapidity range in the SD and LoI to reduce the material budget in front of the FCT by 0.06 in X/X_0.

9.2 Alternative shape for the FCT

The disks of the FCT as simulated in this thesis are circular, however, a circular shape as sensitive volume is difficult to produce. Therefore, such a circular shape needs to be tiled by modules that carry the chip and sensor structures, which themselves are square. Covering a circle in rectangular/square shapes to approach the circular sensitive volume structure will also be done for the outer track disks. In a sense, these circular disks need to be squared, but then in the literal sense and not in the figure of speech where it means to do something impossible. The modules that carry these chips and sensors will from now on be referred to as sensor modules. These sensor modules come in a variety of shapes and sizes, but the ones under consideration, as will be laid out in the upcoming Scoping document [32], are 1 cm × 1 cm, 1 cm × 3 cm, 2 cm × 3 cm and 2 cm × 6 cm in size, with 1 cm × 1 cm being the least likely size to be actually produced in the end. Since the outer radius of the outer tracker disks is much larger than the FCT, it is in essence a lot easier to cover the circular shape with these sizes of modules and at the same time achieve a high coverage with sensor volumes of the total area of the disk. For the FCT, which has disks with an outer radius that is much smaller, covering the circle with these particular module sizes is bound to leave gaps in the coverage, reducing the total coverage significantly. This is a challenge as the coverage of the sensors directly influences the acceptance of the FCT. Two solutions to this problem exist, but one has a much larger benefit than the other. The first solution would be to introduce regions where sensors overlap to increase the coverage, but this increases the prospected material budget of the individual layers and cause multiple scattering to have more of an effect on the transverse momentum resolution of tracked electrons and consequently reconstructed photons. The second solution would be to make the disks square or rectangular. Tiling a square with square sensor modules increases the maximum coverage achievable significantly and does not require overlap of these sensor modules. The square layers[26] could then be placed above the beam pipe, instead of around it, which additionally removes the requirement of them having a hole in the middle of it. A sketch of a possible layout of these layers is given in Fig. 60. These square layers

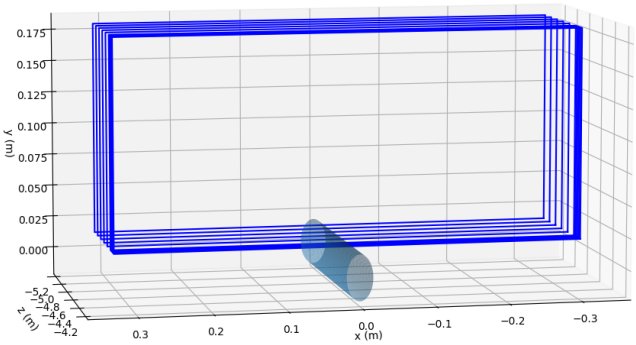

Figure 60: Schematic sketch of rectangular layers (dark blue) of the FCT above the beam pipe (light blue cylinder).

[26] they are not disks anymore

Layer	Circular disks			Rectangular layers		
	Inner Radius (cm)	Outer radius (cm)	Area (cm^2)	Height (cm)	Width (cm)	Area (cm^2)
0	5	17	830	17	48.8	830
1	5	17	830	17	48.8	830
2	5	17	830	17	48.8	830
3	5	17	830	17	48.8	830
4	5	17	830	17	48.8	830
5	5	17	830	17	48.8	830
6	5	17	830	17	48.8	830
7	5	18	940	18	52.2	940
8	5	18	940	18	52.2	940
9	5	19	1060	19	55.8	1060
10	5	19	1060	19	55.8	1060

Table 18: Comparison of the dimensions of circular to square layers of the FCT.

could then have the same area of sensitive volume, leaving the amount of sensors required unchanged. To keep the coverage in pseudorapitiy the same, the height of these layers would remain the same as the outer radius of the circular disks, which would allow the width of the layers to be increased. This is expected to increase the tracking capabilities of e^+e^- pairs. When a photon is created through a collision of protons at the coordinates close to $(0, 0, 0)$, the produced photon coming from the vertex has a momentum $\mathbf{p}$ and the e^+e^- conversion pair in the FCT will bend in the xz-plane through the presence of the dipole magnetic field, but the particles will still have a momentum component in the $\hat{y}-$direction that is unaffected by the presence of the magnetic field. This component, however, is small compared to the p_z component of the momentum and therefore the electrons are not expected to cover great distances in the $\hat{y}-$direction in comparison to the distances covered in the $xy-$plan, meaning that the width of the rectangular layer is more important to increase the acceptance of the detector than the height. Tab. 18 gives a comparison of the dimensions of these square layers with respect to the circular layers following these principles. The position in z and thickness of these layers remains the same. This would mean that the azimuthal coverage of the setup with rectangular layers is reduced compared to that of the one with circular disks, but it is believed this will be made up by the gain in acceptance of the FCT, i.e. how many of the photons that are incident on the FCT can actually be reconstructed.

9.3 IRIS tracker services; additional material in front of the FCT

The IRIS tracker of ALICE 3 is represented in O^2 as described in Sec. 5.1.1. This is not the final layout as services like data links, cables and others are missing. The services are mostly expected to run on top of the petal cases of the IRIS tracker and some inside where they are not in the pseudorapidty range of the FCT, but some will also be on the side of the petal cases, as can be seen by the slate blue geometric shape that partially encapsulates the petal cases in Fig. 17. Then there are the mechanical components which both keep the petal cases in place and allow for rotation and movement to settle the IRIS tracker in the retracted or contracted state. At the time of writing, much is unknown about these services which will probably be explained in more detail in the planned technical design report (TDR) for ALICE 3 that is supposed to be published in 2026/2027 according to the planning of the LoI [8]. As the design of the IRIS tracker still changes frequently, so do the placement of the service components and the amount needed. Therefore, in this thesis there is no attempt made to calculate the material budget of these components, but it is definitely expected to increase the material budget in front of the FCT. It is therefore important to consider an alternative design of ALICE 3 that incorporates a window in the beam pipe and/or that has no parts of the outer tracker disks in the pseudorapidty range of the FCT to keep the material budget in front of the FCT at an acceptable level.

9.4 Using Haissinski's formula to predict the internal bremsstrahlung spectrum at the FCT

The big advantage of Haissinski's formula is that not every charged particle that is produced in an $m \rightarrow n$ scattering process has to enter the formula to predict the internal bremsstrahlung spectrum. Sec. 2.5 showed the level of agreement between the internal bremsstrahlung spectrum as predicted by Low's theorem and Haissinski's adaptation. Fig. 2 showed the charged particle spectrum as function of the momentum as predicted by PYTHIA. This clearly showed that the dominant multiplicity is that of the charged pions. Fig. 43 then showed the charged particle spectrum to arrive at the FCT where the multiplicity of electrons showed an increase due to the fact that they were copiously created in the material in front of the FCT, but the charged pion spectrum remained dominant. To predict the internal bremsstrahlung spectrum by ways of measuring the momentum of the charged particles to arrive at the FCT requires particle identification, which is not present for the FCT if the FCT RICH is not present. To that end and considering the dominance of the charged pion multiplicity, every charged particle could be assumed to be a pion, which would make momentum extraction possible. Since the low momentum charged particles contribute less to the internal bremsstrahlung spectrum, a cut on the momentum could be placed to exclude most low momentum electrons, e.g. $p < 1\,\mathrm{GeV}/c$. As stipulated in Sec. 2.4, when charged particles arrive at the FCT, the spatial correlation between the charged particle that emitted the internal bremsstrahlung photon and the photon will be destroyed due to the presence of the magnetic field. Since the η or p_{T} of the charged particle enters in the Haissinski formula, the question remains how well the internal bremsstrahlung spectrum can be predicted based on the charged particle (read: charged pion) momentum spectrum measured with the FCT. Through MC simulations, the charged particle multiplicity can be predicted and through a measurement the acceptance can then be calculated and thus a correction factor as function of the transverse momentum can be established. However, the question remains how many charged particles that were created outside of the pseudorapidity range of the FCT enter the FCT due to the presence of the magnetic field. In similar fashion, this can be established by comparing the measurement with the simulations performed with O^2. A investigative study to this end could be interesting.

9.5 Perform the soft-photon spectrum measurement with the IRIS in the open position

An obvious reduction in the material budget would be to perform the measurement of the internal bremsstrahlung spectrum with the IRIS tracker in the retracted position. The cut on the pointing angle, as shown in Sec. 6.1, is very effective to reduce the contribution from the secondary interactions/decays to the total soft-photon spectrum. When the IRIS is in the contracted position, the position resolution of the primary vertex is expected to be of negligible contribution to the pointing angle resolution provided by the FCT. However, it is unknown if this remains to be the case when the IRIS tracker is in the retracted position since no tracking studies have been undertaken for this scenario at the time of writing. In the future, if this were done, it would be interesting to see if such a measurement would be possible because the benefits in reduction of the external bremsstrahlung as shown in Fig. 53b are clear.

9.6 A dedicated detector to measure the soft-photon spectrum

The Forward Conversion Tracker faces experimental difficulties within ALICE 3, the impact of which are explored in this thesis. Despite the measurements that claim the existence of an excess in the soft-photon spectrum a factor 4–8 times the predicted internal bremsstrahlung spectrum, the physics community is still divided about its existence, and equally so about a theoretical explanation. In this section, the acquired knowledge of experimental challenges for the FCT through this work is summarized to aid a proposal for a dedicated soft-photon detector (SPD). The SPD would be optimized to detect the soft-photon spectrum from hadron-hadron collisions with a significantly increased signal-to-background ratio compared to the FCT. Fig. 61 shows the radial projection of the SPD at a forward focused tracking experiment (FFTE). The SPD is heavily inspired by ALICE 3 and the FCT and like the FCT it would track and reconstruct $\mathrm{e}^+\mathrm{e}^-$ conversion pairs in the forward direction in a dipole

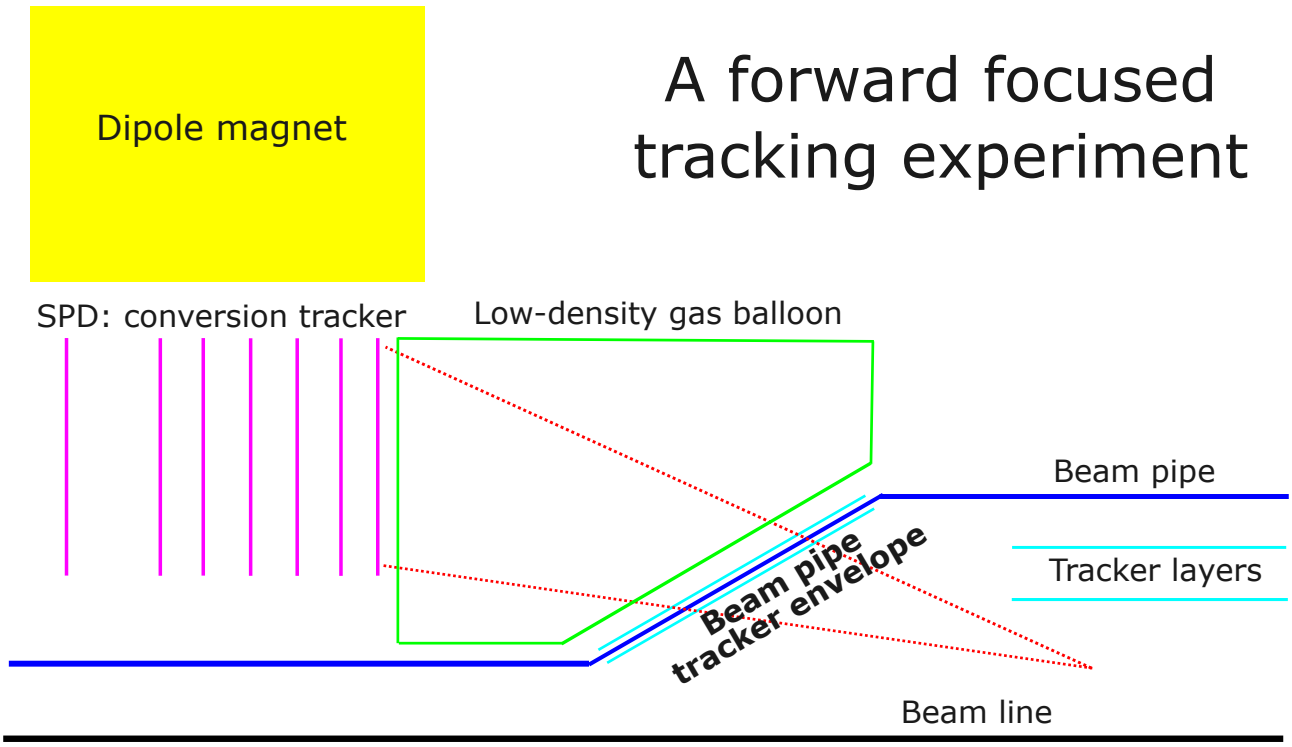

Figure 61: Radial projection of the soft-photon detector at the forward focused tracking experiment. The red lines indicate the psuedorapidity range of the soft-photon detector.

magnetic field to grant access to high energetic, but low-p_{T} photons. Optimizations are proposed to mitigate the challenges the FCT is facing, namely a conical beam pipe to have a low material budget, but also the absence of a solenoidal magnetic field to allow for charged particle reconstruction in the forward direction akin to the FCT, $4 < \eta < 5$. Two tracking layers inside the beam pipe reconstruct the position of the primary vertex which are asymmetric in z such that there is no contribution from its vacuum vessel or services to the material budget in front of the SPD. The defining feature is the conical beam pipe tracker envelope (BPE tracker) that provides an event veto based on electrons produced in the beam pipe material. The BPE tracker has two layers: one inside the conical beam pipe section (BPE L1), and one outside (BPE L2). Photons originating from decay processes produce a lot of electrons through conversions in the beam pipe. These electrons then produce external bremsstrahlung photons. Photons are neutral particles and do not leave a hit in the tracker layers, but charged particles do. In the case of the absence of a hit in BPE L1, but a presence of a hit in BPE L2, the presence of a neutral particle producing a charged particle through an interaction in the beam pipe material can be inferred and the event can be vetoed. If both layers register a hit that points to the primary vertex the presence of a primary charged particle can be inferred. The electron multiplicity in proton-proton collisions is very low in comparison to other charged particles and as such the event does not need to be vetoed if the presence of a charged particle can be established through the presence of a hit in both layers. The SPD would be a fair distance away from the interaction point such that the dipole has little influence on the tracking inside the beam pipe and for the tracking with the BPE. To reduce the contribution from air to the material budget in front of the SPD, a balloon with a low density gas is placed in between the SPD and the conical section in the beam pipe. This measurement would best be conducted at a lower center-of-mass energy for hadron-hadron collisions than at ALICE 3 to reduce the charged particle multiplicity and make tracking easier, but perhaps novel tracker layers could still deal with this at higher center-of-mass energies, or higher charged particle multiplicities as seen in heavy-ion collisions.

10 Conclusion

This thesis presents a novel internal bremsstrahlung generator (LPG) based on Low's theorem which is used to provide a first time full Monte Carlo simulation with generated internal bremsstrahlung photons propagated through the detector setup of ALICE 3. The LPG was compared to predictions made in previous studies and found to be in satisfying agreement. In addition, the robustness of Haissinski's formula was investigated compared to Low's theorem and it was found that Low's theorem is unstable when it has incomplete access to all initial- and final-state charged particles involved in a $m \to n$ scattering process. Haissinski's formula was shown to predict the internal bremsstrahlung spectrum with incomplete access of all charged particles involved, but predicted less soft-photons than Low's theorem that had access to all charged particles involved. By nature of the two formulas, the ratio between the two predictions is constant and thus can be used for scaling purposes if the acceptance of a detector is known to measure the soft-photon spectrum as function of the measured charged particles.

ALICE 3 will operate at a never seen before center-of-mass energy of $\sqrt{s} = 14\,\text{TeV}$ which is a huge jump in energy for the measurement of the internal bremsstrahlung spectrum as compared to previously conducted experiments that attempted this measurement. Great care was taken to map out the (spatial) origin of the different sources of background and multiple strategies were introduced to limit the impact of the background on the measurement after subtraction of the background from the data. A modification of the ALICE 3 setup in terms of a conical section in the beam pipe referred to as a "window" is discussed and it was shown to greatly improve the signal-to-background ratio. In addition, the inclusion of a Cherenkov detector to provide an event veto based on the presence of electrons is discussed. It was found that the inclusion of such a detector has the potential to improve the measurement, but additional studies are needed concerning the feasibility of the inclusion of focusing mirrors to provide ring reconstruction.

The uncertainty on the background originating from material interactions is estimated to be 5% by considering the contribution of the individual modules of ALICE 3 to the material budget. The precise machining of the beam pipe and the retractability of the IRIS tracker provide strong arguments that the impact of the uncertainty of material budget on the measurement of the soft-photon spectrum will be under control. In addition, three techniques are proposed to estimate the uncertainty on the photon spectrum that finds its origin in hadronic decays. With simulations it is shown that the π^0 transverse momentum spectrum can be measured in the pseudorapidity range of $4 < y < 5$ for $p_{\text{T}} > 20\,\text{MeV}/c$ above a significance of 5 for pp collisions, which is an order of magnitude lower in p_{T} than what ALICE achieved so far. It is likely that the FCT can perform this measurement in peripheral heavy-ion collisions and it might as well do this in central heavy-ion collisions.

The performance of the FCT for the measurement of the internal bremsstrahlung for the four scenarios discussed in this thesis is presented in Tab. 19. The table presents the significance and signal-to-background ratio for different values for both the case the internal bremsstrahlung spectrum is unenhanced, or enhanced by a factor 4 as was measured by previous experiments. This table shows the impact of the inclusion of a conical beam pipe to measure the unenhanced internal bremsstrahlung spectrum and has good signal-to-background ratio to boot. Without such a conical section in the beam pipe, a signal-to-background ratio of 0.1 is still desirable as background subtraction techniques tend to improve over time. In the case the internal bremsstrahlung spectrum is indeed enhanced, the FCT is in a good position to measure this, even without a conical beam pipe. However, with a conical beam pipe, a stronger upper limit on the magnitude of a possible excess can be given.

The integrated luminosity requirement for the measurements presented in this thesis is calculated to be $220\,\text{nb}^{-1}$ and ALICE 3 is expected to record $3.5\,\text{pb}^{-1}$ of collisions with readout frames that only contain 1 collision, satisfying the conditions for the FCT. Nevertheless, a dedicated low-luminosity run is recommended to achieve higher statistics and simplify the analysis process.

Scenario	Significance	Unenhanced		Enhanced (factor 4)	
		k_{T} (MeV/c)	**S/B**	k_{T} (MeV/c)	**S/B**
Cut on pointing angle	> 3	-	-	$0.5 < k_{\mathrm{T}} < 8$	0.15–0.18
	> 0.7	$0.5 < k_{\mathrm{T}} < 10$	0.03–0.045	$0.5 < k_{\mathrm{T}} < 10$	0.12–0.18
Cut on pointing angle	> 5	-	-	$0.5 < k_{\mathrm{T}} < 7.5$	0.24–0.48
and distance to closest	> 4	-	-	$0.5 < k_{\mathrm{T}} < 9.5$	0.2–0.48
charged particle	> 2	$0.5 < k_{\mathrm{T}} < 2$	0.09–0.12	$0.5 < k_{\mathrm{T}} < 10$	0.18–0.48
Conical beam pipe section plus cuts	≥ 5	$0.5 < k_{\mathrm{T}} < 1$	0.25–0.3	$0.5 < k_{\mathrm{T}} < 10$	0.24–1.2
	> 4	$0.5 < k_{\mathrm{T}} < 1.5$	0.19–0.3	$0.5 < k_{\mathrm{T}} < 10$	0.24–1.2
	> 3	$0.5 < k_{\mathrm{T}} < 3$	0.16–0.3	$0.5 < k_{\mathrm{T}} < 10$	0.24–1.2
	> 2	$0.5 < k_{\mathrm{T}} < 6$	0.1–0.3	$0.5 < k_{\mathrm{T}} < 10$	0.24–1.2
RICH behind FCT	≥ 5	$0.5 < k_{\mathrm{T}} < 5$	0.2–1	$0.5 < k_{\mathrm{T}} < 10$	0.4–4
	> 4	$0.5 < k_{\mathrm{T}} < 6$	0.2–1	$0.5 < k_{\mathrm{T}} < 10$	0.4–4

Table 19: Summary of the results in this thesis for the four presented scenarios to reduce the background for the measurement of the soft-photon spectrum.

Track reconstruction is the next step for the FCT. This was not explored in this thesis to a great detail, but the gaussian sum filter mentioned in Sec. 5.6 is promising. Increasing the pointing angle resolution should help to increase the signal-to-background ratio by a few percentile points. Increasing the ratio of reconstructable tracks will loosen the integrated luminosity requirement for the FCT. Although 15% in momentum resolution can be considered high, it did not have a great impact on the results presented in this thesis. Therefore, a comparable momentum resolution is deemed to be sufficient. A RICH behind the FCT is an interesting venue to explore further based on the results presented in this thesis, but the experimental challenges are significant. Tracking and a conical beam pipe are much more achievable goals in the near future. If the enhancement in the soft-photon spectrum is still present despite all the investigation done into the background sources for the measurement of the internal bremsstrahlung spectrum with the FCT, a dedicated soft-photon detector with strong soft-photon reconstruction capabilities is be proposed that improves the signal-to-background ratio further by reducing the material budget in front of it significantly and ideally incorporates a veto for events containing $\mathrm{e}^+\mathrm{e}^-$ pairs originating from material interactions.

References

[1] F. E. Low. Bremsstrahlung of very low-energy quanta in elementary particle collisions. *Phys. Rev.*, 110:974–977, May 1958. doi: 10.1103/PhysRev.110.974. URL https://link.aps.org/doi/10.1103/PhysRev.110.974.

[2] T. H. Burnett and N. M. Kroll. Extension of the Low soft-photon theorem. *Phys. Rev. Lett.*, 20: 86–88, Jan 1968. doi: 10.1103/PhysRevLett.20.86. URL https://link.aps.org/doi/10.1103/PhysRevLett.20.86.

[3] J. S. Bell and R. Van Royen. On the Low-Burnett-Kroll theorem for soft-photon emission. *Nuovo Cim. A*, 60:62–68, 1969. doi: 10.1007/BF02823297.

[4] S. Weinberg. *The Quantum Theory of Fields*, volume 1. Cambridge University Press, 1995.

[5] J. Antos et al. Soft photon production in 450 GeV/c p-Be collisions. *Z. Phys. C*, 59:547–554, 1993. doi: 10.1007/BF01562546.

[6] M. L. Tincknell et al. Low transverse momentum photon production in proton nucleus collisions at 18 GeV/c. *Phys. Rev. C*, 54:1918–1929, 1996. doi: 10.1103/PhysRevC.54.1918.

[7] J. Abdallah et al. Observation of the Muon Inner Bremsstrahlung at LEP1. *Eur. Phys. J. C*, 57: 499–514, 2008. doi: 10.1140/epjc/s10052-008-0779-z.

[8] The ALICE Collaboration. Letter of intent for ALICE 3: A next-generation heavy-ion experiment at the LHC, 2022. URL https://arxiv.org/abs/2211.02491.

[9] C. Bierlich et al. A comprehensive guide to the physics and usage of PYTHIA 8.3, 2022. URL https://arxiv.org/abs/2203.11601.

[10] A. T. Goshaw et al. Direct photon production from $\pi^+ p$ interactions at 10.5 GeV/c. *Phys. Rev. Lett.*, 43:1065–1068, Oct 1979. doi: 10.1103/PhysRevLett.43.1065. URL https://link.aps.org/doi/10.1103/PhysRevLett.43.1065.

[11] P.V. Chliapnikov et al. Observation of direct soft photon production in K+p interactions at 70 GeV/c. *Physics Letters B*, 141(3):276–280, 1984. ISSN 0370-2693. doi: https://doi.org/10.1016/0370-2693(84)90216-8. URL https://www.sciencedirect.com/science/article/pii/0370269384902168.

[12] F. Botterweck et al. Direct soft photon production in K + p and π + p interactions at 250 GeV/c. *Z. Phys. C*, 51:541–548, 1991. doi: 10.1007/BF01565578.

[13] S. Banerjee et al. Observation of direct soft photon production in π-p interactions at 280 GeV/c. *Phys. Lett. B*, 305:182–186, 1993. doi: 10.1016/0370-2693(93)91126-8.

[14] A. Belogianni et al. Confirmation of a soft photon signal in excess of QED expectations in π-p interactions at 280 GeV/c. *Phys. Lett. B*, 408:487–492, 1997. doi: 10.1016/S0370-2693(97)00762-4.

[15] A Belogianni et al. Further analysis of a direct soft photon excess in π-p interactions at 280 GeV/c. *Phys. Lett. B*, 548:122–128, 2002. doi: 10.1016/S0370-2693(02)02836-8.

[16] A Belogianni et al. Observation of a soft photon signal in excess of QED expectations in p p interactions. *Phys. Lett. B*, 548:129–139, 2002. doi: 10.1016/S0370-2693(02)02837-X.

[17] J. Abdallah et al. Evidence for an excess of soft photons in hadronic decays of Z^0. *Eur. Phys. J. C*, 47:273–294, 2006. doi: 10.1140/epjc/s2006-02568-8.

[18] J. Abdallah et al. Study of the dependence of direct soft photon production on the jet characteristics in hadronic Z^0 decays. *Eur. Phys. J. C*, 67:343–366, 2010. doi: 10.1140/epjc/s10052-010-1315-5.

[19] R. Bailhache et al. Anomalous soft photons: Status and perspectives. *Physics Reports*, 1097: 1–40, 2024. ISSN 0370-1573. doi: https://doi.org/10.1016/j.physrep.2024.10.002. URL https://www.sciencedirect.com/science/article/pii/S0370157324003478. Anomalous soft photons: Status and perspectives.

[20] P. Braun-Munziger et al. International workshop on soft photons, 1997.

[21] R. Bailhache et al. EMMI Rapid Reaction Task Force - Real and virtual photon production at ultra-low transverse momentum and low mass at LHC, 2022.

[22] S. Weinberg. Infrared photons and gravitons. *Phys. Rev.*, 140:B516–B524, Oct 1965. doi: 10.1103/PhysRev.140.B516. URL https://link.aps.org/doi/10.1103/PhysRev.140.B516.

[23] F. Bloch and A. Nordsieck. Note on the radiation field of the electron. *Phys. Rev.*, 52:54–59, Jul 1937. doi: 10.1103/PhysRev.52.54. URL https://link.aps.org/doi/10.1103/PhysRev.52.54.

[24] E. Barberio and Z. Wąs. PHOTOS - a universal Monte Carlo for QED radiative corrections: version 2.0. *Computer Physics Communications*, 79(2):291–308, 1994. ISSN 0010-4655. doi: https://doi.org/10.1016/0010-4655(94)90074-4. URL https://www.sciencedirect.com/science/article/pii/0010465594900744.

[25] N. Davidson, T. Przedzinski, and Z. Wąs. PHOTOS Interface in C++; Technical and Physics Documentation, 2015. URL https://arxiv.org/abs/1011.0937.

[26] C.A. van Veen. Low photon generator. https://github.com/Cas1997/Low-Photon-Generator, 2025.

[27] P Buncic, M Krzewicki, and P Vande Vyvre. Technical Design Report for the Upgrade of the Online-Offline Computing System. Technical report, 2015. URL https://cds.cern.ch/record/2011297.

[28] M.A. Völkl. Talk: Prospects for testing Low's theorem with ALICE 3. https://indico.cern.ch/event/1139676/sessions/438980/#20220921, 2022. New Vistas in Photon Physics in Heavy-Ion Collisions.

[29] V. N. Gribov. Bremsstrahlung of hadrons at high energies. *Sov. J. Nucl. Phys.*, 5:280, 1967.

[30] J. Haissinski. How to compute in practice the energy carried away by soft photons to all orders in α. *LAL-87-11*, 3 1987.

[31] J.J. Aubert et al. Evidence for anomalous prompt photons in deep inelastic muon scattering at 200 GeV. *Physics Letters B*, 218(2):248–256, 1989. ISSN 0370-2693. doi: https://doi.org/10.1016/0370-2693(89)91428-7. URL https://www.sciencedirect.com/science/article/pii/0370269389914287.

[32] The ALICE Collaboration. Alice 3 scoping document, in preparation, 2025.

[33] L. Betev et al. Definition of the ALICE coordinate system and basic rules for sub-detector components numbering. https://alice-servotech.web.cern.ch/HELP_DCDB-SVT/Help_Files/ALICE-INT-2003-038.pdf, 2003.

[34] M. Dey, V.L. Eletsky, and B.L. Ioffe. Mixing of vector and axial mesons at finite temperature: an indication towards chiral symmetry restoration. *Physics Letters B*, 252(4):620–624, 1990. ISSN 0370-2693. doi: https://doi.org/10.1016/0370-2693(90)90495-R. URL https://www.sciencedirect.com/science/article/pii/037026939090495R.

[35] I. Altsybeev. Private conversation about the collision pileup within the tracker read-out frame of ALICE 3. Internal simulation and performance meeting of ALICE 3, 2024.

[36] A. M. Sirunyan et al. Measurement of the inelastic proton-proton cross section at $\sqrt{s} = 13$ TeV. *Journal of High Energy Physics*, 2018(7), July 2018. ISSN 1029-8479. doi: 10.1007/jhep07(2018)161. URL http://dx.doi.org/10.1007/JHEP07(2018)161.

[37] M. Aaboud et al. Measurement of the inelastic proton-proton cross section at $\sqrt{s} = 13$ TeV with the ATLAS detector at the LHC. *Phys. Rev. Lett.*, 117:182002, Oct 2016. doi: 10.1103/PhysRevLett.117.182002. URL https://link.aps.org/doi/10.1103/PhysRevLett.117.182002.

[38] T.T. Böhlen et al. The FLUKA code: Developments and challenges for high energy and medical applications. *Nuclear Data Sheets*, 120:211–214, 2014. ISSN 0090-3752. doi: https://doi.org/10.1016/j.nds.2014.07.049. URL https://www.sciencedirect.com/science/article/pii/S0090375214005018.

[39] A. Ferrari et al. FLUKA: A multi-particle transport code (Program version 2005). 10 2005. doi: 10.2172/877507.

[40] J. Allison et al. Recent developments in Geant4. *Nuclear Instruments and Methods in Physics Research Section A: Accelerators, Spectrometers, Detectors and Associated Equipment*, 835:186–225, 2016. ISSN 0168-9002. doi: https://doi.org/10.1016/j.nima.2016.06.125. URL https://www.sciencedirect.com/science/article/pii/S0168900216306957.

[41] S. Agostinelli et al. Geant4 — a simulation toolkit. *Nuclear Instruments and Methods in Physics Research Section A: Accelerators, Spectrometers, Detectors and Associated Equipment*, 506(3):250–303, 2003. ISSN 0168-9002. doi: https://doi.org/10.1016/S0168-9002(03)01368-8. URL https://www.sciencedirect.com/science/article/pii/S0168900203013688.

[42] J. Allison et al. Geant4 developments and applications. *IEEE Transactions on Nuclear Science*, 53(1):270–278, 2006. doi: 10.1109/TNS.2006.869826.

[43] X. Ai et al. A Common Tracking Software Project. *Computing and Software for Big Science*, 6(1), apr 2022. ISSN 2510-2044. doi: 10.1007/s41781-021-00078-8. URL http://dx.doi.org/10.1007/s41781-021-00078-8.

[44] S. Navas et al. Review of particle physics. *Phys. Rev. D*, 110(3):030001, 2024. doi: 10.1103/PhysRevD.110.030001.

[45] T.S. Rogoschinski. *Performance of the Electromagnetic Pixel Calorimeter EPICAL-2 and soft-photon background studies in ALICE 3.* doctoralthesis, Universitätsbibliothek Johann Christian Senckenberg, 2024.

[46] The ALICE Collaboration. Inclusive photon production at forward rapidities in pp and p–pb collisions at $\sqrt{s_{\mathrm{NN}}} = 5.02$ TeV. *The European Physical Journal C*, 83(7), July 2023. ISSN 1434-6052. doi: 10.1140/epjc/s10052-023-11729-y. URL http://dx.doi.org/10.1140/epjc/s10052-023-11729-y.

[47] The ALICE Collaboration. Centrality dependence of the charged-particle multiplicity density at midrapidity in pb-pb collisions at $\sqrt{s} = 5.02$ TeV. *Physical Review Letters*, 116(22), June 2016. ISSN 1079-7114. doi: 10.1103/physrevlett.116.222302. URL http://dx.doi.org/10.1103/PhysRevLett.116.222302.

[48] D. Blockus et al. Direct electron pair production in π-p interactions at 16 GeV/c and a model for direct lepton and photon production at low p_{T}. *Nuclear Physics B*, 201(2):205–249, 1982. ISSN 0550-3213. doi: https://doi.org/10.1016/0550-3213(82)90430-8. URL https://www.sciencedirect.com/science/article/pii/0550321382904308.

[49] ATLAS Collaboration. Athena, April 2019. URL https://doi.org/10.5281/zenodo.2641997.

[50] X. Ai et al. ACTS Common Tracking Software docs. https://acts.readthedocs.io/en/latest/index.html#.

[51] G. Alocco. ACTS and NA60+: report at the ACTS Developers workshop 2024. https://indico.cern.ch/event/1397634/contributions/6143075/attachments/2969051/5225756/ACTSworkshop2024.pdf, 2024.

[52] B. Huth. *Track reconstruction for future high-energy-physics experiments with classical and machine-learning methods*. PhD thesis, Universität Regensburg, 2023.

[53] Aerogel Factory. https://www.aerogel-factory.jp/.

[54] Hamamatsu. S13360 series datasheet. https://www.hamamatsu.com/us/en/product/optical-sensors/mppc/mppc_mppc-array/S13360-3050CS.html, 2024.

[55] A. Gola et al. *Sensors*, 19(2), 2019. ISSN 1424-8220. doi: 10.3390/s19020308. URL https://www.mdpi.com/1424-8220/19/2/308.

[56] O. Rodrigues. Des lois géométriques qui régissent les déplacements d'un système solide dans l'espace, et de la variation des coordonnées provenant de ces déplacements considérés indépendamment des causes qui peuvent les produire. *Journal de Mathématiques Pures et Appliquées*, 1e série, 5:380–440, 1840. URL https://www.numdam.org/item/JMPA_1840_1_5__380_0/.

[57] A. G. Valdenebro. Visualizing rotations and composition of rotations with the rodrigues vector. *European Journal of Physics*, 37(6):065001, August 2016. ISSN 1361-6404. doi: 10.1088/0143-0807/37/6/065001. URL http://dx.doi.org/10.1088/0143-0807/37/6/065001.

[58] S. Vallarino et al. Prototype of a dual-radiator RICH detector for the Electron–Ion Collider. *Nuclear Instruments and Methods in Physics Research Section A: Accelerators, Spectrometers, Detectors and Associated Equipment*, 1058:168834, 2024. ISSN 0168-9002. doi: https://doi.org/10.1016/j.nima.2023.168834. URL https://www.sciencedirect.com/science/article/pii/S0168900223008252.

[59] R. Abdul Khalek et al. Science requirements and detector concepts for the Electron-Ion Collider: EIC Yellow Report. *Nuclear Physics A*, 1026:122447, 2022. ISSN 0375-9474. doi: https://doi.org/10.1016/j.nuclphysa.2022.122447. URL https://www.sciencedirect.com/science/article/pii/S0375947422000677.

[60] E. Cisbani et al. AI-optimized detector design for the future Electron-Ion Collider: the dual-radiator RICH case. *Journal of Instrumentation*, 15(05):P05009, may 2020. doi: 10.1088/1748-0221/15/05/P05009. URL https://dx.doi.org/10.1088/1748-0221/15/05/P05009.

[61] The ALICE Collaboration. The ALICE experiment at the CERN LHC. *Journal of Instrumentation*, 3(08):S08002, aug 2008. doi: 10.1088/1748-0221/3/08/S08002. URL https://dx.doi.org/10.1088/1748-0221/3/08/S08002.

[62] The ALICE Collaboration. Performance of the ALICE experiment at the CERN LHC. *International Journal of Modern Physics A*, 29(24):1430044, September 2014. ISSN 1793-656X. doi: 10.1142/s0217751x14300440. URL http://dx.doi.org/10.1142/S0217751X14300440.

[63] The ALICE Collaboration. The ALICE experiment: a journey through QCD. *The European Physical Journal C*, 84(8), August 2024. ISSN 1434-6052. doi: 10.1140/epjc/s10052-024-12935-y. URL http://dx.doi.org/10.1140/epjc/s10052-024-12935-y.

[64] B. Abelev et al. Neutral pion and η meson production in proton–proton collisions at $\sqrt{s} = 0.9$ TeV and $\sqrt{s} = 7$ TeV. *Physics Letters B*, 717(1–3):162–172, October 2012. ISSN 0370-2693. doi: 10.1016/j.physletb.2012.09.015. URL http://dx.doi.org/10.1016/j.physletb.2012.09.015.

[65] S. Acharya et al. Data-driven precision determination of the material budget in ALICE. *Journal of Instrumentation*, 18(11):P11032, November 2023. ISSN 1748-0221. doi: 10.1088/1748-0221/18/11/p11032. URL http://dx.doi.org/10.1088/1748-0221/18/11/P11032.

[66] P. Lu et al. Quantification of the low-p_{T} pion excess in heavy-ion collisions at the LHC and top RHIC energy, 2024. URL https://arxiv.org/abs/2407.09207.

[67] V. Begun and W. Florkowski. Bose-Einstein condensation of pions in heavy-ion collisions at energies available at the CERN Large Hadron Collider. *Physical Review C*, 91(5), May 2015. ISSN 1089-490X. doi: 10.1103/physrevc.91.054909. URL http://dx.doi.org/10.1103/PhysRevC.91.054909.

[68] J. D. Bjorken, K. L. Kowalski, and C. C. Taylor. Baked Alaska. In *7th Les Rencontres de Physique de la Vallee d'Aoste: Results and Perspectives in Particle Physics*, pages 507–528, 4 1993.

[69] K. Rajagopal and F. Wilczek. Static and dynamic critical phenomena at a second order QCD phase transition. *Nuclear Physics B*, 399(2):395–425, 1993. ISSN 0550-3213. doi: https://doi.org/10.1016/0550-3213(93)90502-G. URL https://www.sciencedirect.com/science/article/pii/055032139390502G.

[70] K. Rajagopal and F. Wilczek. Emergence of coherent long wavelength oscillations after a quench: application to QCD. *Nuclear Physics B*, 404(3):577–589, 1993. ISSN 0550-3213. doi: https://doi.org/10.1016/0550-3213(93)90591-C. URL https://www.sciencedirect.com/science/article/pii/055032139390591C.

[71] G. Amelino-Camelia, J. D. Bjorken, and S. E. Larsson. Disoriented chiral condensates in hadron-hadron collisions. *OUTP-96-53-P, CERN-TH-96-246, SLAC-PUB-7400*, 1996. URL https://arxiv.org/abs/hep-ph/9610202.

[72] A. M. Srivastava. Formation of disoriented chiral condensates in relativistic heavy-ion collisions. *Pramana*, 55(1):53–62, Jul 2000. ISSN 0973-7111. doi: 10.1007/s12043-000-0083-4. URL https://doi.org/10.1007/s12043-000-0083-4.

[73] C.M.G. Lattes, Y. Fujimoto, and S. Hasegawa. Hadronic interactions of high energy cosmic-ray observed by emulsion chambers. *Physics Reports*, 65(3):151–229, 1980. ISSN 0370-1573. doi: https://doi.org/10.1016/0370-1573(80)90165-9. URL https://www.sciencedirect.com/science/article/pii/0370157380901659.

[74] L.T. Baradzei et al. Observation of very high energy cosmic-ray families in emulsion chambers at high mountain altitudes (i). *Nuclear Physics B*, 370(2):365–431, 1992. ISSN 0550-3213. doi: https://doi.org/10.1016/0550-3213(92)90291-I. URL https://www.sciencedirect.com/science/article/pii/055032139290291I.

[75] B. Mohanty and J. Serreau. Disoriented chiral condensate: Theory and experiment. *Physics Reports*, 414(6):263–358, 2005. ISSN 0370-1573. doi: https://doi.org/10.1016/j.physrep.2005.04.004. URL https://www.sciencedirect.com/science/article/pii/S037015730500181X.

References - Personal contributions

During my doctoral studies I contributed to the following papers/publications:

[1] R. Bailhache, D. Bonocore, P. Braun-Munzinger, X. Feal, S. Floerchinger, J. Klein, K. Köhler, P. Lebiedowicz, C.M. Peter, R. Rapp, K. Reygers, W. Schäfer, H.S. Scheid, K. Schweda, J. Stachel, H. van Hees, C.A. van Veen, and M. Völkl. Anomalous soft photons: Status and perspectives. *Physics Reports*, 1097:1–40, 2024. ISSN 0370-1573. doi https://doi.org/10.1016/j.physrep.2024.10.002. URL `https://www.sciencedirect.com/science/article/pii/S0370157324003478`. Anomalous soft photons: Status and perspectives.

[2] ALICE Collaboration. Preliminary title: ALICE 3 scoping document, 2025.

[3] C.A. van Veen. Low Photon Generator. `https://github.com/Cas1997/Low-Photon-Generator`, 2025

The first has a way broader and more general explanation of the theory used in this thesis and the second is about the proposed ALICE 3 experiment, of which the Forward Conversion Tracker (talked about in this thesis) is a part of. The scoping document for ALICE 3 is unpublished as of the date of writing, but will be published in the near future. Both of these references are used extensively in my thesis. The third item, the Low Photon Generator is a piece of code I made for the purposes of this thesis and I talk extensively about its performance. It is available to the public on github.

11 Appendix

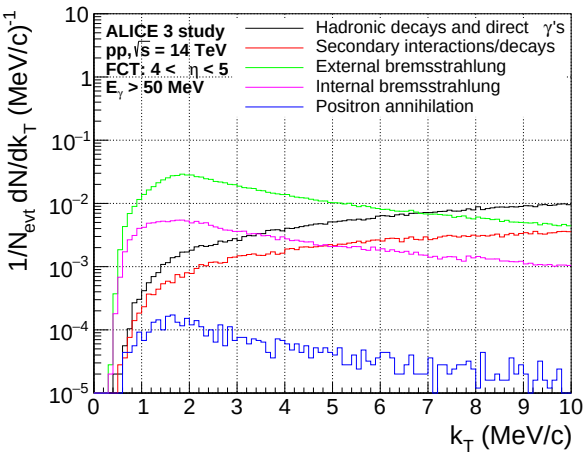

(a) Window length 200 cm

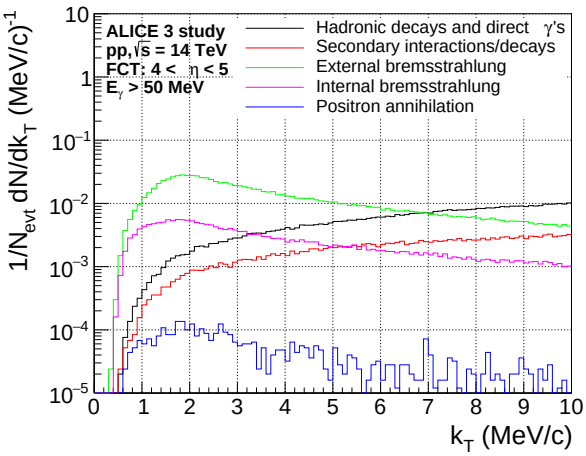

(b) Window length 250 cm

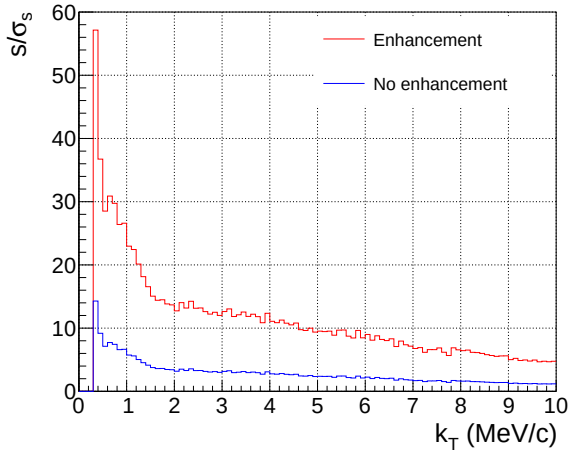

(c) Window length 200 cm

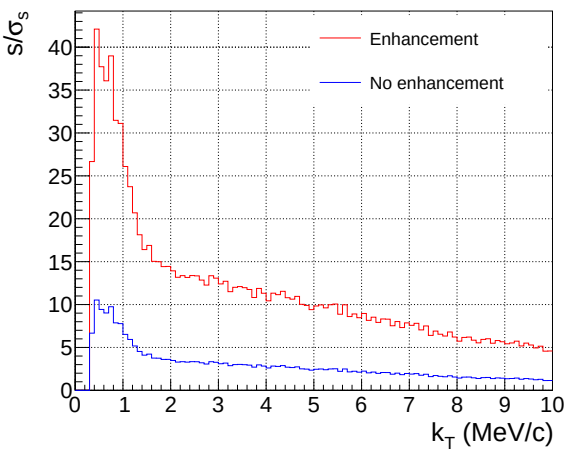

(d) Window length 250 cm

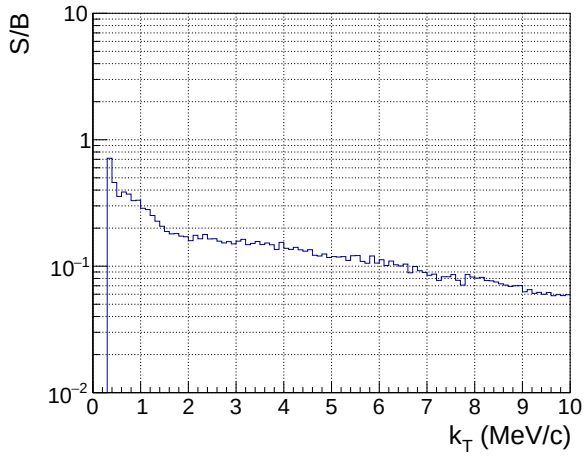

(e) Window length 200 cm

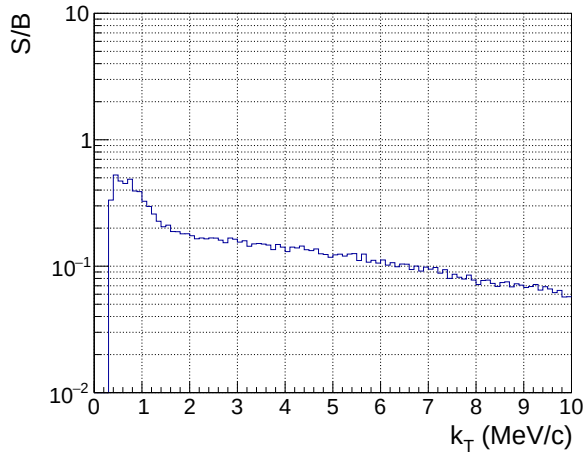

(f) Window length 250 cm

Figure 62: Photon spectra, significance with and without enhancement and signal-to-background ratio for different window lengths, 200 and 250 cm, respectively.

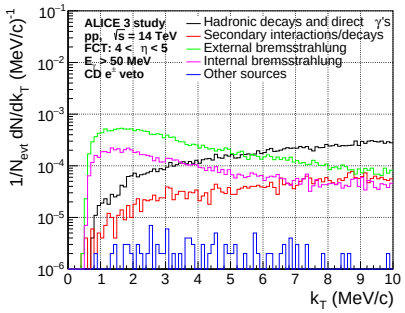

(a) 3050cs, He, Sim 1, $L = 1$ m, $N_{\text{Hits th.}} = 2$, ROF = 2 ns

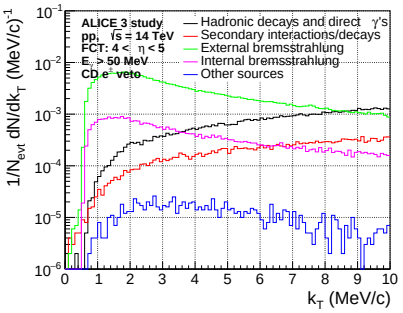

(b) 3050cs, He, Sim 2, $L = 1$ m, $N_{\text{Hits th.}} = 3$, ROF = 2 ns

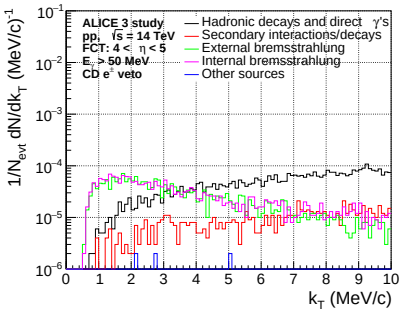

(c) 3050cs, He, Sim 3, $L = 1.8$ m, $N_{\text{Hits th.}} = 2$, ROF = 2 ns

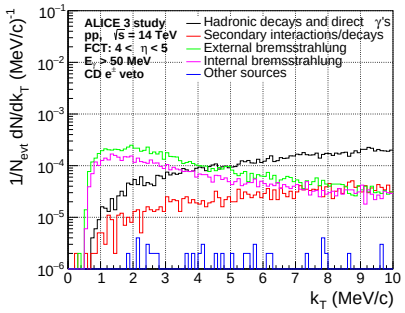

(d) 3050cs, He, Sim 4, $L = 1.8$ m, $N_{\text{Hits th.}} = 3$, ROF = 2 ns

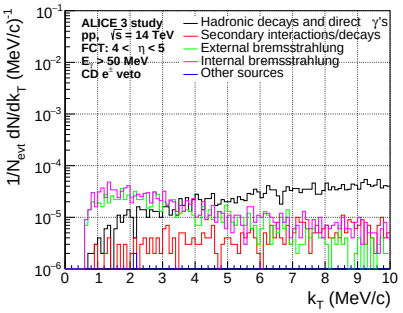

(e) 3050cs, He, Sim 5, $L = 1$ m, $N_{\text{Hits th.}} = 2$, ROF = 20 ns

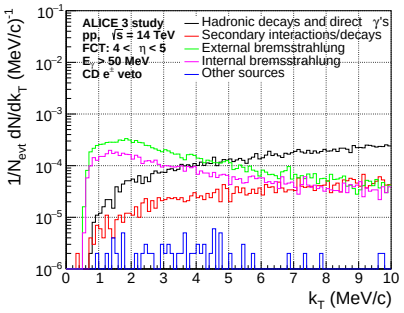

(f) 3075cs, He, Sim 1, $L = 1$ m, $N_{\text{Hits th.}} = 2$, ROF = 2 ns

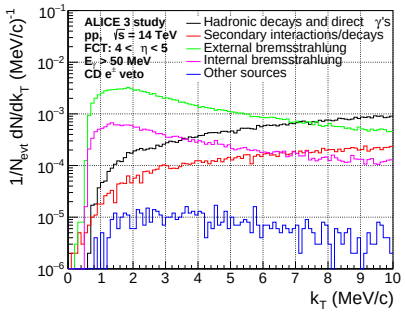

(g) 3075cs, He, Sim 2, $L = 1$ m, $N_{\text{Hits th.}} = 3$, ROF = 2 ns

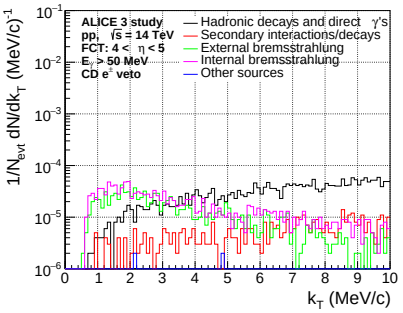

(h) 3075cs, He, Sim 3, $L = 2.45$ m, $N_{\text{Hits th.}} = 2$, ROF = 2 ns

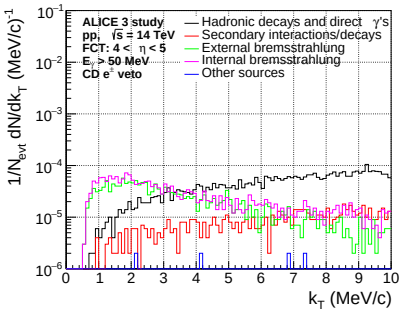

(i) 3075cs, He, Sim 4, $L = 2.45$ m, $N_{\text{Hits th.}} = 3$, ROF = 2 ns

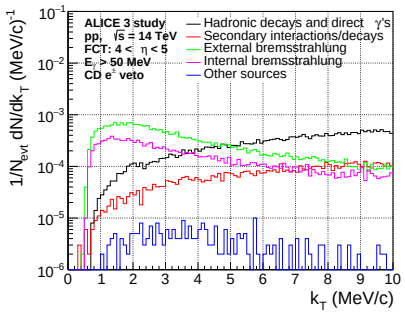

(j) 3075cs, He, Sim 5, $L = 2.45$ m, $N_{\text{Hits th.}} = 6$, ROF = 2 ns

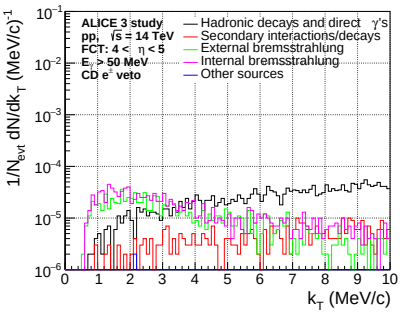

(k) 3075cs, He, Sim 6, $L = 1$ m, $N_{\text{Hits th.}} = 2$, ROF = 20 ns

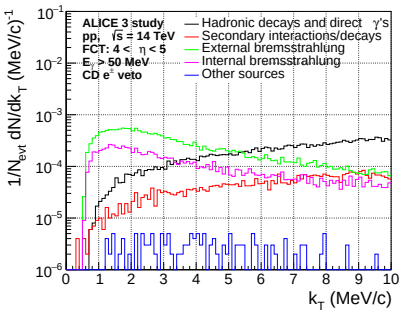

(l) FKB 3V, He, Sim 1, $L = 1$ m, $N_{\text{Hits th.}} = 2$, ROF = 2 ns

Figure 63: Photon spectra of all FCT RICH simulations (part 1/3).

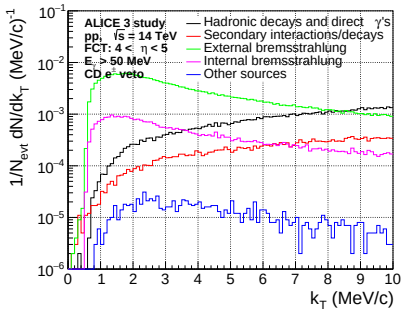

(a) FKB 3V, He, Sim 2, $L = 1$ m, $N_{\text{Hits th.}} = 3$, ROF $= 2$ ns

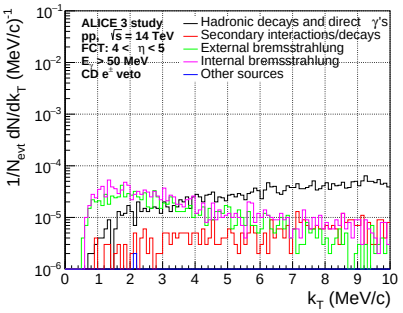

(b) FKB 3V, He, Sim 3, $L = 2.98$ m, $N_{\text{Hits th.}} = 2$, ROF $= 2$ ns

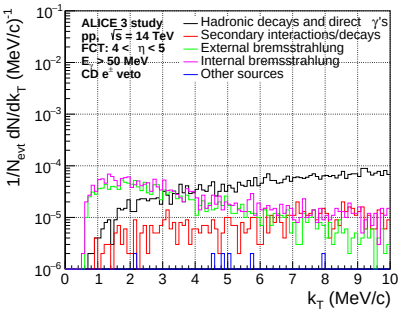

(c) FKB 3V, He, Sim 4, $L = 2.98$ m, $N_{\text{Hits th.}} = 3$, ROF $= 2$ ns

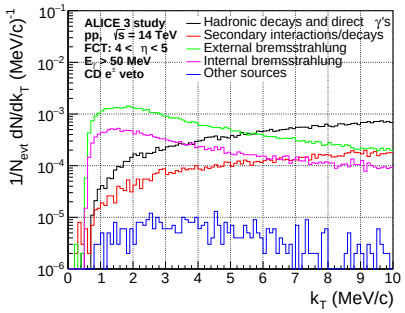

(d) FKB 3V, He, Sim 5, $L = 2.98$ m, $N_{\text{Hits th.}} = 7$, ROF $= 2$ ns

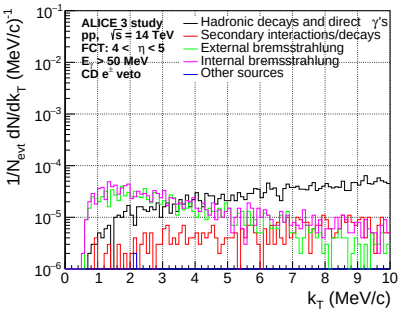

(e) FKB 3V, He, Sim 6, $L = 1$ m, $N_{\text{Hits th.}} = 2$, ROF $= 20$ ns

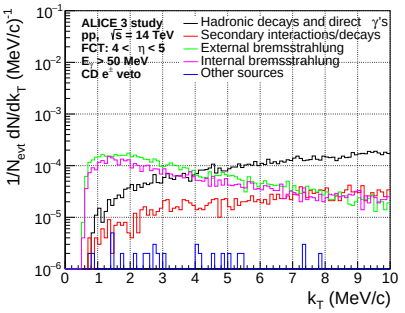

(f) 3050cs, Ne, Sim 1, $L = 1$ m, $N_{\text{Hits th.}} = 2$, ROF $= 2$ ns

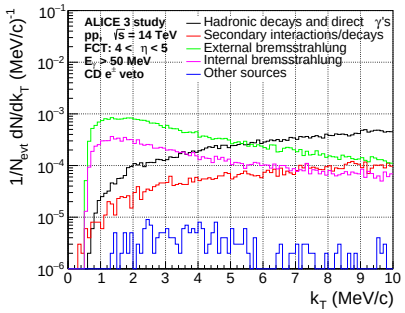

(g) 3050cs, Ne, Sim 2, $L = 1$ m, $N_{\text{Hits th.}} = 3$, ROF $= 2$ ns

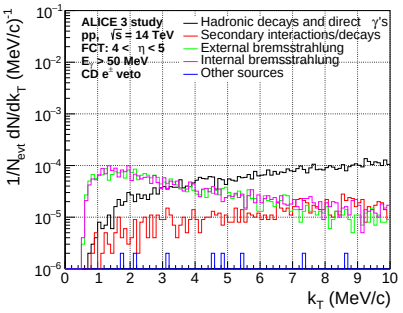

(h) 3050cs, Ne, Sim 3, $L = 1.8$ m, $N_{\text{Hits th.}} = 3$, ROF $= 2$ ns

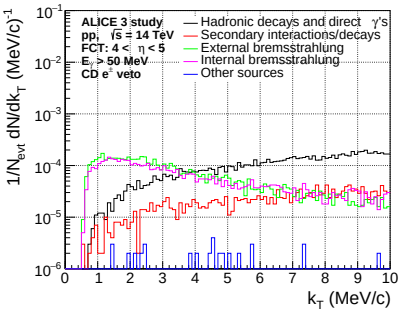

(i) 3050cs, Ne, Sim 4, $L = 1.8$ m, $N_{\text{Hits th.}} = 4$, ROF $= 2$ ns

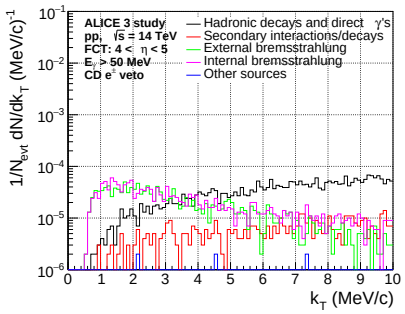

(j) 3050cs, Ne, Sim 5, $L = 1$ m, $N_{\text{Hits th.}} = 2$, ROF $= 20$ ns

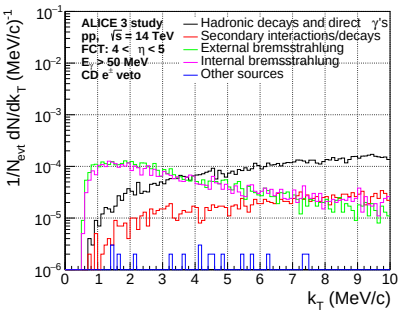

(k) 3075cs, Ne, Sim 1, $L = 1$ m, $N_{\text{Hits th.}} = 2$, ROF $= 2$ ns

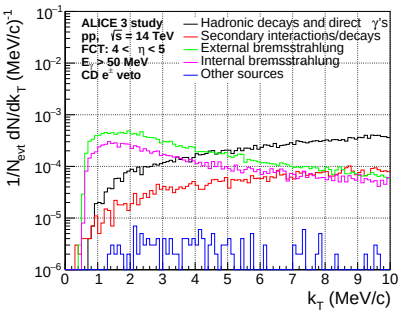

(l) 3075cs, Ne, Sim 2, $L = 1$ m, $N_{\text{Hits th.}} = 3$, ROF $= 2$ ns

Figure 64: Photon spectra of all FCT RICH simulations (part 2/3).

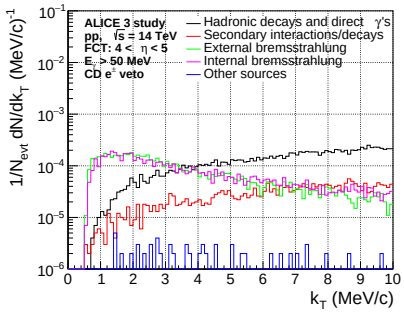

(a) 3075cs, Ne, Sim 3, $L = 2.45$ m, $N_{\text{Hits th.}} = 7$, ROF $= 2$ ns

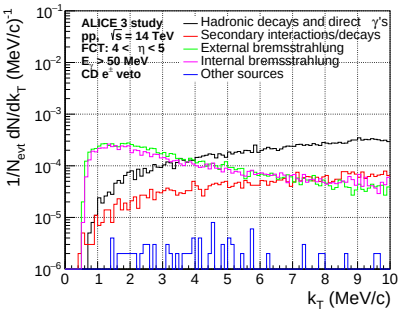

(b) 3075cs, Ne, Sim 4, $L = 2.45$ m, $N_{\text{Hits th.}} = 8$, ROF $= 2$ ns

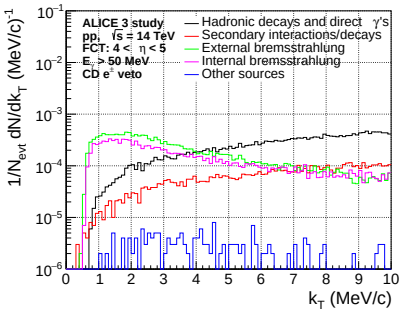

(c) 3075cs, Ne, Sim 5, $L = 2.45$ m, $N_{\text{Hits th.}} = 9$, ROF $= 2$ ns

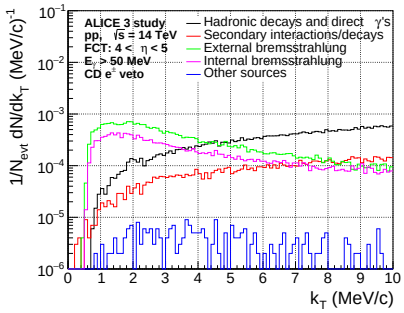

(d) 3075cs, Ne, Sim 6, $L = 2.45$ m, $N_{\text{Hits th.}} = 10$, ROF $= 2$ ns

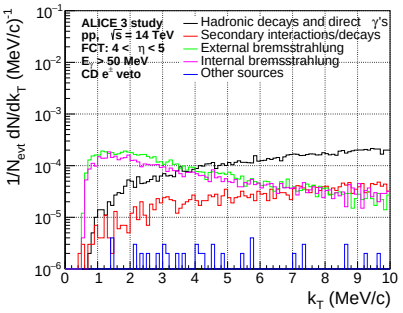

(e) FKB 3V, Ne, Sim 1, $L = 1$ m, $N_{\text{Hits th.}} = 2$, ROF $= 2$ ns

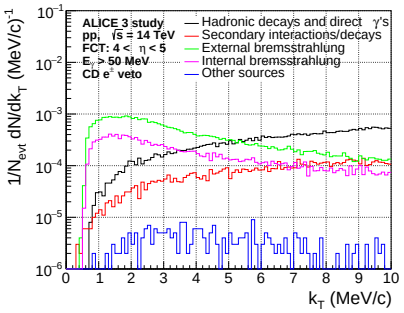

(f) FKB 3V, Ne, Sim 2, $L = 1$ m, $N_{\text{Hits th.}} = 3$, ROF $= 2$ ns

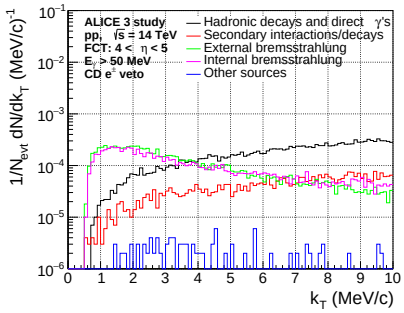

(g) FKB 3V, Ne, Sim 3, $L = 2.98$ m, $N_{\text{Hits th.}} = 8$, ROF $= 2$ ns

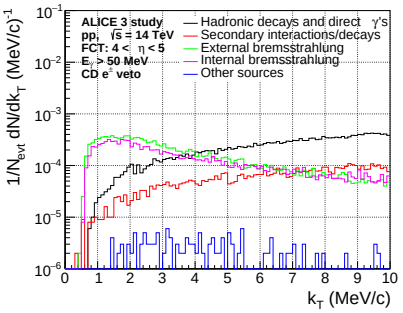

(h) FKB 3V, Ne, Sim 4, $L = 2.98$ m, $N_{\text{Hits th.}} = 9$, ROF $= 2$ ns

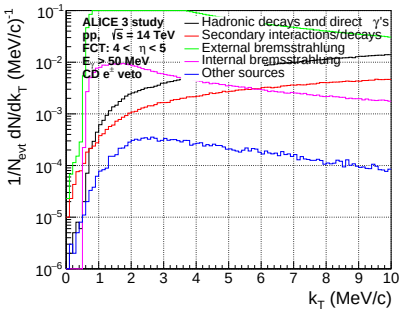

(i) FKB 3V, Ne, Sim 5, $L = 2.98$ m, $N_{\text{Hits th.}} = 10$, ROF $= 2$ ns

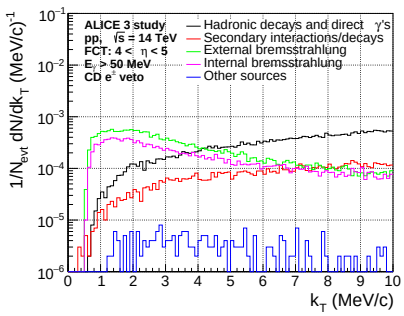

(j) FKB 3V, Ne, Sim 6, $L = 2.98$ m, $N_{\text{Hits th.}} = 10$, ROF $= 20$ ns

Figure 65: Photon spectra of all FCT RICH simulations (part 3/3).